3-D Common Plane Wave Section Migration

Reynam Pestana, CPGG/UFBA, Paul L. Stoffa, IG-UTEXAS,
ALex S. B. Melo, CPGG/UFBA

Abstract

We present a depth migration method that is based on double downward extrapolation of seismic data transformed to the source wavenumber and horizontal ray parameter domain. Initially the data are slant-stacked along the offset direction for each shot and then organized into common ray parameter sections ($\vec{p}_o$). Each constant $\vec{p}_o$ section is migrated separately in a manner similar to a post-stack migration procedure, except for an additional term related to the ray parameter. For a constant velocity medium we present a Stolt migration procedure for common $\vec{p}_o$ sections that can be used to quickly provide depth migrated sections. The prestack depth migration of ray parameter sections was tested on 3-D synthetic data and obtained reasonable results even for a strong lateral contrast velocity model like the SEG/EAEG salt model. The method leads naturally to implementations on parallel computers and is computationally efficient making it viable for a velocity analysis tool in many areas.

Introduction

Prestack depth migration for the large volumes of data acquired in modern 3D surveys remains a computational challenge even for today's fastest computers. Phase-shift migration algorithms preserve the high frequency information in the seismic data and are exact for all dips when there is no lateral velocity variation. Here we present a 3-D prestack phase shift migration method for plane-wave data. It is computationally efficient and can be easily implemented on parallel computers since each plane wave section can be independently migrated. We believe it can be used as part of a velocity analysis tool and will prove useful for 3D data in many situations.

Prestack phase-shift migration can be described by starting with the double-square-root (DSR) equation of Yilmaz (1979), which in its original form requires that all offsets and common-midpoint (CMP) data be downward continued simultaneously. The result of this prestack migration is a completely migrated section. Some notable artifacts during the integration along the offset-wavenumber axis may occur due to sparseness in offset sampling. Popovic (1993) showed that such artifacts can be avoided by sub-sampling the offset-wavenumber axis without taking into account the evanescent wave and also presented a method to downward continue separate offsets by evaluating the offset-wavenumber integral using the stationary phase method. Pestana et al. (1997) has applied Popovic's method for migration of common offset data using the stationary phase method to correct the non-zero offsets. Alkhalifah (1997) presented numerically, and through analytical approximations, the evaluation of the stationary point solution for non-zero-offset data.

To migrate sections of constant offset we derive the propagation operator as a function of offset. Normally the operator does not have a closed form solution and the stationary phase solution is obtained through a numerical procedure or by using an approximation even for the constant velocity case. However, for data in the source wavenumber and ray parameter ($\vec{k}_s, \vec{p}_o$) domain, the propagation operator has a closed form and it can be applied directly for each separate common ray parameter, $\vec{p}_o$, section (Pestana and Stoffa,2001). Since each ray parameter section can be migrated independently, the algorithms we describe are ideally suited for distributed memory parallel computer architectures, e.g., PC and workstation clusters.

For the constant velocity case, Stolt's frequency-wavenumber migration (Stolt, 1978) is recognized as a very fast method of doing both post-stack and prestack migration and it can be used for migration velocity analysis due to its high computational efficiency and accurate imaging for dips up to 90 degrees. In this work we present a Stolt migration procedure for common $\vec{p}_o$ sections.

Theory and the Method

Starting from the DSR equation (Claerbout, 1985), the migrated data for all sources and receivers, as a function of depth (z) and wavenumber vector, $\vec{k}$, are obtained by multiplying the Fourier transformed recorded wave field $D(\vec{k}_s, \vec{k}_g, \omega)$ by complex exponentials and summing over frequency:

$$P(\vec{k}_s, \vec{k}_g, z) = \int d\omega \; e^{-i \int_0^z k_z(\sigma) d\sigma} D(\vec{k}_g, \vec{k}_s, \omega), \tag{1}$$

where P is the downward continued field in depth, D is the input data and $e^{-i\int_0^z k_z(\sigma)d\sigma}$ is the propagation operator. The coordinates are source wavenumber vector, $\vec{k}_s$, receiver wavenumber vector, $\vec{k}_g$, depth ,z, and frequency, ω.

The vertical wavenumber, k_z, for $v(z)$, the velocity defined as a function of depth, is given by:

$$k_z = \sqrt{\frac{\omega^2}{v^2(z)} - |\vec{k}_g|^2} + \sqrt{\frac{\omega^2}{v^2(z)} - |\vec{k}_s|^2} \quad (2)$$

We now introduce a change of variables in the space domain to go from source and receiver vector coordinates to source and offset coordinates:

$$\vec{x}_o = \vec{x}_g - \vec{x}_s \quad \text{and} \quad \vec{x_s'} = \vec{x}_s, \quad (3)$$

where $\vec{x}_s, \vec{x}_g,$ and $\vec{x}_o$ are the source, receiver and offset vector coordinates and vector notation $\vec{x} = (x, y)$ is used to denote the surface location of the sources and receivers and $\vec{k} = (k_x, k_y)$ is the corresponding wavenumber vector.

In Fourier transform space, the offset wavenumber vector, $\vec{k}_o$, and source wavenumber vector, $\vec{k_s'}$, are related to the source wavenumber vector, $\vec{k}_s$, and receiver wavenumber vector, $\vec{k}_g$, by

$$\vec{k}_g = \vec{k}_o \quad \text{and} \quad \vec{k}_s = \vec{k_s'} - \vec{k}_o. \quad (4)$$

Dropping the primes for convenience, the downward continuation of the data in the offset and source wavenumber domain is

$$P(\vec{k}_s, \vec{k}_o, z, \omega) = e^{-i\int_0^z k_z(\sigma)d\sigma} D(\vec{k}_s, \vec{k}_o, \omega), \quad (5)$$

where the vertical wavenumber, $k_z(\vec{k}_s, \vec{k}_o, z, \omega)$, is given by

$$k_z = \sqrt{\frac{\omega^2}{v^2(z)} - |\vec{k}_o|^2} + \sqrt{\frac{\omega^2}{v^2(z)} - |\vec{k}_s - \vec{k}_o|^2}\ . \quad (6)$$

The image is obtained by applying the inverse Fourier transform from wavenumber $\vec{k}$, to space, $\vec{x}$, and from frequency ω, to time, t, over the downward continued wave field and evaluating it for t=0 and offset equal to zero (the imaging condition). In this way we obtain the 3-D prestack migrated data as:

$$P(\vec{x}_s, z) = \int d\vec{k}_o \int d\vec{k}_s e^{i\vec{k}_s\cdot\vec{x}_s} \int d\omega\ P(\vec{k}_s, \vec{k}_o, z, \omega) \quad (7)$$

and the extrapolated data $P(\vec{k}_s, \vec{k}_o, z, \omega)$ (eq. 5) is evaluated depth by depth interval recursively using the mean velocity of each depth interval.

From offset wavenumber to ray parameter

Substituting $\vec{p_o} = \vec{k_o}/\omega$ into equation (5) implies a change in integration variable from $\vec{k_o}$ to $\vec{p_o}$ and results in the following downward continuation equation:

$$P(\vec{k}_s, \vec{p}_o, z, , \omega) = e^{-i\int_0^z k_z(\sigma)d\sigma} D(\vec{k}_s, \vec{p}_o, \omega), \quad (8)$$

where the vertical wavenumber (eq. 6), is now given by

$$k_z = \sqrt{\frac{\omega^2}{v^2(z)} - |\omega\vec{p}_o|^2} + \sqrt{\frac{\omega^2}{v^2(z)} - |\vec{k}_s - \omega\vec{p}_o|^2} \quad (9)$$

and the image is obtained by the following equation

$$P(\vec{x}_s, z) = \int d\vec{p}_o \int d\vec{k}_s e^{i\vec{k}_s\cdot\vec{x}_s} \int |\omega|\ d\omega P(\vec{k}_s, \vec{p}_o, z, \omega). \quad (10)$$

$\vec{\mathrm{p}}_\mathrm{o} - \vec{\mathrm{k}}_\mathrm{s}$ Stolt migration

For the constant velocity case, we solve eq. (9) for ω:

$$\omega = \frac{v\ (k_z^2\ +\ |\vec{k}_s|^2)}{2\ k_z\sqrt{1 - v^2|\vec{p}_o|^2} + 2\ v\ (\vec{k}_s.\vec{p}_o)}. \quad (11)$$

The advantage of such a transformation is that we can use a fast Fourier transform (FFT) to compute the discretized integral. After the change of variable from ω to k_z, the $\vec{p}_o - \vec{k}_s$ Stolt migration becomes

$$P(\vec{k}_s, \vec{p}_o, z) = \int dk_z\ e^{-ik_z z}\ J\ D(\vec{k}_s, \vec{p}_o, \omega(k_z, \vec{k}_s)), \quad (12)$$

where $J = J(k_z, \vec{k}_s)$ represents the Jacobian of the transformation from ω to k_z and $D(\vec{k}_s, \vec{p}_o, \omega(k_z, \vec{k}_s))$ is the initial data as a function of the new variable k_z.

Numerical examples

Dipping Layer model

Initially we test the prestack migration method described above for a 3-D model that includes a dipping and a horizontal layer. The constant velocity value for this model is 1.5 km/s. For the Stolt and phase-shift migrations we choose (p_{oy}, p_{ox}) constant sections with values of $p_{oy} = -.2, .0, .2$

sec/km and 11 p_{ox} sections from -.2 to .2 sec/km. The results and are presented in Figure 1(a) and 1(b), respectively. The migration results with the Stolt and phase-shift methods present the horizontal layer below the dip layer in its correct position which indicate that the migration methods proposed here works very well for this synthetic data.

SEG/EAEG salt model

We also applied the prestack migration method for a volume data with 32 lines from the 3-D SEG/EAEG salt model. The velocity field of the lines 1 and 32 are shown in Figure 2(a) and 2(b), respectively. From the velocity field we generated 675 shots (but only 505 used here) with 61 x-offset ray parameter sections (p_{ox}) from -.2 to .4 s/km with Δp_0 increment equal to .01 s/km and only one y-offset ray parameter section ($p_{oy} = 0.$). The Figures 3 and 4 show the migration results for lines 1 and 32, for the respective $\vec{p_o}$ constant sections. For Stolt migration we need a velocity equal to 2.0 km/s and for the phase-shift migration the mean velocity of each depth. The final migrated section were obtained after stacking all ray parameter sections. The imaging obtained using the 3-D prestack phase-shift method of common plane wave sections even for this data where strong velocities exist between the salt body and the surrounding medium, presented the base and top of the salt and others structures clear and reasonably positioned confirming the applicability of this new method.

Conclusions

We present a plane wave prestack depth migration method, where all the sources for each ray parameter section are downward continued simultaneously. The use of this domain allows migration of each ray parameter section using a very efficient implementation of the algorithm and produces good results within the limitations of the method as confirmed by the synthetic examples. We tested the method for data from the SEG/EAEG salt model; the results show that the base and the top of the salt are very well positioned. The method is applicable to 2-D and 3-D seismic data and since each ray parameter section can be migrated independently, a parallel implementation using, e.g., clusters, can make the method attractive for routine 3D use. For constant velocity, our $p_o - k_s$ Stolt migration also can quickly produces angle-domain CIG that can be used locally as part of a velocity analysis. The method developed here could also be used to do a 3-D phase-shift plus interpolation (PSPI) prestack migration (Gazdag et al., 1984). In this case, each migration would be done with v(z) only at several spatial positions and then interpolated to produce the final image result.This is an alternative approach to the method of full prestack depth migration presented by Tanis et al. (1998) as an extension of the original split-step Fourier method (Stoffa et al., 1990).

Acknowledgments

The first author acknowledges CNPq (process no. 300.812/88-1). Alex Melo thanks ANP for the financial support of a schoolarship.

References

Alkhalifah, T., 1997, Prestack time migration of anisotropic media: Expanded Abstracts 60th Ann. Inter. Mtg., SEG, 1583-1586.

Claerbout, J.F., 1985, Imaging the earth's interior: Blackwell Scientific Publications.

Gazdag, J., and Sguazzero, P., 1984, Migration of seismic data by phase shift plus interpolation: Geophysics, 49 124-131.

Pestana, R. C. and Costa M. S.,1997, Two-step migration of common offset data (in Portuguese): 5th Int. Cong. Braz. Geophys. Soc., Extend Abstracts, 163-166.

Pestana, R. C. and Stoffa, P. L.,2001, Plane wave time migration, J. Seismic. Explor.,9:223-233

Popovic, M., 1993, Pre-stack phase-shift migration of separate offsets: SEP-79, 115-127.

Stoffa, P. L., Fokkema, J. T., Freire, R. M. L., and Kessinger, W. P., 1990, Split-step Fourier depth migration: Geophysics, 55, 410-421.

Stolt, R. H., 1978, Migration by Fourier transform: Geophysivs, vol. 43, 23-48.

Tanis, M. C., Stoffa, P. L., and Pestana, R. C., 1998, Prestack depth migration in the source-offset domain: Expanded Abstracts 61th Ann. Inter. Mtg., SEG, 1839-1842.

Yilmaz, O., 1980, Prestack partial migration: Ph.D. Thesis, Stanford University

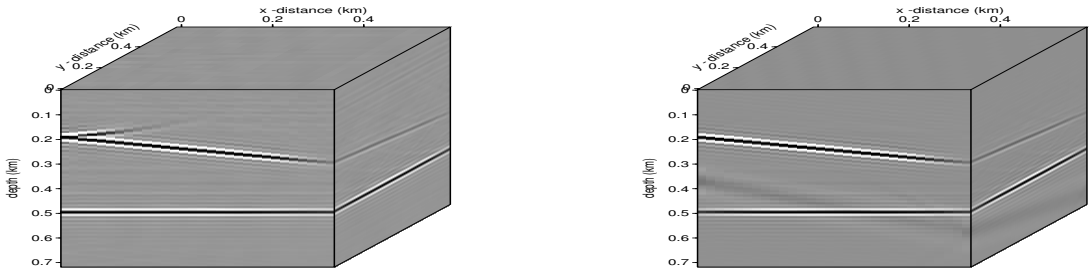

(a) (b)

Figure 1: Migrated imaged with velocity equal 1.5 km/s. (a) $\vec{p}_o - \vec{k}_s$ Stolt migration and (b) $\vec{p}_o - \vec{k}_s$ Phase-shift migration

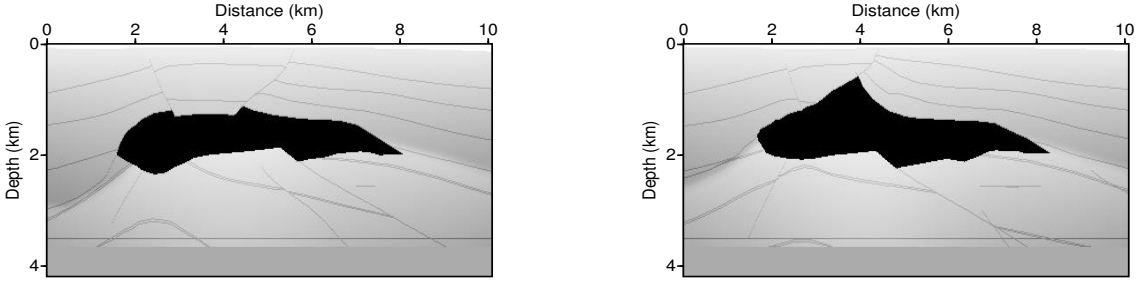

(a) (b)

Figure 2: 2-D slice of the 3-D SEG/EAEG salt model. The interval velocity in depth. (a) Line 1 and (b) line 32

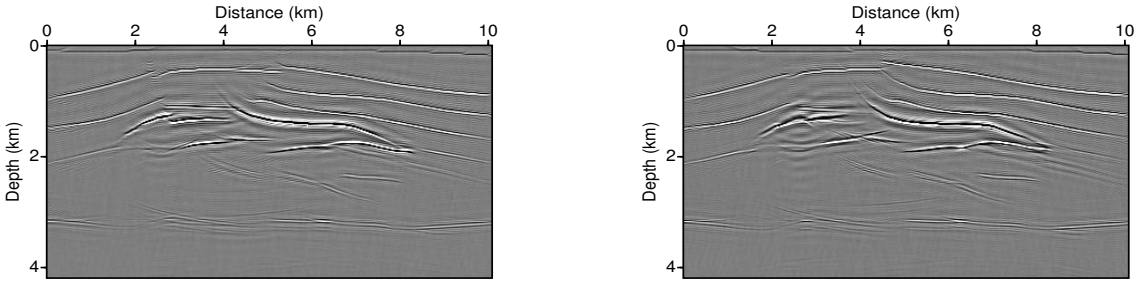

(a) (b)

Figure 3: Stolt depth migration with velocity equal to 2.5 km/s. (a) Line 1 and (b) line 32.

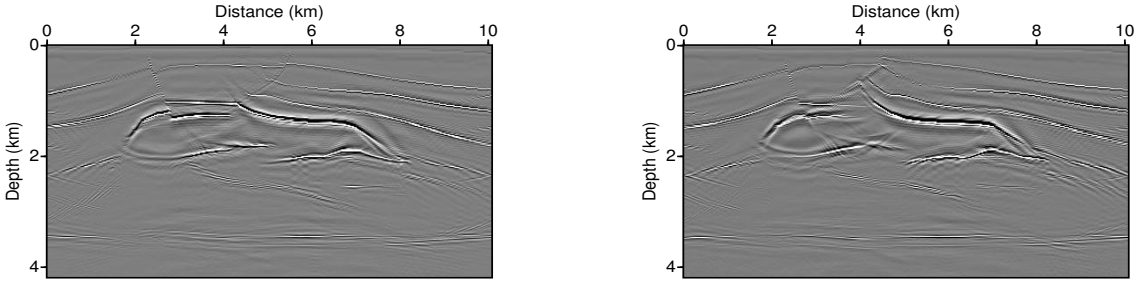

(a) (b)

Figure 4: Phase-shift migration. The vertically varying interval velocity was derived for the mean velocity in each depth interval. (a) Line 1 and (b) line 32.

An inverse-scattering sub-series for predicting the correct spatial location of reflectors without knowing or determining the propagating medium

Arthur B. Weglein[*], Douglas J. Foster[†], Kenneth H. Matson[††], Simon A. Shaw[††], Paulo M. Carvalho[†††], Dennis Corrigan[††††]
[*]University of Houston, Houston, TX, [†]Phillips Petroleum, Bartlesville, OK, [††]BP, Houston, TX, [†††]Petrobras SA, Rio de Janeiro, Brazil [††††]ARCO (retired)

Abstract

Green's Theorem predicts the wavefield in a medium from boundary measurements and knowledge of the medium properties such as wave velocity. All current wave theoretical methods for predicting the correct spatial location of reflectors in the subsurface derive from various forms of Green's Theorem. When the medium above the target is complex, current velocity analysis techniques often fail to yield an adequate velocity model, which in turn has a detrimental impact on subsequent imaging. Hence the accurate location, resolution and identification of targets beneath complex media (e.g., salt, basalt and karsted sediments) are high priority and essentially unsolved problems today.

In this paper, we present a method with the potential to precisely locate reflectors beneath complex media without a detailed knowledge of the propagating medium. In a sense, this method is able to supercede or override the requirements of Green's Theorem by providing an algorithm with the same promise but with fewer demands. The inverse scattering series is a direct multi-dimensional inversion method that achieves all tasks of inversion explicitly in terms of reference medium properties.

We introduce the purposeful perturbation concept as a means of addressing the issues most often associated with series solutions. The algorithm proposed in this paper is a task-specific inverse scattering sub-series whose purpose is the location of reflectors in the subsurface. The convergence and rate of convergence of the imaging sub-series are examined for the case of a normal-incident plane wave on a 1-D medium.

Precise prediction from imprecise input

Linear prediction (or, in general, closed-form prediction) methods typically require precise input to predict precise output. The archetypical linear prediction of depth, *d*, from constant velocity, *v*, and travel-time, *t*, is

$$d = v \times t$$

where given precise *v* and *t*, predicts precise distance (or depth), *d*.

Green's Theorem is another linear relationship between boundary measurements of a wavefield and the predicted wavefield in the medium with precise medium knowledge expressed through the Green's function of the medium, *G*.

Testing imaging methods using synthetic data and the precise model velocity as input does not actually address the relevant problem. At the very least, imaging methods need to be tested using synthetic data and a velocity model that corresponds to what would be estimated from the data using current best velocity analysis techniques. This component of realism would help focus on the relevant issue, namely, how do we achieve accurate imaging at depth given our current ability to estimate the velocity, especially under complex geologic circumstances? There are two responses to this challenge: (1) to significantly improve velocity estimation capability, and (2) to develop methods that can produce accurate images at depth without precise velocity. We support both approaches and this paper represents an effort in the second category.

The inverse scattering series is the only direct multi-dimensional inversion that doesn't assume that the actual and the estimated reference medium are equal or that they are close enough so that differences can be ignored. The reference medium is never updated and the reference is never assumed to be perfect. Hence, the method has the potential of achieving precise inversion goals, and all the tasks associated with achieving that objective, without knowing or ever determining the precise medium.

The inverse scattering series never attempts to change the imprecise input towards precise input; it predicts precise output directly in terms of the input that is recognized and anticipated to be imprecise. Since the removal of free-surface and internal multiples, the location of reflectors in space, and determining medium properties are tasks associated with inversion, the inverse scattering series provides the opportunity to achieve each of these tasks without precise reference or migration input information. Each task has a different sub-series; each has different convergence properties, and inherent need for proximity to actual properties and data requirements.

In Weglein et al. (2000), a method was described for extending the inverse-scattering equations to predict the precise wavefield at depth without knowing the propagation medium. A second approach is described in this paper: the inverse sub-series is identified that performs the imaging task of locating reflectors in their correct position in space. These inverse-scattering series concepts represent the only current candidate with the potential for achieving a precise spatial map of angle dependent reflection coefficients (imaging) without knowing, or ever determining, the propagating medium.

In this paper, the imaging sub-series is identified and analyzed, and convergence and data requirements are investigated. Initial analysis points to robust convergence properties. However, the rate of convergence appears to appreciate (and benefit from) a starting model that is proximal to the actual. Hence, we anticipate that an effective migration velocity analysis and concomitant depth migration are important starting points for this methodology. The data requirement conditions of this sub-series are also being analyzed (Shaw, 2001). All inverse-series applications require a good estimate of the source signature in the water.

The inverse-scattering sub-series for a normal incident wave on a 1-D medium

For a wave normal incident upon a 1-D acoustic medium, the pressure $P(z,\omega)$ is governed by

$$\left[\frac{d^2}{dz^2}+\frac{\omega^2}{c_0^{\,2}}(1-\alpha(z))\right]P=0 \qquad (1)$$

where ω is the angular frequency, c_0 is the homogenous reference velocity, $k = \omega/c_0$ and $V = k^2\alpha$. In this context, the inverse problem is to determine α.

$$\alpha=\alpha_1+\alpha_2+\ldots \qquad (2)$$

The first term in the general inverse-series described by, e.g., Weglein et al. (1997) reduces in this 1-D case to finding α_1 in terms of data, P_s.

$$P_s(z_m,\omega)=\int\frac{e^{ik|z_m-z'|}}{2ik}k^2\alpha_1(z')P_0(z',\omega)dz' \qquad (3)$$

where P_0 is the incident (reference) wavefield, $P_s = P - P_0$, and z_m is the location of the receiver. Using this equation, α_1 can be obtained from the scattered field (reflection data) by

$$P_s(z_m,\omega)\frac{2i}{k}e^{ikz_m}=\alpha_1(2k) \qquad (3)$$

α_1 is the familiar Born approximation for α, and corresponds to trace integration. Higher terms can be computed in terms of α_1, as described in the above reference.

$$\alpha_2(z)=-\frac{1}{2}\left[\alpha_1^{\,2}(z)+\frac{d}{dz}\alpha_1(z)\int_0^z\alpha_1(z')dz'\right] \qquad (4)$$

$$\alpha_3(z)=-\frac{1}{2}\left[2\alpha_1(z)\alpha_2(z)+\frac{d}{dz}\alpha_1(z)\int_0^z\alpha_2(z')dz' + \frac{d}{dz}\alpha_2(z)\int_0^z\alpha_1(z')dz'+\cdots\right] \qquad (5).$$

Note that Eqs. (3), (4), (5) … are the exact equations for α_1, α_2, α_3, … . These equations do not represent a perturbative approximation.

Example

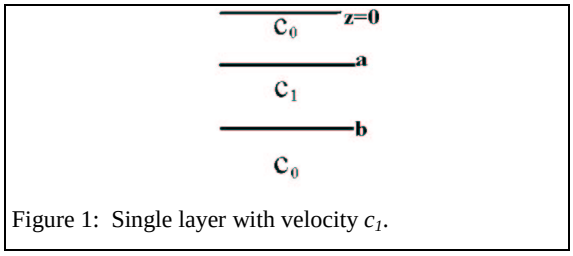

Figure 1: Single layer with velocity c_1.

For $P_0 = e^{ikz}$ and the case of a single layer with velocity c_1 (see Fig. 1) and reference c_0,

$$R_1=\frac{c_1-c_0}{c_1+c_0}\quad,\quad R_2'=-T_{01}R_1T_{10} \qquad (6).$$

T_{01} and T_{10} are the transmission coefficients going from medium 0 to 1 and 1 to 0, respectively. We assume that multiples have been removed and therefore the data consist of two primaries arriving at times t_1 and t_2

$$P_s=R_1\delta(t-t_1)+R_2'\delta(t-t_2) \qquad (7)$$

For this example, Eq. (3) becomes

$$\alpha_1=4R_1\,\mathrm{H}(z-a)+4R_2'\,\mathrm{H}(z-b') \qquad (8)$$

where $b' = a + \varepsilon\,(b - a)$ and $\varepsilon = (c_0 / c_1)$. b' is the pseudo depth that time t_2 images with velocity c_0; b' can be larger or smaller than b depending on whether $c_0 > c_1$ or $c_0 < c_1$, respectively (see, e.g., Fig. 2).

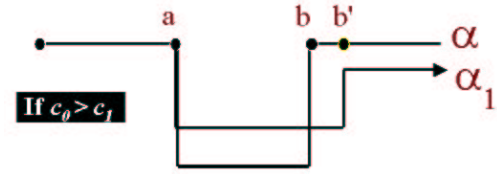

Figure 2: The relationship between α and α_1 for the case $c_0 > c_1$.

The derivative of α_1 relates to migration with velocity c_0 and provides the correct spatial location a and the incorrect spatial location b'.

Computing the second term in the series using Eq. (4), we have

$$\alpha_2(z) = -8\left[R_1 R_2'\,(\varepsilon(b-a))\,\delta(z-b') + R_1^2\,\mathrm{H}(z-a)\left(2R_1R_2' + R_2'^2\right)\mathrm{H}(z-b')\right] \quad (9).$$

This provides step functions starting at a and b´ and a delta function at b´. The step function results from the α_1^2 (z) while the δ function results from the separated contribution that is represented by $\frac{d\alpha_1(z)}{dz}\cdot\int_0^z \alpha_1(z')dz'$ (see Fig. 3).

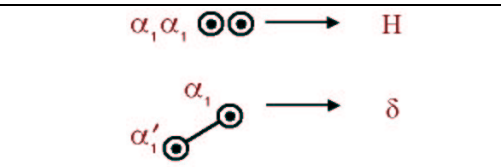

Figure 3: Interpretation of the coincident and separated contributions to the α_2 term.

For this example, higher terms in the inverse series provide additional step functions, delta functions and derivatives of delta functions at b'. The order of derivatives of delta is one less than the number of separated interactions.

The imaging sub-series

The imaging at depth sub-series corresponds to a subset of these separated diagrams where at most one upward reflection-like scattering and absolutely no downward reflection-like scattering is included. This subset is illustrated in Fig. 4, where the dots represent data migrated with G_0, and the lines represent G_0. The sum of these diagrams in Fig. 4 is the imaging series.

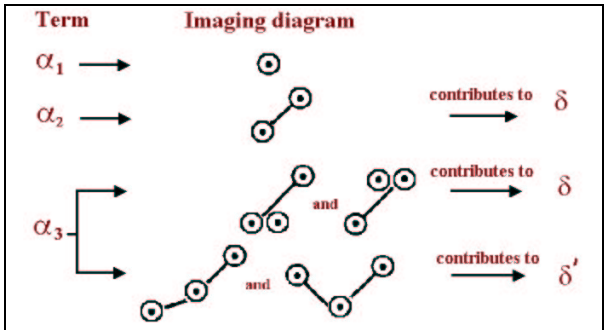

Figure 4: The reflector imaging sub-series is the sum of terms corresponding to these diagrams. Dots represent data migrated with G_0, and lines represent G_0.

Just as the "W"-diagram in Fig. 5 lead to the first term in the internal multiple elimination series, similarly the sum of the diagrams in Fig. 4 correspond to the algorithm for imaging primaries at the correct depth without the correct velocity.

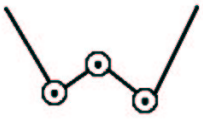

Figure 5: This type of separated diagram, with a downward reflection-like scattering, contributes to the removal of internal multiples and not to the imaging of primaries.

Basically, inverse diagrams that look like internal multiples remove internal multiples and diagrams that look like primaries process primaries. This symmetry between the construction of events in the forward series and the processing of those events in the inverse series is truly amazing. More amazing still is that this carries the possibility of imaging beneath salt without knowing the velocity.

Understanding how this works

Consider that the moving task is to take the box from (a, b') to (a,b) as illustrated in Fig. 6. Hence, since α_1 produces the (a, b') box, a task of $\alpha_2 + \alpha_3 + \ldots$ is to construct the b' to b (dashed) box. That box is

$$\mathrm{H}(z-b') - \mathrm{H}(z-b) = -\left[\mathrm{H}(z-b) - \mathrm{H}(z-b')\right] \quad (10)$$

and its Taylor series about $z - b'$ is

$$-\left[\delta(z-b')(b'-b)+\delta'(z-b')\frac{(b'-b)^2}{2}+\ldots\right].$$

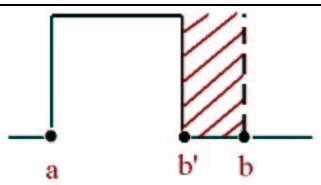

Figure 6: Interpreting the task of moving the reflector from pseudo depth b' to actual depth b.

Hence the move from false depth b' to actual depth b, is produced by this Taylor series which in turn relates to the δ, δ' in Fig. 4. Equation 10 can be written

$$\int \frac{e^{ik(z-b')}}{ik}\sum_{n=1}^{\infty}\frac{[ik(b'-b)]^n}{n!}dk \qquad (11)$$

and thus the Fourier transform of Eq. (11) converges for any finite $k(b' - b)$. For this example, the rate of convergence of the imaging series in locating the true depth, b, depends on the product $k(b' - b)$.

Purposeful perturbation: a new concept

There are issues associated with series solutions. Convergence is one; another is the rate of convergence. The classic inverse series papers (e.g., Razavy, 1975) focused only on the traditional inversion objective: identify target material properties. Typically, without knowledge of the medium, there is no guidance as to how many terms are required to reach a desired level of accuracy. It was not possible to determine the deliberate purpose of each individual term of the series as they relate to the single classic inverse objective. This has always been a drawback when using series methods and it drives the search for closed form solutions. However, there are no direct closed-form exact solutions for the multi-dimensional seismic inverse problem. To address this dilemma, we have developed a new concept: purposeful perturbation analysis. By first separating the process of inversion into tasks and identifying the location of these tasks within the inverse-series and, second, identifying the specific purpose within the task itself that each term in the sub-series performs, we allow identification of the specific benefit of each contribution to the inverse series, *totally independent of the nature of the target*. For example, a term in the inverse scattering sub-series for eliminating free surface multiples removes precisely one order of free-surface multiple completely independent of the depth of the water or any other property or characteristic of the earth. This is purposeful perturbation: the action of each term is identified totally independent of the detail of the target. The internal multiple attenuating sub-series also has this purposeful identification. We have identified an imaging sub-series and are seeking this purposeful specificity for the imaging sub-series, as well.

Conclusions

We have provided a sub-series that images at depth without the precise velocity. For a simple acoustic model in 1-D, and a normal incidence plane wave, we have shown that this series converges for all finite $k(b' - b)$, and the rate of convergence depends on the product $k(b' - b)$. We are in the process of extending this analysis to more complex multi-dimensional earth models and wavefields. Purposeful perturbation allows us to know the exact benefit provided by a finite number of terms totally independent of the specific detail of the subsurface.

References

Razavy, M. (1975) "Determination of the wave velocity in an inhomogeneous medium from the reflection coefficient": JASA, 58, pp. 956–963.

Shaw, S.A (2001) "An inverse-scattering sub-series for predicting the correct spatial location of reflectors: Initial analysis, testing and evaluation" submitted to 7th International Congress, SBGf, Salvador, Brazil.

Weglein, A.B., Gasparotto, F.A., Carvalho, P.M., and Stolt, R.H. (1997) "An inverse scattering series method for attenuating multiples in seismic reflection data": Geophysics, 62, pp. 1975–1989.

Weglein, A.B., Matson, K.H., Foster, D.J., Carvalho, P.M., Corrigan, D., Shaw, S.A. (2000) "Imaging and inversion at depth without a velocity model" 70th Annual Meeting, SEG, Calgary, Canada.

Acknowledgments

We would like to express our appreciation to ARCO, Petrobras, BP, Phillips, Federal University of Bahia, and PPPG for supporting various aspects of this research program. The support of the M-OSRP sponsors and the Margaret S. and Robert E. Sheriff Faculty Endowment is gratefully acknowledged.

Analysis of the effects of varying the anti alias filter in Kirchoff pre stack depth migration

Mark Morford, Centro Nacional de Procesado Sismologico - Pemex*

Summary

It is well known that in any pre-stack depth migration project the majority of effort is spent building the velocity model to be used in the migration. In this study, another important variable, the anti - alias filter, was studied. It was observed that varying the characteristics of the anti- alias filter had a dramatic effect on the migrated result. This study will show examples of how this process effects the seismic response and how it can influence the final interpretation.

Introduction

3d pre-stack depth imaging can be very useful in improving the seismic image in complex areas. In this particular study, Arcos Lajitas in Mexico, the depth migration was used to resolve the image beneath a package of low velocity sands which display low reflectivity and unclear form on the time migrated section. The RMS velocities from the original processing were smoothed before the time migration and do not represent the geology in the area. The idea was to better define the interval velocities and apply Kirchoff depth migration using the new velocities and re- interpret the section.

In the process of model- building, tests were run with various apertures, mutes, stretch filters and anti - alias filters in order to determine the optimum migration parameters. By nature, Kirchoff summation algorithms have aliasing problems which are amplified in the near surface. Also, this dataset is a land dataset and thus has an irregular acquisition configuration which tends to increase the amount of aliasing in the data. In the process of testing parameters and attempting to optimize the filter it was observed that the anti - alias filter applied had a dramatic impact on the resulting image.

Method

The input data for this study included CMP gathers, a 3d time migrated volume, well velocities and depths, an initial interpretation of the key horizons in the time domain and stacking velocities.

Stacking velocities were converted to interval velocities and used to build an initial velocity model. These interval velocities were then converted into velocity maps by extracting along the interpreted horizons. The velocity maps then were calibrated with the pseudo velocities from the wells. Pseudo velocities were calculated as

$$V_{int}(Pse) = 2 * (Z_{wi} - Z_{wi-1}) / (T_{mi} - T_{mi-1})$$

The interval velocity maps were then used to convert the time maps into depth maps. Having calculated both interval velocities and corresponding depths, an initial velocity-depth cube was constructed.

Using forward modeling it was determined that an aperture of 2900 meters was sufficient to image the steepest events in the depth migration. Kirchoff 3d pre-stack depth migration was then applied to every 20^{th} crossline to a depth of 5000m. These crosslines were used as the velocity control lines. The output of this process was CIP gathers (depth gathers) as well as a depth stack.

CIP gathers are very useful in refining the velocity model. Residual horizon velocity analysis was performed using the CIP gathers as input. The residual moveout semblance is a measurement of error in the velocity model along the key horizons and was interpreted at each CMP location for each of the velocity lines. These errors were then the used as input to tomography in order to update the velocity field before another iteration of migration. Some errors were found in the velocity model and 4 iterations of the pre-stack depth migration followed by tomography were necessary to determine an accurate velocity model.

At this point it was clear that there were imaging problems in various parts of the dataset. The near surface was very noisy and there were problems with imaging in the deeper section. The steep deeps in the area, which define the border of a sand/gas body were not being imaged properly. This is shown in Figure 1. We knew that this should be imaged as it was seen in the time migrated section. Looking at the gathers in the area it was clear that there was nothing wrong with the velocity model, as the reflections in the gathers were flat. Migration tests were then performed using different apertures and the events were still not imaged so it was determined that the imaging problems were not related to the aperture.

Having determined that the aperture and velocities were adequate it was clear that another variable was adversely affecting the migration image and the conclusion was that the problem was related to the anti - alias filter that was applied during the migration process. It is common in the migration to apply an anti- alias filter to remove artifacts related to operator, data and image aliasing.

Effects of anti-alias filter

Plane waves with a given frequency w_d are well- sampled and not aliased if their slopes are limited within the range determined by the condition

$$|p| \leq k_n/w_d \qquad (1.1)$$

where p is slope of the plane wave
k_n is the Nyquist wavenumber as a function of spatial sampling Δx

$$k_n = \pi / \Delta x \qquad (1.2)$$

Aliasing will take place when the condition (1.1) is violated because either the dip range is too wide, the waveform is too high frequency or the spatial sampling is too coarse(Biondi, 1999). Anti- alias filters that are typically applied in the migration are basically high- cut filters to reduce aliasing artifacts. A stronger filter reduces more artifacts and the filter applied is at a lower frequency. Since the aliasing problem is more dramatic in the shallow section, a strong filter is required to image and reduce artifacts in the near surface. However, this strong filter tends to reduce resolution in the data and can destroy signal, thus it must be applied with caution.

Example

Figure 1 shows typical results from the study area. This depth migrated section was created using a strong anti- alias filter. As indicated in the figure, important dipping events were filtered out. The flank of the reservoir of interest is not well imaged when the strong filter is applied.

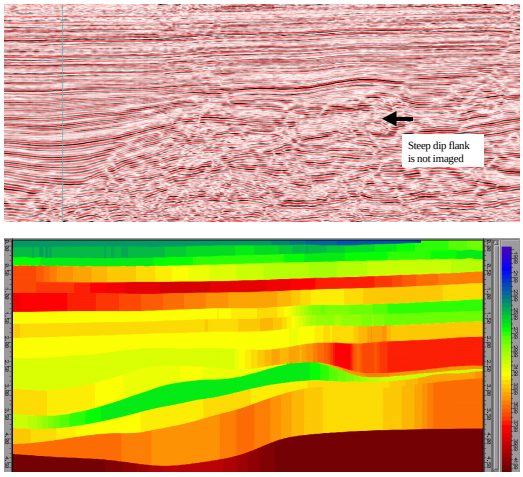

Figure 1. This depth seismic section was created using a strong filter. The lower display is the migration velocity.

Figure 2 is a zoom of the same line after pre-stack depth migration. In the upper section a strong anti- alias filter was applied while the section below it was created with a weak anti- alias filter. There are several significant differences to consider. A disadvantage of the strong filter is that it reduces the continuity of the high dip flank of the body of interest. This makes interpretation of the flank more difficult. On the other hand, the strong filter improves the deeper section by helping continuity and by accentuating fault planes and it also reduced noise in the near surface, thus making interpretation easier and more accurate in these areas. This was the case, in all the lines tested. By contrast the weak anti- alias filter does preserve the steeper dips, but produced a much noisier section and the near surface events were lost.

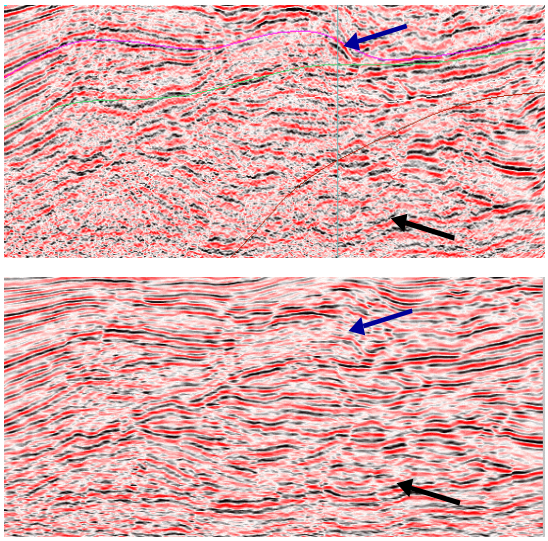

Figure 2. Zoom of the sections demonstrating differences in results due to choice of anti-alias filter. The upper section was created using a weak anti-alias while the lower section was created using a strong anti-alias filter.

The depth sections in Figure 3 are zoomed displays highlighting the near surface results. Due to the nature of Kirchoff migration and the low fold in the in the near surface, the upper part of the section in any dataset is where the aliasing effects are usually the most severe. In the section where a strong anti- alias was applied the data is more continuous and there are fewer migration artifacts. The fault planes are also more clearly defined and easier to interpret.

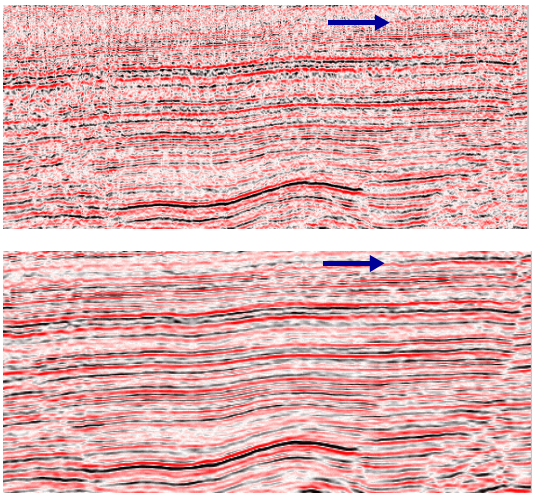

Figure 3. The near surface displays improvement in the bottom section which is with a strong anti-alias filter.

Conclusion

Most of the time and effort in a depth migration project is spent in building the velocity model which is recognized as critical in producing a good image. In this study it was shown that a frequently over-looked parameter, the anti-alias filter can also have a dramatic effect on the results. Care must be taken in designing the filter correctly in order to preserve the desired image while minimizing artifacts. It was shown that a strong filter can remove dipping events, but improve other aspects of the seismic section. Using a weak filter in migration tends to produce a very noisy shallow section and a less continuous section overall. The results for any particular dataset will vary somewhat and thus tests should be performed and analyzed with the interpreter prior to proceeding with a processing sequence.

Acknowledgements

The author would like to thank Pemex and the Centro Nacional Procesado Sismológico for providing the data and support necessary to present this work.

References

Biondi L. Biondi, 1999. 3d Seismic Imaging:Stanford Exploration Project

Lumley, D.E., Claerbout, J.F., and Bevc, D., 1994, Anti-aliased Kirchoff 3-D migration: 64th Ann. Internat. Meeting, Soc. Expl. Geophys., Expanded Abstracts, 1282-1285.

Construção de Imagens Sísmicas pelo Método de Superfície de Reflexão Comum (CRS)

Sérgio da Silva Araujo, PETROBRAS S/A, Brasil, ssa@petrobras.com.br
Martin Tygel, Depto. Matem. Aplicada, IMECC/UNICAMP, Brasil, tygel@imecc.unicamp.br

Abstract

The importance of seismic reflection in the exploration work and petroleum reservoir characterization has been greatly increasing. Its objective is to provide an image from multicoverage reflection data sets used to interpret a geological model, creating subsidies for a correct reservoir characterization. The conventional seismic imaging method (NMO/DMO stack) is a process that demands a sufficiently accurate velocity macro-model to produce correct results. This work describes a recently developed imaging concept, named the Common Reflection Surface (CRS) Stack in which only the near-surface velocity needs to be previously known. The CRS stacking operator depends on a stacking triplet parameter that is determinated in an automatic way through a search and coherence analysis procedure. For synthetic data set, the wavefront attributes obtained showed a great agreement with the expected results. The CRS method provide, not only a good quality section, but also important wavefield attributes that can be used for several purposes: macro-model velocity determination, true-amplitude imaging and layers characterization.

Introdução

Cada vez mais, o imageamento sísmico por sísmica de reflexão vem ganhando importância nos trabalhos de exploração e caracterização de reservatórios, já que uma melhor imagem estrutural da subsuperfície permite a correta interpretação do modelo geológico.

O processamento de dados sísmicos é convencionalmente realizado em coordenadas de ponto médio (x_m). Cada traço individual é atribuído ao ponto médio entre as posições de tiro e de receptor associados com aquele traço. Esses traços com a mesma coordenada de ponto médio se agrupam, compondo uma família CMP. Além das famílias CMP, famílias de afastamento comum (CO) são de maior importância. Uma família CO pode ser imaginada como uma coleção de traços que foram adquiridos trocando um único par fonte-receptor com afastamento constante ao longo da linha sísmica. Uma seção de afastamento nulo (ZO) seria o caso especial de uma seção de CO com pares fonte-receptor coincidentes ($h = 0$).

A imagem no domínio empilhado é o resultado de uma experiência hipotética (já que os receptores seriam explodidos) onde fontes e receptores são coincidentes, ou seja, a simulação de uma experiência de afastamento nulo (ZO). Pode ser obtida a partir de dados multicobertura através de métodos, como o empilhamento CMP e o processamento NMO/DMO.

Métodos para Imageamento Sísmico

Os métodos de empilhamento sísmico estão baseados em fórmulas de aproximação do tempo de percurso de um raio de reflexão na vizinhança de um raio de reflexão fixo, denominado raio central. Na quase totalidade dos casos, este raio central corresponde ao caso de afastamento nulo (raio normal), com o par fonte-receptor posicionado no CMP. A diferença entre o tempo de percurso de um raio na vizinhança do raio central (raio paraxial) e aquele do raio normal é denominado de *moveout.*

Várias expressões de aproximação do tempo de percurso existem na literatura. No caso do processamento CMP, temos o chamado *moveout* normal (NMO) para fontes e receptores na configuração CMP. Pela equação 1, percebemos a forte dependência do modelo de velocidades v no cálculo dos tempos de percurso.

$$t^2(h) = t_0^2 + \frac{4h^2}{v^2} \qquad (1)$$

Ainda na configuração CMP, temos a expressão do tempo de percurso “das hipérboles deslocadas” do método PolyStack (de Bazelaire et. al., 1994). A equação 2 mostra como este método já trabalha com 2 fatores, a velocidade média v_a e $t_p=t_0+t_r$, o que melhora a precisão dos cálculos.

$$\left(t + t_p + t_0\right)^2 = t_p^2 + \frac{4h^2}{v_a^2} \qquad (2)$$

Para fontes e receptores arbitrariamente posicionados em torno do ponto central, fugindo, assim da configuração CMP, existem fórmulas clássicas de tempo de percurso. Gelchinsky (1989) introduziu uma expressão de tempo de percurso, no âmbito do método Multifocus de empilhamento.

$$t = t_0 + \Delta t_S + \Delta t_G$$
$$\Delta t_S = \frac{\overline{SS'}}{v_0} = \frac{1}{v_0 K_S}\left[\sqrt{1+2K_S \operatorname{sen} b_0 \Delta x_S + \left(K_S \Delta x_S\right)^2} - 1\right] \qquad (3)$$
$$\Delta t_G = \frac{\overline{GG'}}{v_0} = \frac{1}{v_0 K_G}\left[\sqrt{1+2K_G \operatorname{sen} b_0 \Delta x_G + \left(K_G \Delta x_G\right)^2} - 1\right]$$

Esta fórmula (equação 3) depende de três parâmetros: o ângulo de emergência do raio normal (b_0) e as curvaturas das frentes de onda (eigenwaves) K_S e K_G

Empilhamento por Superfície de Reflexão Comum:

O método de superfície de reflexão comum (CRS), objeto deste trabalho, ainda no caso de fontes e receptores dispostos arbitrariamente em relação ao ponto central, utiliza a fórmula hiperbólica de tempos de percurso de Èervený reescrita por Schleicher et al. (1993) e Tygel et al. (1997) (equação 4).

$$t^2 = \left(t_0 + \frac{2x_m \operatorname{sen} b_0}{v_0} \right)^2 + \frac{2t_0 \cos^2 b_0}{v_0} (K_N x_m^{\ 2} + K_{NIP} h^2) \qquad (4)$$

A superfície de empilhamento CRS pode ser especificada por meio deste operador de empilhamento que depende de três parâmetros: o ângulo de emergência do raio ZO (b_0) e duas curvaturas de frente de onda hipotéticas introduzidas por Hubral (1983), representadas na figura 1. As frentes de onda de ponto de incidência normal (*NIP*) e normal (*N*).

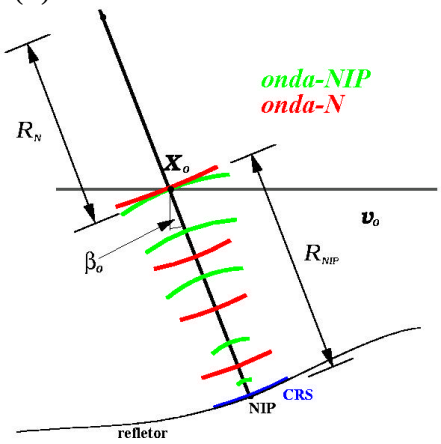

Figura 1: Os três parâmetros envolvidos nas expansões de tempo de percurso baseadas na teoria de raios paraxiais (modificado de Müller, 1999).

No aplicativo do WIT, aqui utilizado, este trio de parâmetros é determinado de um modo automático por meio de procedimento de busca e análise de coerência. O empilhamento CRS fornece, além da seção de afastamento nulo, estes importantes atributos de campo de onda que são úteis para deduzir um modelo de macro-velocidade, ao contrário do que ocorre no empilhamento convencional. O operador de empilhamento ajusta com mais coerência os eventos registrados nos dados pré-empilhados que métodos convencionais, já que utiliza pares de fontes e receptores posicionados arbitrariamente em relação ao ponto central e não apenas simetricamente a ele, como no processamento convencional. Os modelos de velocidades obtidos pelo método CRS serão, desta forma, mais confiáveis para uma futura migração, por exemplo.

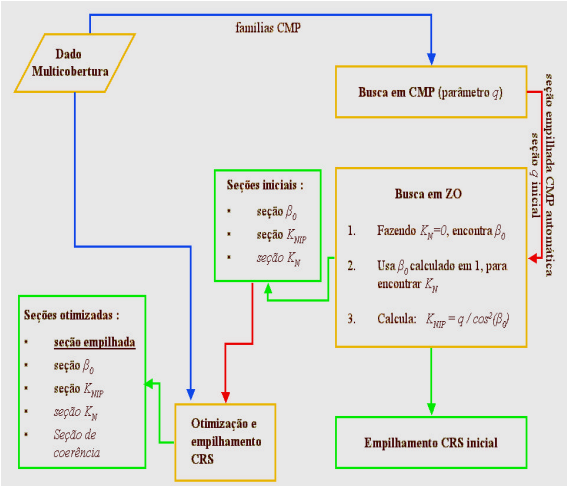

Figura 2: Fluxograma para o empilhamento CRS. Em azul são mostrados os fluxos dos dados de entrada. Em verde aparecem as seções obtidas com o método.

Modelo Sintético.

Um modelo sintético elástico bidimensional foi gerado a partir do conceito da teoria do raio, utilizando o sistema SEIS88 desenvolvido por Èervený e Pšenèík (1988). Foi também utilizado um algoritmo desenvolvido pelo Laboratório de Geofísica Matemática (LGM) da UNICAMP, que extrai os valores dos parâmetros CRS a partir do modelo elástico. Comparando os parâmetros teóricos com aqueles determinados pelo método de empilhamento CRS, a precisão da aproximação de tempo de percurso foi testada. Ruído aleatório foi acrescentado aos dados multicobertura para produzir uma relação sinal/ruído semelhante à apresentada em dados reais.

O modelo da figura 5 consiste de uma situação geológica do tipo talude, cuja geometria, junto com o forte contraste de impedância do fundo do mar, gera dificuldades para o imageamento sísmico convencional.

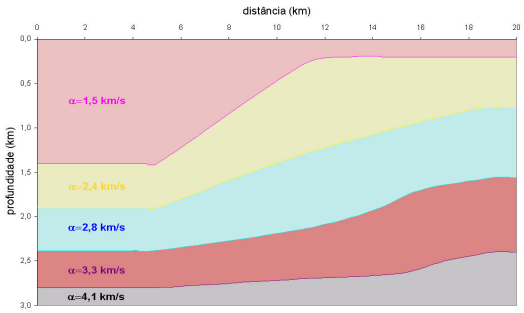

Figura 5: Modelo sintético.

Empilhamento CRS

O empilhamento CRS como detalhado no fluxograma da figura 2 é então aplicado a este dado sintético. Na primeira parte ocorre a estimativa do parâmetro combinado $q=cos^2\hat{a}_0 K_{NIP}$, por meio de uma busca mono-paramétrica nas famílias CMP extraídas dos dados multi-cobertura. A situação é semelhante a uma análise de velocidade v_{NMO} automática convencional. O empilhamento CMP automático produz então o resultado mostrado na Figura 6. A seção Empilhada CMP Automática é um resultado intermediário no procedimento de empilhamento CRS e é usada como uma aproximação de seção de afastamento-nulo (ZO), para extrair os ângulos de emergência b_0 e as curvaturas da *onda-N* K_N,.

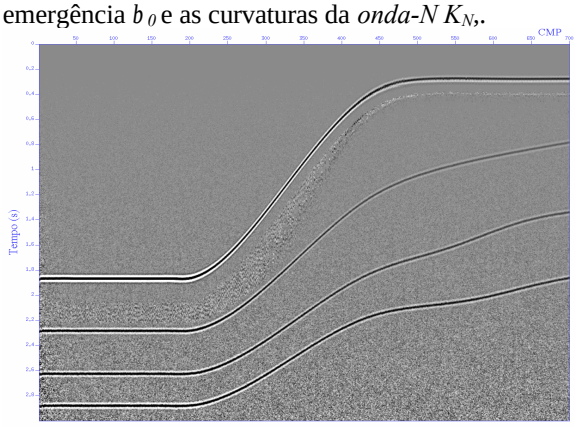

Figura 6: Seção empilhada CMP automática.

A seção empilhada CRS da figura 7 apresenta uma maior razão S/N em comparação com o resultado do empilhamento CMP automático. Esta é uma indicação para o bom ajuste das superfícies de empilhamento CRS definidas pelos parâmetros de empilhamento iniciais à resposta da reflexão modelada. Assim, o aumento no nível S/N é devido a uma soma ao longo da superfície usando muito mais traços para simular cada amostra de tempo ZO. A boa qualidade da seção empilhada CRS é observada no bom imageamento dos eventos de reflexão relativos aos flancos íngremes da zona de talude.

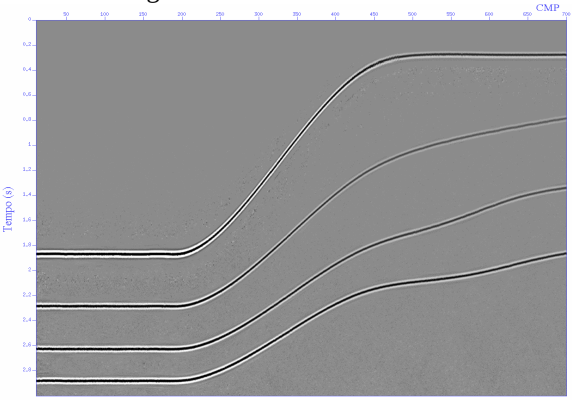

Figura 7: Seção empilhada CRS inicial..

A última parte do processo consiste na aplicação de um algoritmo de otimização. O resultado final apresenta uma seção semelhante à anterior, porém os parâmetros CRS finais são mais precisos, possibilitando uma melhor inversão do modelo. Além das seções ZO simuladas, o método de empilhamento CRS produz as seções destes atributos.

As Figuras 8 a 10 mostram uma comparação entre os parâmetros teóricos, calculados diretamente do modelo e os otimizados. Pode-se verificar que o método CRS fornece estimativas de parâmetros geralmente precisas na maioria da seção, destacando-se o ângulo de incidência. Porém, nota-se que uma maior dispersão em alguns pontos, para as curvaturas das frentes de *onda-N* e *NIP,* devido, provavelmente, ao programa usado para escolher (*picking*) os parâmetros para plotagem.

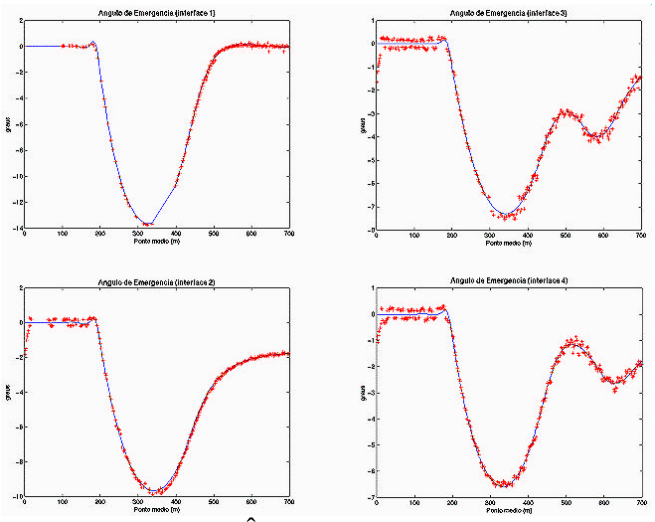

Figura 8: Ângulo de emergência b_0.

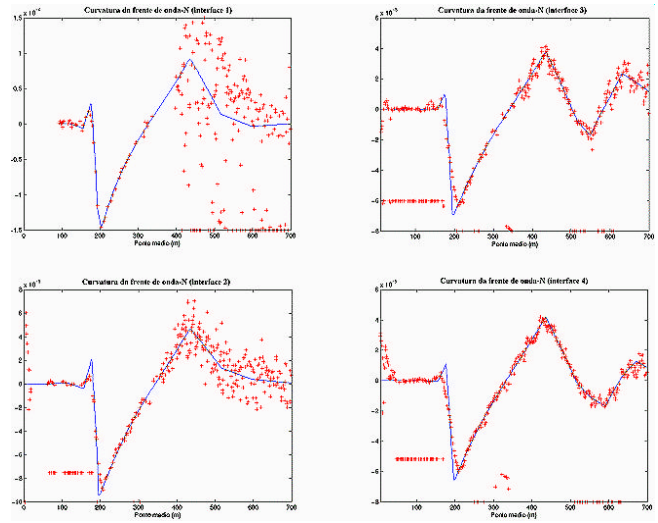

Figura 9: Curvatura da frente de *onda-N* K_N:

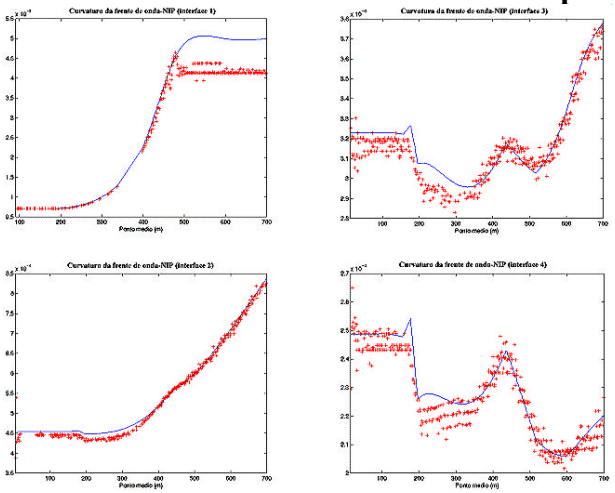

Figura 10: Curvatura da frente de *onda-NIP.*

Além da qualidade da imagem, o tempo de processamento é um fator importante para determinar o sucesso de um processo de imageamento. Tempo de processamento é definido como o tempo total necessário para completar um processo. Isto inclui tempo de CPU e o tempo gasto para ações interativas. O tempo de CPU depende do *hardware* usado e da efetividade do algoritmo implementado. Isto é fácil de medir e comparar. O tempo que o usuário precisa para processos interativos é bastante difícil estimar. Depende de fatores como a disponibilidade de uma informação a priori e das habilidades e experiência do usuário. O *hardware* utilizado neste trabalho foi uma estação *SUN – ULTRA 60*, com 2 processadores de 450 MHz e 1 Gb de memória RAM. O tempo de CPU para finalizar todo o processo de empilhamento CRS foi de quase 4 horas.

Conclusões e Perspectivas.

Como resultado de um empilhamento CRS obtém-se, além de cada amostra ZO simulada, atributos do campo de ondas importantes: o ângulo de emergência e os raios de curvatura da frente de *onda NIP* e normal. Não requer, a princípio, um modelo de macro-velocidades prévio, utiliza muito mais traços que as famílias CMP do empilhamento convencional. Assim, o método CRS fornece uma seção empilhada mais limpa, com uma melhor relação S/N.

Do ponto de vista de esforço computacional, o empilhamento CRS Inicial é bastante rápido, gerando boa qualidade da imagem. Se a simulação de uma seção ZO for o alvo principal, pode ser usado o empilhamento CRS Inicial, aplicando uma otimização orientada apenas a determinados objetivos, como em regiões de maior complexidade estrutural. Por outro lado, se os parâmetros de empilhamento CRS forem usados como parâmetros de entrada para um processo de inversão para determinar o modelo de velocidades ou outros propósitos, será necessário investir mais tempo de CPU na busca dos melhores parâmetros possíveis.

Uma opção para a implementação do método CRS comercialmente poderia ser, no caso de um reprocessamento, a utilização do modelo de velocidades e da seção ZO já obtidos com o método CMP convencional como entrada para um processo de busca do ângulo de emergência inicial.

Referências Bibliográficas

Birgin, E. G., Biloti, R., Tygel. M., Santos, L. T. Restricted optimization: a clue to fast and accurate implementation of the common reflection surface stack method. Journal of Applied Geophysics, v.42, p.143-155, 1999.

de Bazelaire, E., Viallix, J. R. Normal moveout in focus. Geophysical Prospecting, v.42, n.5, p.477-499, 1994.

Gelchinsky, B. Homeomorphic imaging in processing and interpretation of seismic data – fundamentals and schemes. In: 59th Annual International Meeting. Expanded Abstracts, Society of Exploration Geophysicists, 1989. p.983.

Hubral, P. Computing true-amplitude reflections in a laterally inhomogeneous earth. Geophysics, v.48, p.1051-1062, august 1983.

Müller, T. The common reflection surface stack method – Seismic imaging without explicit knowledge of the velocity model. Ph. D. thesis. Karlsruhe University, 1999, 132p.

Tygel, M., Müller, T., Hubral, P., Schleicher, J. Eigenwave based multiparameter traveltime expansions. In: 67th Annual International Meeting. Expanded Abstracts, Society of Exploration Geophysicists, 1997. p.1770-1773.

Agradecimentos

O primeiro autor gostaria de agradecer à PETROBRAS por permitir a publicação deste trabalho. Saliento, também a grande ajuda do colega Eduardo Filpo durante o curso deste trabalho.

CRS as a tool for true amplitude imaging

R. S. Portugal, R. Biloti, L. T. Santos and M. Tygel

State University of Campinas, Brazil

Abstract

We present a method to obtain a true-amplitude migration and amplitude-versus-angle (AVA) at selected points using the attributes generated by the Common Reflection Surface (CRS) Stack. Our approach combines the CRS stack/inversion process applied to multicoverage data, together with the use of a kinematic Kirchhoff migration, to achieve true-amplitudes (TA) at assigned depth points of the migrated images. The proposed method consists of the following steps: (i) apply the CRS process to the given multicoverage data; the obtained CRS attributes are next used to produce a simple macro-velocity depth model; (ii) perform an unweighted Kirchhoff migration for imaging purposes only; for selected points on target reflectors in the migrated image, we use the macro-velocity model to determine, by ray tracing, common-reflection-point (CRP) gathers that belong to the input data; for these rays, we compute the incident angles and the geometrical spreadings; (iii) go back to CRP gathers and compensate the amplitudes for geometrical spreading. The results permit to construct AVA curves on the assigned CRPs. In summary, our method is designed to aggregate amplitude information on selected points of a reflector, after a purely kinematic image (migration) has been obtained. The method is tested on a synthetic inhomogeneous layered model with good results.

Introduction

One of the main objectives of processing seismic reflection data for hydrocarbon prospecting is to obtain meaningful images of the geological structures, in particular reservoir structures in the subsurface. The geological structures to be imaged are defined by seismic reflectors.

Kinematical images, in which only the location and orientation of the reflectors (with no regard to amplitudes) are considered, can be achieved, for example, by efficient Kirchhoff migration procedures using simple weights or no weights at all. Kirchhoff migration requires a given macro-velocity model. Moreover, special methods exist to combine the migration outputs to update the model, so as to refine and improve the image. The final result is, in many cases, a fairly adequate (kinematical) image of the structures of interest.

The problems that concern us in this paper is how to aggregate dynamical information (amplitudes) to the obtained image. In fact, the amplitudes are needed essentially on selected points at key interfaces, where the determination of angle-dependent reflection coefficients is the most desirable information.

According to zero-order ray theory, the amplitude of a primary-reflection event can be described by

$$U = \mathcal{A}\,\frac{R_c}{\mathcal{L}}\,, \qquad (1)$$

where R_c is the angle-dependent reflection coefficient of the primary reflection ray and θ is the incidence angle of that ray with respect to the interface normal. The reflection coefficient is the quantity of interest to be estimated from the data. The quantity $\mathcal{L}$ is the angle-dependent geometrical-spreading factor of the reflection ray. It accounts for the amplitude variations due to focusing and defocusing of the energy carried by the ray along its ray path. All factors which affects amplitudes other than the geometrical spreading are combined and represented by overall quantity $\mathcal{A}$ in equation (1). The geometrical spreading, $\mathcal{L}$, is generally singled out as one of the major sources of amplitude distortion in the observed data. That is the reason why the term *true-amplitude* is typically attached to a primary-reflection amplitude that has been corrected for geometrical spreading.

In the case of depth migration, the term *true-amplitude* (TA) migration refers to the case in which the migration output equals the observed amplitudes automatically corrected for geometrical spreading (see, e.g., Hubral *et al.*, 1996). Full TA algorithms are significantly more expensive and time-consuming than their kinematic unweighted counterparts. As another complication, the accuracy requirements on the macro-velocity depth model are higher for the application of TA migration than for purely kinematic migration. The flexibility of using migration outputs to update the velocity model is lost when such a heavy migration algorithm is applied. As a last, and probably the best, argument against the application of a full TA migration algorithm to an overall region is that, in fact, the amplitude information is required only

on some specific target points or reflectors. Away from these points, the obtained amplitudes are not useful.

In this paper, we propose a method to aggregate true amplitudes (i.e., observed primary-reflection amplitudes after geometrical-spreading correction) at selected CRPs of interest, after an image of the subsurface has been obtained. This image can be, for example, the result of one or several kinematic migrations.

Strategy

The kernel of the method is summarized by the fluxogram shown in Figure 1. Our strategy is mainly divided in three steps: CRS attribute extraction & macro-model inversion, kinematic imaging through unweighted Kirchhoff migrations and subsequent geometrical spreading corrections in the input data.

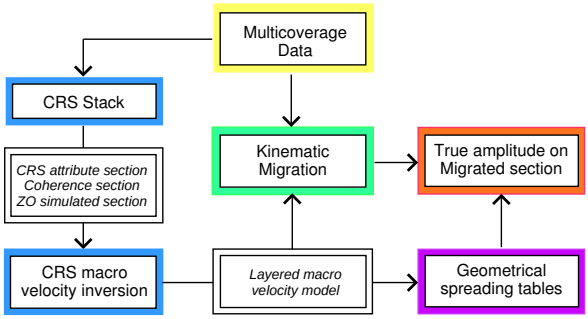

Figure 1: Fluxogram.

CRS stack. The 2-D common-reflection-surface (CRS) stack (see, e.g., Müller 1999), applied to multicoverage data on a seismic line, is designed to produce a stacked section (an approximation of a zero-offset section), together with three auxiliar sections of CRS attributes and a coherence section.

For each fixed central point (e.g., a CMP location of the original data), on which the output trace is to be computed, the CRS uses a multiparametric traveltime formula to stack all data that correspond to arbitrary source and receiver locations in the vicinity of that point. In this sense, it differs significantly from the conventional NMO/DMO stack (that employs only reflections from CMP gathers) to achieve much more redundancy with a consequent improvement of signal-to-noise ratio. The three CRS attributes assigned to each point of the stacked section are the parameters of the traveltime moveout formula. These are the emergence angle of the normal reflection ray and the wavefront curvatures of the NIP- and N-waves that arrive at that point. For the definition of the NIP-wave and the N-wave, the reader is referred to the original paper of Hubral (1983).

The CRS attributes are extracted upon the use of coherency analysis strategy directly applied to the data. The determination of more efficient and accurate parameter extraction methods is a topic of active research (Birgin *et al.*, 1999).

CRS macro-velocity model inversion. The philosophy of the CRS Stack method is to use as much data as possible during the stacking process. Therefore, the most relevant events are better defined on the stacked section and available for further inversion.

The input data for CRS velocity inversion are the CRS attributes that refer to those selected target reflections. Also the near-surface velocity field needs to be known. In fact, this is already a requirement for the application of the CRS method.

The classical layer-stripping velocity inversion algorithm of Hubral and Krey (1980) can be recast in terms use of the CRS, inverts iteratively on the depth the homogeneous layer velocities and the interface positions. The interfaces are constructed as cubic splines, which are suitable for further blocky ray tracing algorithms.

Kinematic image. As soon as the homogeneous layered velocity model is provided by the CRS inversion, it is smoothed in order to perform a kinematic migration. The traveltime tables are generated on the fly by the wavefront construction method, therefore each seismic trace can be migrated independently from each other. To enhance the signal-to-noise ratio, the final image is built by stacking all common-offset migrated section, this section is called stacked migrated section.

Geometrical spreading correction. On the stacked migrated section, it is possible to choose depth points on a target reflector. For each one chosen point, using the approximated homogeneous layered model, we compute, by standard dynamic ray-tracing, the traveltimes, the incident angles and the geometrical spreading factors. These quantities help to extract a common-reflection-point (CRP) gather from the original data. For each trace, using the computed reflection traveltime, we can pick

the amplitude, which is multiplied by the corresponding geometrical spreading factor. Applying this successively for all traces in the CRP gather, we obtain the desired AVO/AVA curves.

Synthetic example

The synthetic model, depicted in Figure 2, is composed by four layers separated by smooth interfaces. The first and fourth layers are homogeneous with constant compressional velocity of 2.0 km/s and 2.7 km/s, respectively. The second and the

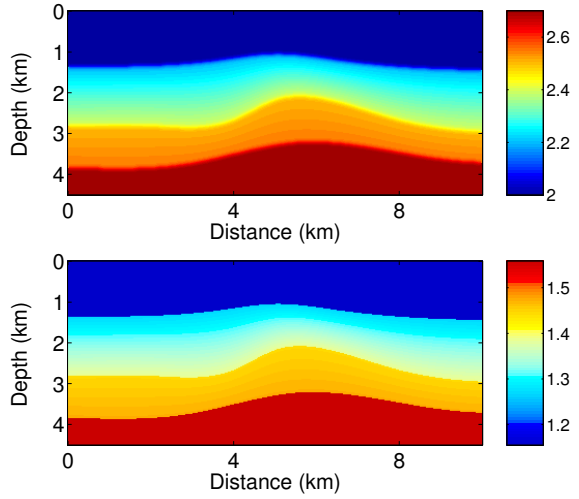

Figure 2: Velocity model for synthetic data. Top: compressional velocity. Bottom: shear velocity.

third layers are inhomogeneous, and their velocities are composed as a linear combination of the velocity just below the upper interface of the layer and the velocity just above the lower interface that bounds the layer. For those layers, the compressional velocity varies from 2.2 km/s to 2.4 km/s and from 2.5 km/s to 2.55 km/s, respectively. The shear velocity in each point of the model is the compressional velocity divided by $\sqrt{3}$, and the density is unitary in the whole model. The multicoverage data is composed by 501 common-source experiments, where the sources are 20 m spaced. Each CS section has 151 receivers 20 m spaced. The ratio signal-to-noise in the data is 7:1. Figure 3 shows a typical common-offset section.

Each common-offset section was migrated separately, and then stacked to generate a stacked migrated section, depicted in Figure 4. The velocity model employed on the migration process (Figure 5) was obtained from the CRS attributes by

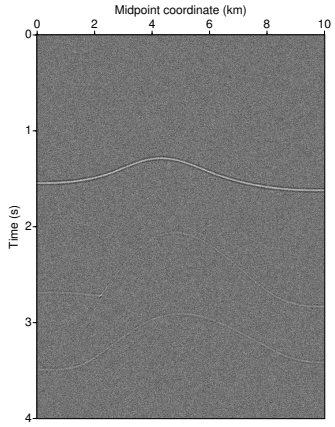

Figure 3: A typical common-offset section for the offset 1500 m.

the inversion process briefly describe above. Note that the inverted model is as accurate as possible, since only homogeneous layers could be inverted.

Using this kinematic image we have chosen a point locate on the second interface to analyze the amplitude variation (AVO and AVA curves). Figures 6 and 7 show the CRP section and the AVO and AVA curves for the selected point, respectively.

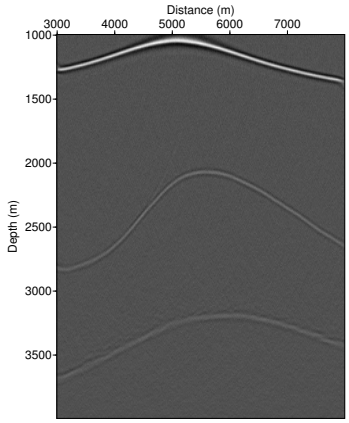

Figure 4: Stacked migrated section.

Conclusions

We have presented a method which provides a complete process to obtain AVA curves for chosen points on target interfaces. It is mainly composed by three steps: (i) construction of a layered macro-velocity model by using CRS attributes (obtained from the multicoverage data); (ii) kinematic migration of data using that macro-velocity model; (iii) *a*

posteriori correction of amplitude of chosen points on the migrated section (using traveltime, reflection angle and geometrical spreading computed on the approximated model). The numerical results are encouraging, concerning accurancy and computational effort. As a next step, further tests in real data will be carried out.

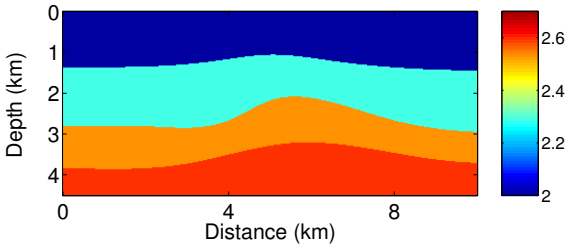

Figure 5: Compressional velocity model obtained by the CRS inversion algorithm.

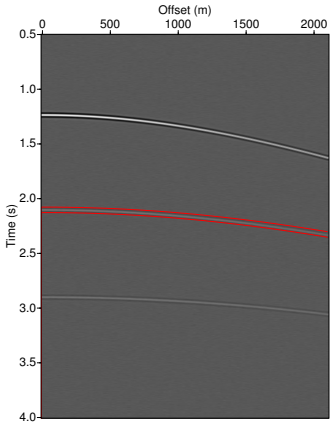

Figure 6: CRP section for the selected point on the second interface. The red tube confines the region where the picking process was carried out. This region was found out by the traveltime estimation that came out of the modelling process.

Acknowledgments

This work was partially supported by FAPESP (Grants 97/12125-8 and 97/12318-0) and by the sponsors of the WIT Consortium.

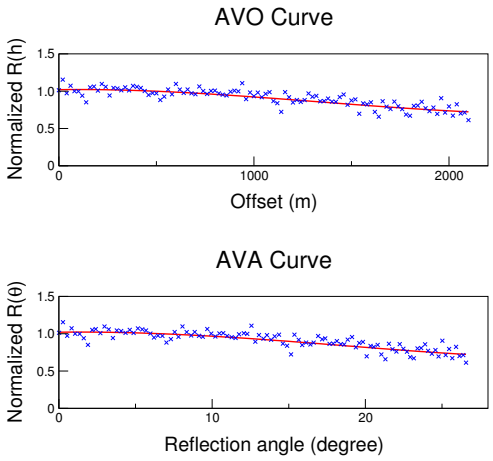

Figure 7: AVO and AVA curves for the chosen point on the second interface. The solid red line is the expected normalized reflection coefficient. The blue crosses are the picked amplitude correct for geometrical spreading, computed on the approximated model, and normalized.

References

Birgin, E. G., Biloti, R., Tygel, M., and Santos, L. T., 1999, Restricted optimization: a clue to a fast and accurate implementation of the common reflection surface method: Journal of Applied Geophysics, **42**, 143–155.

Hubral, P., and Krey, T., 1980, Interval velocities from seismic reflection time measurements: Soc. of Expl. Geophys.

Hubral, P., Schleicher, J., and Tygel, M., 1996, A unified approach to 3-d seismic reflection imaging, part i: Basic concepts: Geophysics, **61**, no. 03, 742–758.

Hubral, P., 1983, Computing true amplitude reflections in a laterally inhomogeneous earth: Geophysics, **48**, no. 08, 1051–1062.

Müller, T., 1999, Common reflection surface stack method – seismic imaging without explicit knowledge of the velocity model: Ph.D. thesis, Geophysical Institute, Karlsruhe University, Germany.

Deepening the use of time migration

Carlos A. Cunha[†] *and Andre Romanelli Rosa*[†]

Abstract

We describe an imaging method based on Kirchhoff integral which can be defined as an intermediate process between time and depth migration. If we take the first two terms of the Taylor expansion of the velocity field associated with a single diffraction, it is possible to analytically construct the diffraction surface related to a point diffractor inserted in a constant velocity gradient medium. Selected exemples ilustrate the potential of the method, as well as the steps required to build the migration velocity-gradient field.

Introdução

Apesar de a migração pré-empilhamento em profundidade já ser uma técnica madura e amplamente difundida na indústria do petróleo, boa parte dos dados processados hoje em dia são ainda migrados em tempo, embora antes do empilhamento e não mais após, como era prática comum durante a década de 80. A principal razão para isto está no esforço requerido (não apenas computacional, mas também humano) para obter o modelo de velocidade adequado para produzir uma imagem nítida e precisa da sub-superfície. A migração em tempo, em grande parte dos casos, é capaz de produzir uma imagem de qualidade similar à obtida em profundidade com um esforço significativamente menor.

Uma das formas de diferenciar estes dois "tipos" de migração (tempo/profundidade) está na forma como o operador de extrapolação do campo de ondas registrado incorpora o campo de velocidade representativo das rochas em sub-superfície. Enquanto a migração em profundidade trabalha com um campo de velocidades complexo, com definição detalhada das velocidades locais (intervalares) de propagação, a migração em tempo "enxerga" apenas o efeito cumulativo (ou médio) das rochas atravessadas pela onda em sua trajetória de ida e volta entre a superfície e as diversas interfaces refletoras.

Na migração em profundidade os tempos de trânsito associados a uma difração são obtidos pela integral de trajetória da vagarosidade da fonte ao difrator e deste ao receptor. Para o caso da migração em tempo tradicional, assume-se uma velocidade única para focalizar um ponto difrator, ou seja, procura-se definir um meio homogêneo cuja difração gerada melhor aproxime (segundo algum critério definido) a difração gerada pelo meio heterogêneo real. Dependendo do tipo de parametrização utilizada para descrever uma difração, a velocidade estimada de propagação do campo de onda gerado por um ponto difrator $M(\mathbf{r_0})$ será dada por

$$\begin{aligned} v(\mathbf{r_0};\mathbf{r}) &= v(\mathbf{r_0}) \quad \rightarrow \quad \text{migração em tempo,} \\ v(\mathbf{r_0};\mathbf{r}) &= v(\mathbf{r}) \quad \rightarrow \quad \text{migração em profundidade} \end{aligned}$$

onde $\mathbf{r_0} \equiv (x_0, y_0, z_0)$ corresponde a posição do ponto difrator e $\mathbf{r} \equiv (x, y, z)$ as coordenadas do meio no qual a onda se propaga. Teremos para o caso de afastamento nulo entre fonte e receptor que a cinemática da difração real é aproximada por um hipérbolóide no domínio (x, y, t).

O caminho natural para se construir um processo intermediário entre caracterizar a difração com uma velocidade única ou através de um campo de velocidade com variação ampla é a introdução de um campo com gradiente constante de velocidade. Neste caso, a velocidade de focalização de um ponto difrator $M(\mathbf{r_0})$ passa a ser dada pelos dois primeiros termos da expansão de Taylor do campo de velocidade em torno do ponto difrator

$$v(\mathbf{r_0};\mathbf{r}) = v(\mathbf{r_0}) + \mathbf{g}(\mathbf{r_0}) \cdot (\mathbf{r} - \mathbf{r_0}) \qquad \text{ou seja,}$$

$$v = v_0 + g_x(x - x_0) + g_y(y - y_0) + g_z(z - z_0)$$

Neste tipo de meio a trajetória dos raios é descrita por um arco de círculo e tanto esta quanto o tempo de trânsito possuem solução analítica (Slotnick, 1959). Deve-se notar que a curvatura do raio introduzida como mais um parâmetro na descrição cinemática implica não apenas em um maior grau de liberdade para aproximar a superfície de difração no domínio (x, y, t) como também na possibilidade do imageamento do difrator não ficar restrito à vertical abaixo do topo da difração. Fica claro que, embora geneticamente próxima à migração em tempo, a introdução do gradiente leva a uma migração que se enquadra plenamente no conceito de migração em profundidade. A difração será imageada em algum ponto ao longo do raio imagem que atravessa verticalmente a superfície na posição do topo da curva de difração.

[†]Petrobras S.A., Brasil

Cinemática com gradiente

De forma similar às migrações Kirchhoff tradicionais no domínio do offset comum, uma amostra de saída (ponto difrator) é obtida a partir da integração das amostras do cubo de offset comum de entrada que se encontrem sobre a superfície de difração. Uma amostra com coordenadas $[x_0, y_0, z_0]$ no cubo de saída receberá contribuição de um traço de entrada no tempo t dado por $t = t_s + t_r$, onde t_s = tempo de trânsito do difrator à fonte e t_r = tempo de trânsito do difrator ao receptor. O processo de obtenção destes tempos é descrito a seguir.
Primeiro obtem-se o plano ξ' que contém simultaneamente o ponto difrator $\mathbf{r_0} \equiv (x_0, y_0, z_0)$, o ponto da fonte $\mathbf{r_s} \equiv (x_s, y_s, z_s)$ e ainda o vetor gradiente de velocidade $\mathbf{g} \equiv (g_x, g_y, g_z)$. A partir deste plano, do vetor gradiente e do ponto difrator define-se um novo sistema de coordenadas com origem em $[x_0, y_0, z_0]$, direção z' coincidente com a direção do gradiente, direção x' perpendicular a z' e contida no plano ξ', e direção y' perpendicular ao plano.
Neste sistema de coordenadas, são utilizadas as equações válidas para descrever a cinemática de meios com gradiente vertical de velocidade (Slotnick, 1959; Telford et al. 1976). São obtidos assim os tempos de trânsito, ângulos de chegada e partida e a distância percorrida pelo raio.

Análise de velocidade-gradiente

Um ponto chave para a implementação do método é naturalmente o processo de estimativa dos parâmetros que definem o modelo de velocidade a ser usado na migração. A análise de velocidade em profundidade se torna impraticável devido ao movimento vertical do evento analisado para diferentes velocidades e gradientes. Particularmente importante na escolha do par $[v_0, g_x]$ é a análise de fatias de profundidade constante do cubo de coerência medida ao longo do offset $[Coe(v_0, g_x, z)]$ que fica inviabilizado pela mobilidade vertical do evento. Para piorar a situação, observa-se que o evento se move também na horizontal em função dos parâmetros v_0 e g_x. Estas dificuldades no entanto podem ser contornadas utilizando-se o conceito de raio imagem (Hubral, 1977). Considerando-se – para um meio com gradiente definido – o raio que parte do difrator e chega verticalmente à superfície, realiza-se uma transformação de coordenadas da profundidade z para o tempo τ medido ao longo deste raio. O procedimento para este tipo de análise é exposto a seguir para o caso 2-D com gradiente na direção x.

- O ponto escolhido para a análise (x_a, τ_a) refere-se a uma posição fixa na superfície, apartir da qual é traçado um raio imagem. O ponto atingido pelo raio no tempo τ define o ponto difrator (x_0, z_0) a ser usado como origem para os raios envolvidos na análise. As coordenadas desta origem variam em função da velocidade e do gradiente analisados.
- O ponto de referência para o par (v_0, g_x) interpretado é também a posição (x_a, τ_a).
- O resultado final da análise é uma tabela de pontos interpretados representados por $v_0(x_a, \tau_a)$ e $g_x(x_a, \tau_a)$.

Tanto a análise de velocidade quanto a própria migração realizadas segundo este conceito de raio imagem constituem na verdade uma forma de imageamento em tempo, onde o difração colapsada é posicionada verticalmente sobre o topo da difração. Esta versão em tempo da migração com gradiente pode ser expressa de uma forma bem mais simples a partir de uma extensão da equação cinemática da dupla raiz quadrada para gradiente zero, com as velocidades dadas por

$$v_{0s} = v_0 + g_x(x_0 - x_s)/2 \quad (1)$$
$$v_{0r} = v_0 + g_x(x_0 - x_r)/2 \quad (2)$$

onde x_0, and t_0 definem a posição do ponto difrator, t é o tempo onde a curva de difração intercepta o traço com coordenadas de fonte e receptor dadas por x_s e x_r respectivamente e v_0 e g_x são a velocidade e gradiente também na posição do ponto difrator.
Caso se deseje migrar o dado em profundidade a partir dos dados interpretados em tempo, torna-se necessário mapear os pares $[v_0, g_x]$ do domínio (x_a, τ_a) para o domínio (x_0, z_0), novamente através do raio imagem. A interpolação espacial destes pontos deve ser realizada com mais cuidado que a interpolação em tempo devido ao maior grau de irregularidade observada após esta transformação.

Alguns exemplos ilustrativos

Para testar a sensibilidade deste método de imageamento aos parâmetros envolvidos no processo foram gerados dados sintéticos 2-D pelo método Kirchhoff utilizando-se um modelo (denominado Modelo 1) constituído por um refletor plano a 500 metros de profundidade em um meio com gradiente

horizontal de velocidade $g_x = 0.5$ Hz e velocidade na posição de referência igual a 2000 m/s. Os offsets variam de 0 a 1180 metros.
Estes dados foram migrados com diferentes valores de velocidade de referência v_0 e diferentes valores de gradiente horizontal g_x. Os painéis na figura 1 mostram um mesmo CRP migrado com diferentes valores de gradiente para uma velocidade fixa (esquerda) e diferentes valores de velocidade para um gradiente fixo (direita). Esta última é equivalente a uma análise de velocidade convencional. Fica claro nestas figuras que apenas a migração realizada com os valores corretos de velocidade e gradiente foi capaz de adequadamente imagear o refletor para todos os offsets.

Para determinar o efeito da correção indevida dos

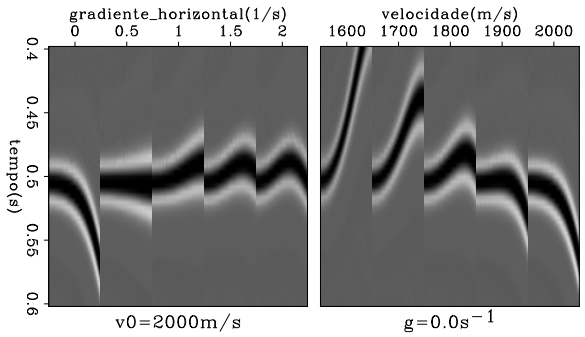

Figure 1: ESQUERDA: registros associados a um CRP migrado com uma mesma velocidade de referência $v_0 = 2000$ m/s e cinco valores diferentes de gradiente horizontal de velocidade. DIREITA: registros associados a um CRP migrado com um mesmo gradiente horizontal de velocidade $g_x = 0.0$Hz e diferentes velocidades de referência.

CRPs na imagem final obtida pelo empilhamento dos diversos offsets foi gerado um novo modelo (Modelo 2), consistindo de um refletor plano a 700 m de profundidade com um canal em forma de "V", inserido num meio com mesmas caracteristicas de velocidade e gradiente do modelo 1 e gerados dados sintéticos pelo método Kirchhoff.
Estes dados foram migrados em tempo com o método Kirchhoff convencional (difrações com velocidade constante), utilizando-se para cada posição de saída uma velocidade diferente definida a partir do gradiente de velocidade correto, ou seja, cada difrator é imageado com uma velocidade diferente porém constante. A figura 2 contém quatro painéis referentes a aplicação da migração acima descrita com diferentes valores da velocidade de referência. O quinto painel corresponde a migração em tempo através do método Kirchhoff com gradiente usando-se os valores corretos para velocidade de referência e gradiente, enquanto o sexto painel corresponde à versão em profundidade desta migração. A análise destes painéis mostra claramente que a imagem obtida com o método proposto é mais nítida e com melhor fase que as demais, além de possibilitar uma estimativa mais correta da velocidade do meio.

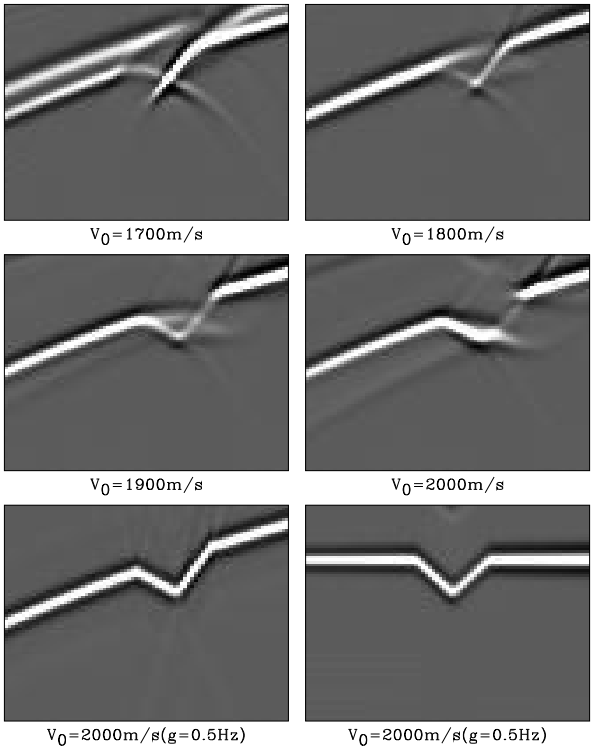

Figure 2: Os quatro painéis de cima mostram os resultados do empilhamento da migração em tempo dos dados sintéticos gerados a partir do Modelo 2 utilizando-se o método tradicional (sem gradiente) de Kirchhoff com diversos valores da velocidade de referência. O painel de baixo à esquerda corresponde a migração em tempo (raio imagem) com o método aqui descrito usando-se o gradiente de velocidade correto, enquanto o painel de baixo à direita corresponde à versão em profundidade da migração com gradiente.

Aplicação a dados reais

O método foi aplicado a dados de águas profundas da bacia de Campos, numa região com ocorrência de diápiros salinos. A análise de velocidade/gradiente-horizontal foi realizada através de um procedimento semi-automático. Ini-

cialmente, foi realizada uma análise de velocidade convencional para migração pré-empilhamento (gradiente=0) em alguns CRPs equi-espaçados. A partir dos pontos interpretados foram realizadas migrações com várias velocidades em torno da velocidade interpretada, cada uma delas com vários gradientes, para uma pequena janela de tempo em torno do tempo interpretado. Calculou-se então um plano de coerência ao longo do eixo de offsets, buscando-se os valores de velocidade e gradiente associados à coerência máxima. A Figura 3 mostra um plano de coerência correspondente a um dos pontos interpretados. A velocidade original era 1975 m/s (máximo valor de coerência para a linha de gradiente nulo) e a nova passou a ser 2025 m/s correspondente a um gradiente de -0.25 Hz.
As Figuras 4 a e b mostram um trecho dos dados migrados em tempo antes do empilhamento com as velocidades interpretadas originalmente (4-a) e migrados, também em tempo porém com o método do gradiente, usando-se o campo de velocidade/gradiente-horizontal obtido pelo processo acima descrito (4-b). Existe uma melhora significativa na definição das falhas e de diversos eventos notadamente na parte inferior da seção. É importante frisar que as migrações aplicadas foram 2-D, e uma vez que tais dados se encontram em uma região estruturalmente perturbada pela proximidade de um diápiro, o imageamento correto irá requerer a aplicação de migrações 3-D.

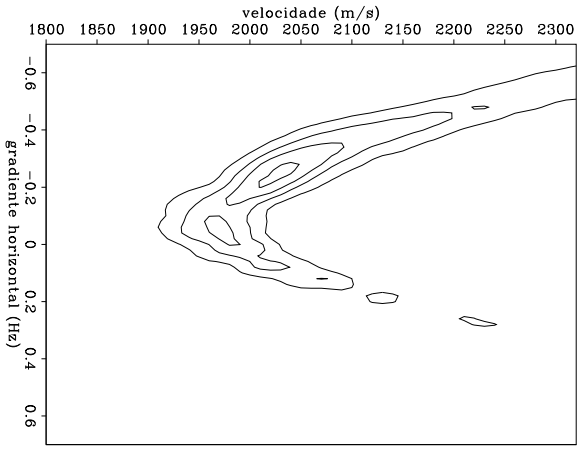

Figure 3: Plano de coerência referente a um ponto de análise do dado mostrado na Figura 4.As linhas de contorno mais internas correspondem aos maiores valores de coerência.

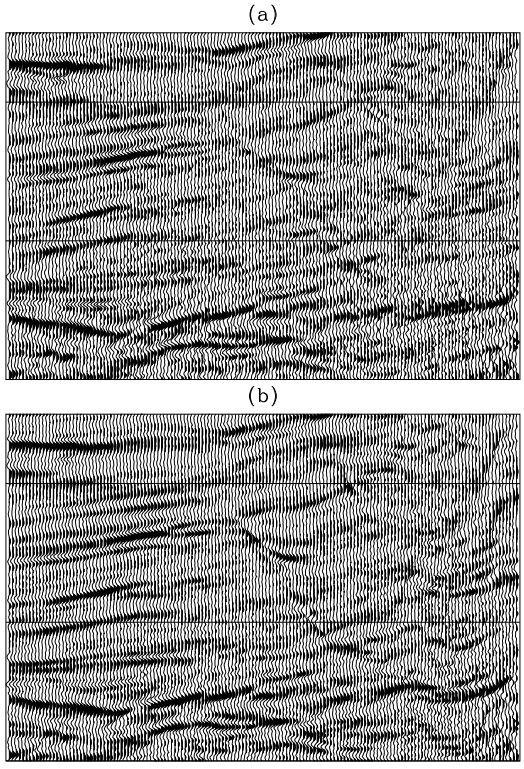

Figure 4: (a) Trecho de um dado migrado em tempo antes do empilhamento com velocidades interpretadas. (b) Mesmo trecho migrado com o uso do gradiente horizontal e o campo de velocidade-gradiente ajustado por análise automática de coerência.

Conclusões

O método proposto se mostra promissor para melhorar o imageamento em áreas de complexidade estrutural moderada com um esforço computacional e humano menor do que o exigido para a aplicação da migração em profundidade.

Referências

Hubral, P., 1977, Time migration - Some ray theoretical aspects: Geophys. Prosp., **25**, no. 04, 738–745.
Slotnick, Morris M., 1959, Lessons in seismic computing *: Soc. Expl. Geophys.. (* Edited by R. A. Geyer)
Telford, W.M., Geldart, L.P., Sheriff, R.E., and Keys, D.A., 1976, Applied Geophysics. Cambridge University Press.
Liner, C., 1996, Seismos: The Leading Edge of Geophys., **15**, no. 10, 1156–1158.

Depth Imaging using FTG Gravity and Pre-Stack Seismic Depth Migration: Case Studies from the Deepwater Gulf of Mexico

Holly Huston, Hunter 3-D Inc., Craig Barker and Mary Murphy, Unocal Deepwater USA, Jonathan Finstuen, Unocal do Brasil, and Elizabeth Johnson, Unocal E&P Technology

Abstract

In the deepwater GOM, allochthonous salt bodies obscure seismic imaging of deeper geologic features. Gravity and full tensor gradient (FTG) data, which respond to the significant density contrasts associated with the salt bodies, are highly useful when integrated into the pre-stack depth migration (PrSDM) imaging workflow for sub-salt targets. In this paper, we will discuss:

- What is Full Tensor Gradient (FTG) data?
- Why is it important?
- How do we use it for depth imaging?
- What improvements have been realized when we incorporate FTG data into depth imaging in the Deepwater GOM, and what factors enabled high quality results?

Full Tensor Gradient Data

Bell Geospace's Full Tensor Gradient system measures small variations in the 3D gravity field. For the nine tensor components, five independent components are processed in the gradiometer system. The sixth component is computed from two of the others using LaPlace's equation, while the other three tensor components can be determined using tensor symmetry. The FTG data offer higher resolution and greater fidelity compared to conventional marine gravity data. FTG data contribute to a detailed picture of the edges, shapes, and approximate depth to dominate mass anomalies shallower than 18,000 ft. Traditional gravity data is also acquired and utilized in our FTG projects to model deeper density sources.

Methodology

In order to produce timely, superior depth images for our deepwater sub-salt targets, our workflow has multiple stages and involves interaction between the seismic interpreter, potential fields interpreter, and seismic processor. In the deepwater Gulf of Mexico, gravity anomalies are generated from many different geologic sources at a variety of depths, with overlapping wavelengths. Constrained modeling is the most effective way to isolate the density sources and to focus on anomalies critical to salt imaging. We use available well control, 3-D and 2-D seismic derived surfaces, seismic velocities, and regional gravity and magnetic data to construct a complex, constrained, 3-dimensional target-oriented geologic model, which is modified at each stage during PrSDM. Forward Free-Air gravity and FTG components are calculated from the model and then subtracted from the observed data. The resulting residual anomalies indicate where mass needs to be increased or decreased within the density model. Horizons from inverse and forward gravity / gradient modeling are fed back to the seismic interpreter to produce a more accurate velocity model for the next iteration of the workflow.

We begin with a comprehensive understanding of the regional gravity field. Through 2D and 3D modeling, we account for the gravity anomalies generated by the Moho, the boundary between lower and upper crust, basement structure and lithology, and autochthonous salt. The basement model is constrained by high-resolution magnetic data and detailed profile analyses of these data. Additionally, regional seismic horizons constrain broad gravity anomalies generated by the Cretaceous and shallower section.

The target-oriented models start with key horizons interpreted from post-stack depth migrated data and a density-depth function from the nearest well is used for the sediments above allochthonous salt. Major differences between the model and the observed gravity data are analyzed with both forward and inverse modeling of gravity and computed gravity gradients. Once a PrSDM velocity model is built for imaging the top of allochthonous salt, the sediment velocity volume is converted to densities. This density volume is incorporated into the model and the gravity data are used to help define the top of salt where PrSDM has failed to image the reflector. At this stage, we often incorporate FTG data in order to resolve residual gravity anomalies generated by errors in the top of salt and sediment model. Once the top of salt surface is constrained, the velocity model is flooded with salt velocities below for imaging the base of allochthonous salt. The seismic interpreter picks areas of high confidence for the base of salt, while the gravity and FTG data are used to help interpret base of salt where depth migration (salt flood stage) has failed to image a reflector. This

integrated surface is then used to re-build and constrain a new velocity model for the sub-salt sediment velocity flood.

Case Studies

Our case studies in the Keathley Canyon and Walker Ridge OCS areas demonstrate significant contributions of FTG data to PrSDM. These examples include identification of recumbent salt overhangs and steeply dipping salt/sediment interfaces, definition of lateral contacts between salt and a high velocity shale mass, and improved imaging of top and base salt reflectors that confirm the original FTG interpretations. Many of these model improvements would not have been defined without the superior resolution of FTG data. However, high quality regional gravity and magnetic data are essential in order to reduce ambiguity in the complex 3-D geologic model.

Our method has been applied to a number of areas, and is now routinely used for PrSDM projects in the deepwater GOM. The results vary from producing major changes in the velocity model to confirmation of the original seismic interpretation with an independent data set. We have plans to apply this iterative methodology to overseas depth imaging problems, even when FTG data is not yet available. The methodology would be uniquely suited to offshore Brazil, where salt features contribute to similar imaging problems.

Conclusions

The following factors have contributed to the quality, cost effectiveness and timeliness of our successful integration of FTG data into the PrSDM process:

- Regional 2D gravity data and seismic horizons are used to build and constrain the density model beyond the target volume, rather than mathematically filtering the gravity data. Aeromagnetics is used as an additional constraint for the regional.

- We invest additional time and expense to build an FTG-constrained, detailed, sediment velocity/density cube only when earlier models are deemed inadequate, and only after the longer-wavelength anomalies in the 2D gravity data have been honored.

- Multiple iterations of the 3D density model over the target area provide “fit for purpose” models at each stage of the velocity model building process. This enables the FTG data to have a direct impact on the quality and the cycle time of the velocity modeling, thus supporting superior depth imaging.

Efficient Kirchhoff migration in the presence of strong anisotropy

Garabito[*]*,G.,UFPA, german@ufpa.br;*
Costa, J.C., UFPA, jesse@ufpa.br;
Cruz, J.C.,UFPA, jcarlos@ufpa.br
Araújo, M.S.B, UFPA, silvino@ufpa.br.

Abstract

A Fast marching eikonal solver for the exact dispersion relation in anisotropic media allowed us to implement efficiently Kirchhoff migration in the presence of strong anisotropy in 2-D. There is no restriction relative to the symmetry class except that we assume the propagation in a plane of symmetry. The principal axis of anisotropy can have arbitrary orientation relative to the coordinate system. The algorithm is applied to zero-offset synthetic data generated with elastic anisotropic finite difference code. The effect of anisotropy on the migrated section is evaluated by migrating the same data set with an elliptical anisotropic model and an isotropic model.

Introduction

The need of anisotropic models for better seismic imaging is a reality today (Gray et al., 2001). Migration in the presence of anisotropy has been implemented using several approaches in the recent literature. Dong & McMecham(1993) proposed a 3-D reverse-time migration for elliptically anisotropic velocity models with the restriction that the principal axis of the ellipsoid be oriented along the coordinate axes. Phadke et al (1994) proposed a 2-D downward continuation extrapolator for elliptical media also. Ball (1995) performed a prestack migration of a real data set using Kirchhoff migration assuming weak transversally isotropic (TI) models. Alkhalifah (1995) presented a Gaussian beam algorithm for TI media.
We developed a fast marching (Sethian, 1999) eikonal solver for the exact dispersion relation in anisotropic media in 2-D. The efficiency of the algorithm is used to compute diffraction stack curves for Kirchhoff migration. A fully elastic and anisotropic synthetic data set generated using finite differences is used to evaluate our implementation. In order to evaluate the anisotropic velocity, the synthetic data is also migrated with an elliptically anisotropic model and an isotropic model. The distortions of the migrated images are more dramatic when the principal axis of anisotropy is not aligned with the coordinate axes. In this case reflectors are mispositioned vertically and laterally. The elliptical model, though producing a better image than isotropic velocity model cannot correct these defects when the anisotropy is strong.

Anisotropic Eikonal Solver

We implemented a fast marching eikonal solver for the exact dispersion relation in 2-D, i.e., assuming that the propagation occurs in a symmetry plane. The dispersion relation in this case is

$$F(\mathbf{s}) = (\Gamma_{11} - 1)(\Gamma_{33} - 1) - \Gamma_{13}^2 = 0, \quad (1)$$

where

$$\Gamma_{11} = a_{11}s_1^2 + a_{55}s_3^2 + 2a_{15}s_1s_3 \ ,$$

$$\Gamma_{33} = a_{55}s_1^2 + a_{33}s_3^2 + 2a_{35}s_1s_3 \ ,$$

$$\Gamma_{13} = a_{15}s_1^2 + a_{35}s_3^2 + (a_{13} + a_{55})s_1s_3 \ ,$$

Γ_{ij} are the entries of the Christoffel matrix, a_{IJ} are the density normalized elastic constants in reduced notation and s_i are the slowness components (Musgrave, 1970).
The fast marching scheme (Sethian, 1999) warranties the unconditional stability and causality of the algorithm for arbitrary velocity contrasts. A binary heap keeps a computational front, the point with the minimum travel time on the computational front is select to advance the wavefront using the exact dispersion relation to compute diffractions, head waves and plane wave events and chooses the fastest. Newton-Raphson (Iserles, 1996) iterations are used to solve the dispersion relation (1) starting from elliptical anisotropy approximation.

The model and synthetic data

The model we use to present the eikonal solver and the Kirchhoff migration is presented in Figure 1, which also shows the traveltime contours for a source located in the anisotropic layer. The density in kg/m^3 units and the elastic parameters in GP of each layer are in Table 2.

Table I. Density and Elastic parameters of the Model

Layer	1	2	3	4
Dens	2300	2420	2500	2200
$\mathbf{C_{11}}$	14.375	29.163	30.625	36.000
$\mathbf{C_{13}}$	4.792	12.754	10.208	12.000
$\mathbf{C_{15}}$	0.000	-4.905	0.000	0.000
$\mathbf{C_{33}}$	14.375	22.418	30.625	36.000
$\mathbf{C_{35}}$	0.000	-0.936	0.000	0.000
$\mathbf{C_{55}}$	4.792	8.809	10.208	12.000

The layer 2 only is anisotropic and has parameters close to the Mesaverde Shale presented in Thom-

Thomsen(1986). Its Thomsen parameters for the untilted model are $\varepsilon = 0.36$, $\delta = -0.10$ and $\gamma = 0.480$.
The synthetic data set was computed using a fully elastic finite difference code. The zero-offset section presented in Figure 3 was generated using the exploding reflector model and a volume injection source was used to minimize S waves. The source signature is a Blackman-Harris with dominant frequency of 50Hz. The grid spacing is 2m and absorbing boundaries were applied at the lateral boundaries only.

Kirchhoff Migration

We used the stacking integral presented by Schleicher at al. (1993) with unit weight function. The migration integral in this case is

$$V(M) = \int_{\Omega} d\xi \partial_{-t}^{1/2} u_z(\xi, t)\Big|_{t=\tau_D(\xi,M)}, \quad (2)$$

where Ω is the sources and receivers domain which is parameterized by ξ, M is a point in the migration domain and $\partial_{-t}^{1/2}$ indicates the anticausal half derivative, $u_z(\xi,t)$ is the recorded vertical component of the displacement field, $\tau_D(\xi,M)$ is the diffraction stack curve computed using the eikonal solver and $V(M)$ represents the depth migrated image at M.

Three velocity models were used for migration. The only difference in these models is the qP-slowness curve for layer 2; the other layers have the same elastic parameters used to produce the synthetic data set. The first velocity model uses the exact anisotropic constants. The second model uses an elliptical approximation and the third model is isotropic. The P-slowness curves for layer 2 for each of these models are in Figure 2. The migration with the exact anisotropic model was four times slower than the migration using the isotropic model. The migrated images are presented in Figures 4. The results show mispositioned reflectors below the anisotropic layer when anisotropy was not correctly taken into account as we can see mainly at locations A, B and C in figure 4. Elliptical approximation produced better results the isotropic model but still was not enough to correctly delineate the reflector below the anisotropic region.

Conclusion

We implemented Kirchhoff depth migration using an efficient exact eikonal solver in anisotropic media. Application of the algorithm to synthetic data shows that, in the presence of strong anisotropy, isotropic migration performs poorly producing strong distortion of reflectors below the anisotropic layer. Elliptic approximation though producing better results than an isotropic model is not enough to produce accurate images.

References

Alkhalifah, T., 1995, Gaussian beam depth migration for anisotropic media. Geophysics, 60(5),1474-1484.

Ball, G., 1995, Estimation of anisotropy and anisotropic 3-D prestack depth migration, offshore Zaire. Geophysics, 60(5), 1495-1513.

Dong, Z. and McMechan, G.A., 1993, 3-D prestack migration in anisotropic media. Geophysics, 58, 79-90.

Iserles, A., 1996, A first course in numerical analysis of differential equation. Cambridge University Press. Cambridge

Musgrave, M.P.J., 1970, Cristal acoustics. Holden-Day. S. Francisco.

Phadke,S. Kapotas, S., Dai,N. and Kanasewich, E.R., 1994, Migration of P-wave reflection data in transversaly isotropic media.

Sethian, J.A., 1999. Level set methods and fast marching methods. Cambridge University Press. Cambridge.

Thomsen, L., 1986, Weak elastic anisotropy. Geophysics,51,1954-1966.

Acknowledgments

The authors acknowledge the support of the ANP and the PRONEX/UNICAMP in reservoir engineering for providing the computational resources.

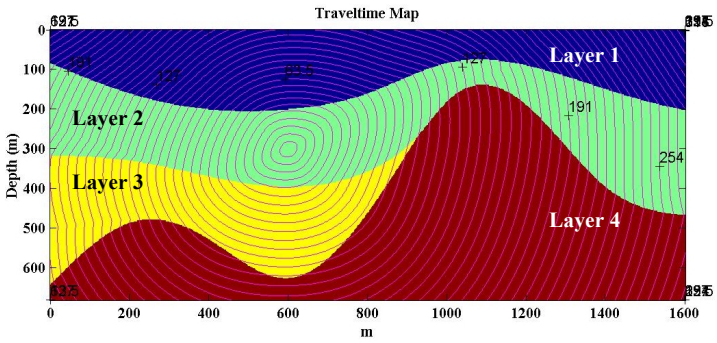

Figure 1. Layered model used for generate the synthetic data. Only the layer 2 is anisotropic. The traveltime curves are computed using the anisotropic eikonal solver.

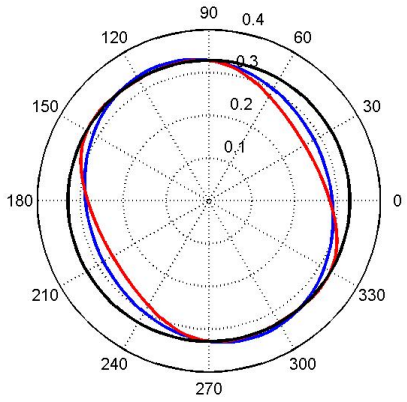

Figure 2. P-Slowness for the layer 2 used for migration. The red curve is the exact qP slowness curve for layer 2. The blue curve is the elliptical approximation and the black curve is the isotropic approximation used for migration. The slowness values are in s/km.

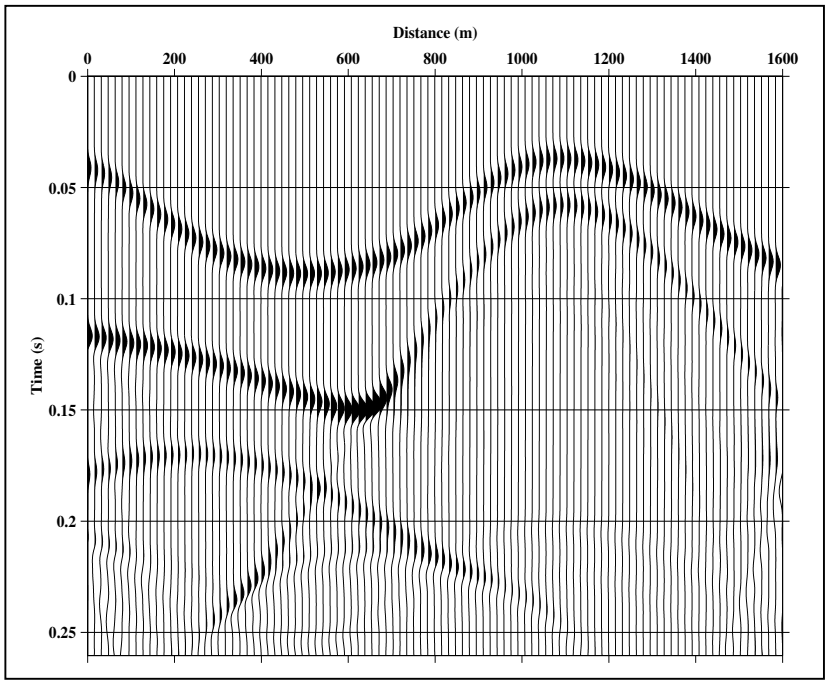

Figure 3. Zero Offset section generated by finite differences using the exploding reflector model. Volume injection sources were used to minimize S-waves.

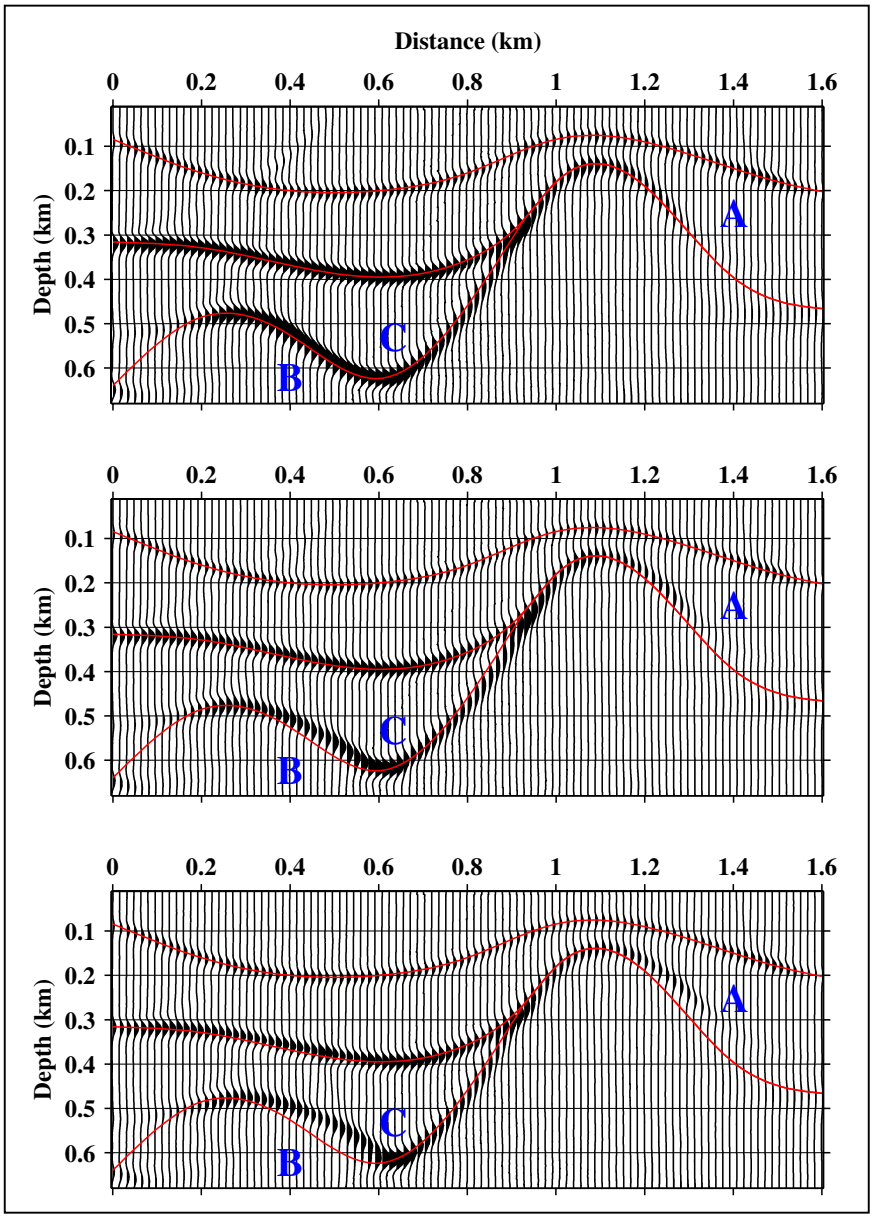

Figure 4. Kirchhoff migration results for the three velocity models. On top the migration using the exact anisotropic model. In the middle the migration result using elliptic approximation on the anisotropic layer. On bottom is the migration using the isotropic approximation indicated on figure 2. The solid line indicates the correct reflectors position. The locations A, B and C indicate differences on the migrated images.

Layered velocity model from kinematic attributes

R. Biloti, L. T. Santos and M. Tygel

State University of Campinas, Brazil

Abstract

In conventional processing, the classical algorithm of Hubral and Krey is routinely applied to extract an initial macro-velocity model that consists of a stack of homogeneous layers bounded by curved interfaces. Input for the algorithm are identified primary reflections together with NMO velocities derived from a previous velocity analysis conducted on CMP data. This work presents a modified version of the Hubral and Krey algorithm that is adapted to advantageously use previously obtained CRS attributes as its input. A simple synthetic example is provided to illustrate and explain the implementation of the method.

Introduction

The CRS method (Birgin *et al.*, 1999) is a recent technique that is becoming an alternative to the conventional seismic process, presenting promising results concerning the generation of simulated zero-offset sections. The CRS parameters give, in addition to a better stacking, more information, which can be applied to produce a more reliable velocity model that can be used for further imaging purposes such as depth migration.

This is what our work intends to do: once we have already made an effort to estimate the CRS parameters to construct a clean simulated zero-offset section, we shall immediately be in the position of inverting a macro-velocity model.

Hyperbolic Traveltime and CRS parameters. The hyperbolic traveltime expression relates the traveltime of two rays. One of them is taken as a reference ray and is called central ray. When this central ray is taken as a normal ray at X_0 (see Figure 1), the formula becomes

$$T^2(x_m,h) = \left(t_0 + \frac{2x_m \sin\beta_0}{v_0}\right)^2 + \frac{2t_0\cos^2\beta_0}{v_0}\left(K_N\, x_m^2 + K_{NIP}\, h^2\right),$$

with $x_m = (x_G + x_S)/2 - x_0$ and $h = (x_G - x_S)/2$, where x_0 is the coordinate of the central point, x_S and x_G are the horizontal coordinates of the source and receiver pair (S,G) near X_0, t_0 is the zero-offset traveltime and β_0 is the angle of emergence at the zero-offset ray with respect to the surface normal at the central point X_0. The quantities K_N and K_{NIP} are the wavefront curvatures of the N-wave and the NIP-wave (Tygel *et al.*, 1997), respectively, measured at the central point X_0. The traveltime formula above is on the kernel of the CRS method. Therefore, those three parameters, β_0, K_N and K_{NIP} are called CRS parameters.

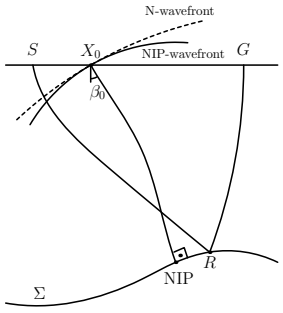

Figure 1: CRS Parameters for a normal central ray X_0 NIP X_0: the emergence angle β_0 and the NIP- and N-wavefront curvatures. Σ is the reflector, X_0 is the central point coordinate, and S and G are the source and receiver positions for a paraxial ray, reflecting at R.

The Hubral & Krey algorithm

Our inversion method is based on the well established algorithm proposed in Hubral and Krey (1980). The velocity model to be inverted from the data is assumed to consist of a stack of homogeneous layers bounded by smoothly curved interfaces. The unknowns are the velocity in each layer and the shape of each interface. These unknowns are iteratively obtained from top to bottom by means of a layer-stripping process.

The main idea of the algorithm is to backpropagate the NIP-wave down to the NIP located at the bottom interface of the layer to be determined (see Figure 2). This means that the velocities and the reflectors above the layer under consideration have already been determined. Since the NIP-wave is due to a point source at the NIP, the backpropa-

gation through this last layer gives us a focusing condition for the unknown layer velocity.

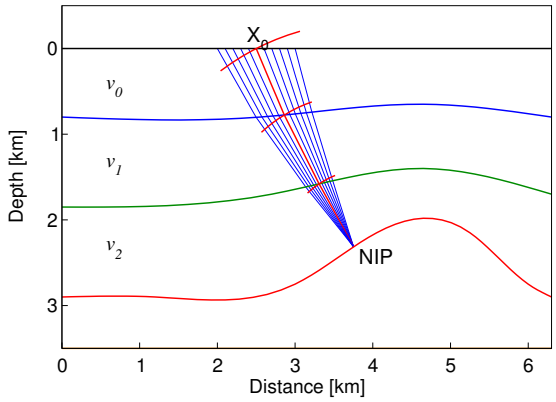

Figure 2: NIP-wavefront associated to the central zero-offset ray X_0 NIP X_0, in red.

To well describe the wavefront curvature along a ray path that propagates through the layered medium, we should consider two distinct situations: (a) propagation inside a homogeneous layer and (b) transmission across an interface. Figure 3 depicts a

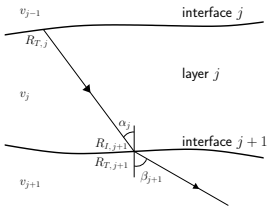

Figure 3: Ray propagation through layer j.

ray that traverses the homogeneous j-th layer (with velocity v_j) being transmitted at the interface $j+1$. Let $R_{T,j}$ be the wavefront radius of curvature at the initial point of the ray (that is, just below the j-th interface). The wavefront radius of curvature, $R_{I,j+1}$, just before transmission, is given by

$$R_{I,j+1} = R_{T,j} + v_j\,\Delta t_j\ , \tag{1}$$

where Δt_j is the traveltime of the ray inside the layer. We now consider the change in wavefront curvature due to transmission at the interface. As shown in Hubral and Krey (1980), we have

$$\frac{1}{R_{T,j+1}} = \frac{v_{j+1}\cos^2\alpha_j}{v_j\cos^2\beta_{j+1}}\frac{1}{R_{I,\,j+1}} + \frac{1}{\cos^2\beta_{j+1}}\left(\frac{v_{j+1}}{v_j}\cos\alpha_j - \cos\beta_{j+1}\right)\frac{1}{R_{F,\,j+1}}\ . \tag{2}$$

Here, α_j and β_{j+1} are the incident and transmission angles of the ray, respectively, and $R_{F,j}$ is the interface radius of curvature, all these quantities being measured at the transmission point. Note that Snell's law is valid and relates α_j and β_{j+1}. Assume now that the NIP is located at the $(N+1)$-th interface. This leads to the *focusing conditions*

$$\begin{cases} R_{I,N+1} &= 0 = R_{T,N} + v_N\Delta t_N \\ \Delta t_N &= t_0 - \left(\displaystyle\sum_{j=1}^{N-1}\Delta t_j\right) \end{cases} \tag{3}$$

which determine the velocity v_N. Note that $R_{T,N}$, as given by setting $j = N-1$ in equation (2), has an implicit dependence on v_N and β_N. This is because $v_N \sin\beta_N = \sin\alpha_{N-1}\ v_{N-1}$, by Snell's law. Once v_N and β_N are determined, the segment of the zero-offset ray inside the N-th layer can be constructed. The sought-for NIP location is then such that its distance to that transmission point is $v_N\Delta t_N$.

Summary of the algorithm

It is instructive to discuss the key ideas involved in the preceding strategy. Firstly, we will present the main steps of the algorithm. Then, we will make some comments about its implementation.

The method aims to extract a model composed by homogeneous layers separated by smoothly curved reflectors, corresponding to the well identified interfaces within the data only. This choice is made *a priori* by the user.

Determination of the first layer. The input data is, for each zero-offset ray, the traveltime, the emergence angle and the NIP-wavefront curvature. The velocity of the first layer is assumed to be known. Thus, only the reflector (the bottom of the layer) should be determined. As explained below, this can be achieved in many different ways.

Determination of the jth-layer. Suppose that the model has been already determined up to the $(j-1)$th-layer. The method will proceed to the determination of the next layer, that is, the velocity of the jth-layer and the $(j+1)$th-interface. The input data is again, for each zero offset ray reflecting at the interface $(j+1)$, the traveltime, the emergence angle and the NIP-wavefront curvature. Trace the zero-offset ray down to the j-th interface. Recall that this ray makes the angle β_0 with the surface normal at its initial point. Now, using equations (1) and (2), back-propagate the NIP-wave from the

surface to the j-th interface along that ray. Then, use the focusing conditions (3) to determine the layer velocity v_j, the angle β_j and the NIP.

The above procedure can, in principle, be done to each zero-offset ray. However, under the constraint that the layer velocity v_j is constant, we obtain an over-determined system for that unknown. How to deal with problem will be discussed below.

Brief discussion of the algorithm

The quantities needed by the method (emergence angles, normal traveltimes and NIP-wave curvature) are not directly available, but have to be extracted from the data. In Hubral and Krey (1980), those quantities are obtained by conventional processing on CMP data.

The back-propagation of the NIP-wavefront, is carried out independently for each ray. Thus, in principle, each ray carries enough information to recover the layer velocity, that can be translated into many equations depending on the same unknown. This implies an over-determination of the velocity. Hubral and Krey have pointed out that this "excess" of information could be used to improve the velocity distribution considered.

Equation (2) depends on the curvatures of the interface (R_F) at the transmission point. Hubral and Krey state that this can be obtained by a normal ray migration.

The revised algorithm

In this section we discuss how to use the CRS parameters to fully supply the needs of the Hubral and Krey algorithm, and how to deal with the numerical aspects involved in. Then, we present a revised version of the original algorithm.

The obvious advantage of having the CRS parameters is that emergence angles and NIP-wavefront curvatures have been already determined. Thus, nor a velocity analysis neither a traveltime gradient estimation are required. Moreover, using the well-defined coherence section provided by the CRS method, it becomes easier to select the interesting horizon events.

We have to take special care when dealing with estimated quantities as input data, due to estimation errors. The strategy applied was to smooth the parameter curves. This has a physical meaning, since no abrupt variations on the parameters can in general occur. The method used can be stated as: To each five neighboring points on the curve, fits the least-square parabola and replace the middle point by its correspondent on the parabola. This smoothing technique can be applied a fixed number of times to each parameter curve. This method can be applied to any curve on the plane. All we need to know is how to follow the curve. In our case, the curves are parameterized by the central point coordinate. In caustic regions, many values of the parameter are associated to the same central point. This could generate a problem to find out the correct sequence[1].

We have formulated a criterion to unfold the parameter curve. When the curve has more than one value for the same central point coordinate, the proposed criterion tries to keep the variations of the CRS parameters between two neighboring points on the curve as small as possible. The merit function to be minimized is

$$F(\mathbf{p}_j, \mathbf{p}_i) = \frac{|t_0^j - t_0^i|}{t_0^i} + \frac{|\beta_0^j - \beta_0^i|}{|\beta_0^i|} \,,$$

where $\mathbf{p}_i = (x_0^i, t_0^i, \beta_0^i, K_{NIP}^i, K_N^i)$ denotes the vector of the CRS parameters, i is the index of the current point and j varies on the set of index of the neighboring point of the current point. We evaluate the function above for each neighbor of point x_0^i and then the point with minimum value is select to be next one in the reordered sequence. We have made tests including two more terms, one for K_{NIP} and one for K_N, but the stability of the method was reduced. Recall that this criterion should be applied before the smoothing process. So it must work even if there is noise in the parameters values. We have made several tests with this criterion and it was really able to unfold the curve.

We deal with the over-determination on the velocity considering a solution in the least-squares sense. By now, we are supposing a model with homogeneous layers, but this approach can be easily extended to incorporate velocity profiles depending, for example, linearly on the depth.

The many obtained NIP's could be interpolated to recover the interface, but this lead to a not so smooth interface. This would be a disaster for ray tracing processes. Better than simply smoothing the interpolated NIP's, we use them to adjust a cubic spline in a least-squares sense. This is performed by means of an optimization algorithm, which really enhances the quality process overall.

Following, we present our implementation of

[1]The reader could argue that perhaps the correct order are already known. But, since the CRS parameters are extracted from the parameter sections by some picking process, the method we are going to describe could be used to automatically do it.

Migração em Profundidade Usando a Solução Numérica da Equação do Eiconal

Luz, S.L.F, *slfl@ufpa.br*, Cruz, J.C.R, *jcarlos@ufpa.br*, Garabito, G., *german@ufpa.br*
Universidade Federal do Pará

Abstract
The Kirchhoff migration method is very useful for determining the position of seismic reflectors, if it is known the seismic wave velocity model and the traveltimes through the earth model. The traveltime calculation is a necessary step for stacking the seismic data by means of the Kirchhoff migration operator. In this work the traveltimes are obtained by solving the eiconal equation of the ray theory. A developed migration algorithm is applied to synthetic models, providing a very good image resolution even in the presence of random noise and reflectors below dome-like strucrures.

Introdução
Com a finalidade de obter mais informações sobre as propriedades físicas da subsuperfície da terra, vários autores têm desenvolvido algoritmos de modelamento e imageamento sísmicos e aplicado em métodos de migração Kirchhoff em profundidade. Estes métodos requerem o cálculo dos tempos de trânsito entre as posições de registro na superfície e os pontos em profundidade no modelo de velocidade. Atualmente, há dois métodos para o cálculo dos tempos de trânsito: o primeiro, o mais usual, emprega o traçado de raios (Cerveny et al., 1977) o segundo, resolve a equação do eiconal através de um esquema numérico, uma técnica recentemente desenvolvida por vários autores como Reshef & Kosloff, 1986; Vidale, 1988; Podvin & Lecomte, 1991; Schneider et al., 1992; Zhao, 1998. Este trabalho se propõem a desenvolver um algoritmo de migração Kirchhoff em profundidade utilizando os tempos de trânsito a partir da solução da equação eiconal. Este esquema calcula somente os eventos das primeiras chegadas. Serão analisados os efeitos do ruído na seção sísmica migrada e a presença de refletores abaixo de um domo. Diante destas situações veremos como se comporta o algoritmo desenvolvido, mostrando sua estabilidade e acurácia na reconstrução da imagem do refletor.

Integral de Empilhamento de Difração
Considera-se que a subsuperfície é descrita por um modelo de camadas isotrópicas estratificadas, e que também existem somente reflexões primárias P-P com pares fonte-receptor (S,G) dados por

$$x_S = x_S(\xi), \quad x_G = x_G(\xi) \ , \qquad (1)$$

em que ξ é um parâmetro na superfície que identifica a posição de um par fonte-receptor. De acordo com Schleicher et al. (1993) e seguindo o formalismo dado por Urban (1999), a integral de empilhamento de difração bidimensional pode ser escrita como

$$V(M,t) = \frac{1}{\sqrt{2\pi}} \int_A d\xi \, w(\xi,M) \, \partial_{t_-}^{\frac{1}{2}} U(\xi, t+\tau_D(\xi,M)). \qquad (2)$$

Na equação (2), $\partial_{t_-}^{\frac{1}{2}}$ é o operador semi-derivada temporal anti-causal e corresponde, no domínio da freqüência, ao filtro $F(\omega)=\sqrt{-i\omega}$. τ_D é a curva de tempos de trânsito de difração calculada para cada ponto *M* da malha na zona alvo de migração, ou seja, o tempo de trânsito correspondente ao raio que liga a fonte ao ponto *M* mais o tempo de trânsito dos raios ligando o ponto *M* a cada um dos geofones. A função $U(\xi, t + \tau_D(\xi,M))$ representa a componente principal do campo de onda da onda primária refletida e $w(\xi,M)$ a função peso. Tendo em vista que este trabalho não se propõe a remover o efeito causado pelo espalhamento geométrico no sinal sísmico, a função peso assumirá o valor um. O resultado, portanto, da integral (2) fornece apenas uma imagem cinemática do refletor sísmico. Neste trabalho é considerada apenas a velocidade da onda P.

Equação da Eiconal
Considerando-se a solução assintótica da teoria do raio (Cerveny, 1987), a propagação cinemática da onda é descrita pela equação

$$\nabla\tau \cdot \nabla\tau = s^2, \qquad (3)$$

conhecida como equação do eiconal, em que s(**x**) é a vagarosidade do meio (inverso da velocidade da onda) e τ (**x**) representa o tempo de trânsito de uma frente de onda num ponto **x** em profundidade. Vários autores têm recentemente desenvolvido métodos para calcular os tempos de trânsito diretamente sobre uma malha regular. Neste trabalho utilizou-se um programa desenvolvido por ZHAO (1998) , que resolve a equação do eiconal. Este programa se baseia na consideração de frentes de ondas curvas, sendo portanto garantida a acurácia do cálculo dos tempos e tendo como referências principais os trabalhos de Schneider et al. (1992) e Podvin & Lecomte (1991). Este programa fornece somente os tempos de trânsito das primeiras chegadas, usados para ser aplicado no algoritmo de migração desenvolvido e obter uma imagem do refletor, haja visto que os modelos físicos considerados neste trabalho não possuem fortes variações laterais de velocidade.

Modelos Geofísicos

Os modelos usados são bidimensionais, com uma rede que apresenta um espaçamento regular $\Delta x = \Delta z = 3m$, satisfazendo a seguinte relação

$$\frac{v}{16f} \leq \Delta z \leq \frac{v}{2f} , \qquad (4)$$

onde v é a menor velocidade do meio, f a freqüência do pulso fonte e Δz o intervalo de discretização da rede. A relação acima é importante para estimar o valor do tamanho de cada cela Δz do grid, que deve ser menor do que o comprimento de onda $\lambda = v/2f$, para se ter uma melhor precisão no cálculo dos tempos de trânsito. As curvas coloridas, nos modelos, representam frentes de onda e mostram como a energia se propaga no meio, Figuras 1 e 4. O meio é heterogêneo e isotrópico. O primeiro modelo, Figura 1, é constituído por 4 interfaces, sendo as três primeiras, interfaces suavemente curvas abaixo das quais encontra-se um domo salino. As velocidades na primeira, segunda, terceira e quarta camadas são 2.5 km/s, 3.0 km/s, 3.5km/s e 4.0 km/s respectivamente. O segundo modelo foi construído a partir do primeiro, adicionando-se um refletor abaixo do domo. A velocidade abaixo do domo é 4,5 km/s, Figura 4.

Geração de Dados Sintéticos

Os dados sintéticos foram gerados a partir do programa SEIS88 (Cerveny & Psencik, 1988). Estes dados usados para a migração são sismogramas contendo a componente vertical do vetor deslocamento sísmico, sendo desprezado o efeito da superfície da terra, ou seja, a camada superior do modelo é considerada um semi espaço infinito. Para a geração do sismograma sintético temos a seguinte descrição para os dois modelos: a configuração utilizada foi de afastamento comum, com um afastamento de 50m. O número de pares de fonte e geofone é 83, e as posições iniciais da primeira fonte e do primeiro geofone são respectivamente 0.2km e 0.25km, sendo o espaçamento entre cada fonte ou geofone igual a 0.025km. O pulso fonte utilizado foi a função Gabor, com freqüência dominante de 30 Hz, sendo o intervalo de amostragem entre cada traço de 0.002s. A zona alvo (retângulos indicados por linhas pontilhadas) possui dimensões $0.3 \leq x \leq 2.2$ km, $0.4 \leq z \leq 1.4$ km, e o intervalo de discretização é $\Delta x = 0.025$ km e $\Delta z = 0.0083$ km. Foi adicionado ruído aditivo ao sismograma do primeiro modelo com amplitude máxima de 20% da amplitude máxima do dado sintético. As Figuras 2 e 5 mostram os sismogramas gerados para o primeiro e segundo modelos, respectivamente.

Resultados Numéricos

Os dados sintéticos foram migrados no domínio da profundidade, Figuras 3 e 6. No primeiro exemplo o objetivo foi ver o desempenho do algoritmo, aplicado a um dado sintético com ruído. No segundo exemplo, visou-se imagear um refletor localizado abaixo de um domo, uma situação muito explorada ultimamente, como por exemplo, na investigação de reservatórios que se encontram abaixo de um domo. Foi considerado conhecido a priori o modelo de velocidade verdadeiro acima do refletor alvo.

Conclusões

Através dos resultados obtidos pôde-se notar a eficiência e acurácia do algoritmo de migração desenvolvido, na reconstrução da imagem do refletor, quando utilizando os tempos de trânsito da equação do eiconal. Mesmo na presença de ruídos nos dados sintéticos, o algoritmo apresentou um bom desempenho, fornecendo uma boa imagem do refletor. Somente os tempos dos primeiros eventos foram utilizados, e o método utilizado para o cálculo dos tempos de trânsito mostrou-se bastante eficiente quando empregado na migração dos dados sísmicos.

Referências

Podvin, P. & Lecomte, I., 1991. Finite difference computation of traveltimes in very contrasted velocity models: a massively parallel approach and its associated tools. *Geophys. J. Int*., 105: 271-284.

Schleicher, J., Tygel, M., Hubral, P., 1993. 3-D True-amplitude finite-offset migration. *Geophysics*, 58: 1112 - 1126.

Schneider, Jr. W. A, Ranzinger, K.A., Balch, A.,H, Kruse, C.-1992. A dynamic programming approach to First Traveltime computation in media with arbitrarily distributed velocities. *Geophysics*, 57: 39-50.

Zhao, P., 1996. An efficient computer program for wavefront calculation: Computers & Geoscienses: 22: 239-251.

Urban, J., 1999. Two-dimensional true-amplitude migration and introduction to 2.5-D case. Master theses. Federal University of Pará, Brasil.

Agradecimentos

Agradecemos a Ping Zhao, do departamento de Geofísica de exploração da universidade de Curtin, autor do programa Eiconal, e a Cerveny & Psencik, 1988, autores do programa de modelamento sísmico, SEIS88. Agradecemos também à ANP pelo suporte financeiro.

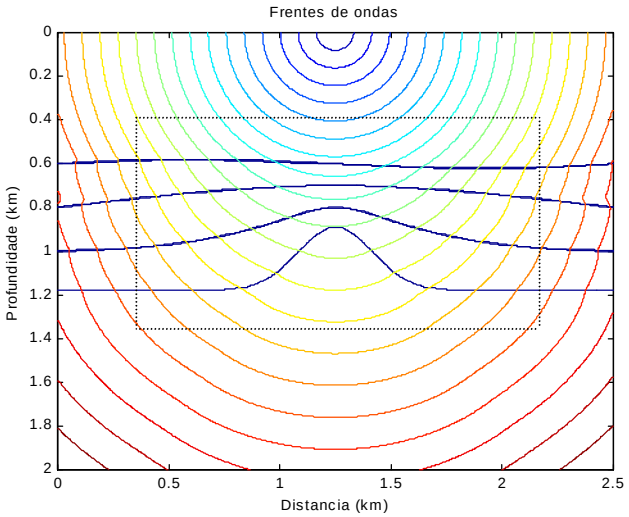

Figura 1 - Modelo complexo contendo um domo. As velocidades na primeira, segunda, terceira e quarta camadas são 2.5 km/s, 3.0 km/s, 3.5km/s e 4.0 km/s respectivamente

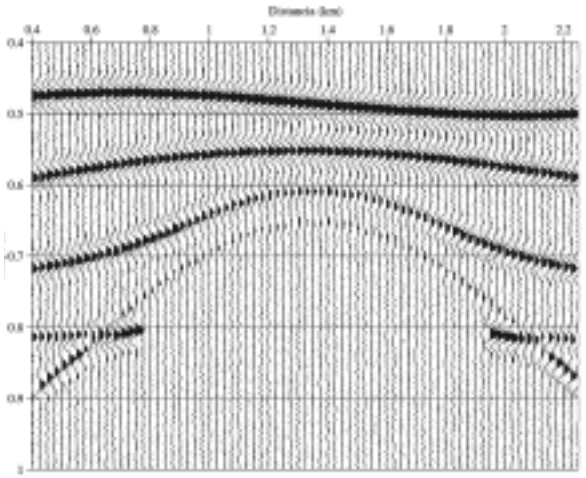

Figura 2 - Sismograma contendo ruído aditivo com amplitude máxima de 20 % da amplitude máxima do dado sintético. O pulso fonte utilizado foi a função Gabor com freqüência dominante de 30 Hz e o intervalo de amostragem entre os traços é de 2 ms.

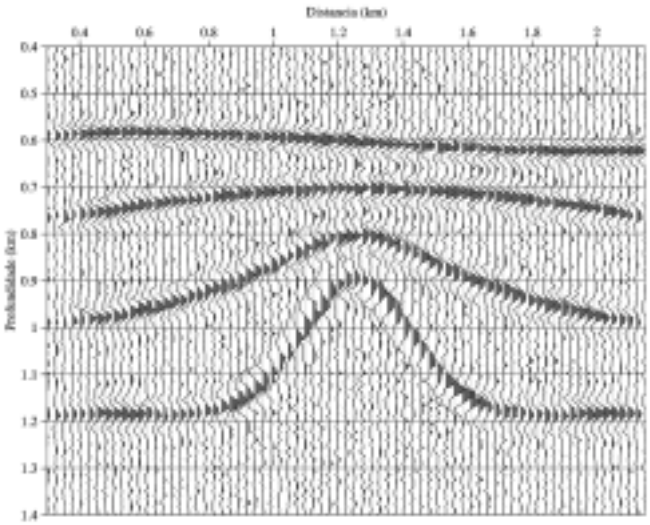

Figura 3 - Seção sísmica migrada no domínio da profundidade usando os tempos de trânsitos da equação do eiconal. Foi utilizado o modelo de velocidade verdadeiro.

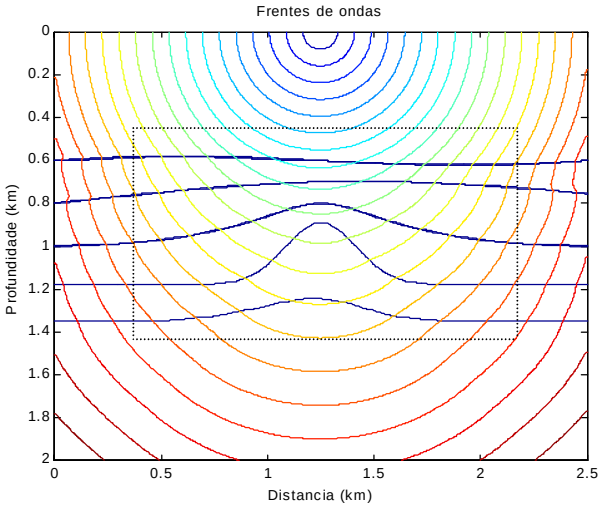

Figura 4- Modelo físico contendo um refletor alvo abaixo do domo. Foram mantidas as mesmas velocidades do modelo anterior, sendo agora a velocidade abaixo do domo igual a 4.5 km/s.

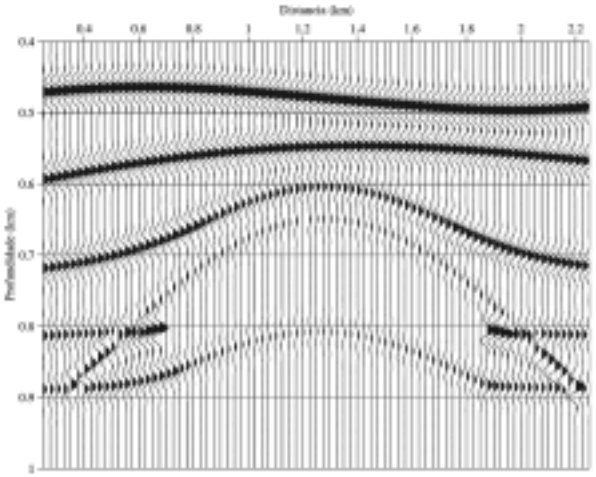

Figura 5 - Sismograma sintético.

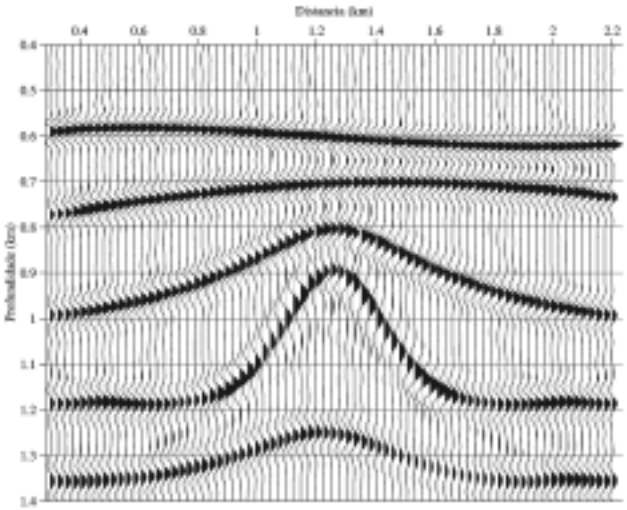

Figura 6 - Seção sísmica migrada pela equação eiconal usando o modelo de velocidade verdadeiro.

Migração pré-empilhamento em profundidade no domínio das Ondas Planas

João Roberto Simões B. dos Santos (*), Reynam da Cruz Pestana (**), & Paul L. Stoffa (***)

ABSTRACT

The prestack migration tecnique in the plane wave domain is based on the solution of acoustic wave equation. Initially the shots gathers are transformed to tau-p domain and sorted on common offset ray parameter sections. After that, these sections are transformed to frequency–source wavenumber domain (w – k_s) by the Fourier transform in order to apply the prestack migration operator. The image is obtained when all common offset ray parameter migrated sections are summed. This prestack migration method can be also used on lateral velocity medium as long as a split-step phase correction is applied. It was tested on synthetic data and we obtained reasonable results even on the SEG/EAGE salt model.

INTRODUÇÃO

A migração pré-empilhamento de seções de parâmetro de raios constante baseia-se na solução da equação acústica da onda (Pestana et al., 2001). A imagem em profundidade é construída pela combinação dos componentes de ondas planas que se propagam a partir das posições das fontes com o campo de ondas planas decorrente da depropagação das ondas registradas nos receptores. A decomposição prévia do campo de ondas em componentes de ondas planas é obtida a partir dos dados registrados em tiro comum transformados para o domínio *tau-p* (tempo de interseção – parâmetro de raio) e agrupados em seções de parâmetro de raio constante. Como a operação de migração é realizada no domínio da freqüência e do número de onda (w – k_s), uma transformada dupla de Fourier ainda deve ser aplicada sobre as seções de p comum. O operador de extrapolação 1-D desta migração guarda semelhança com o operador DSR de migração pré-empilhamento do tipo "phase-shift" de Yilmaz (1980). Nesta migração a construção da imagem final em profundidade é obtida pela simples soma das seções de p comum migradas separadamente, ou seja, pela superposição de pontos de imagem comum ("common image gathers") de todas as seções de mesmo parâmetro de raio. No caso de meios com variação lateral de velocidade, implementamos uma correção de fase tipo "split-step" (Stoffa et al., 1990), apenas sobres as posições das fontes, a cada passo de profundidade Δz, visando corrigir as variações laterais de velocidade.

TEORIA ENVOLVIDA

A equação acústica 2-D da onda, em um meio de densidade constante, para fonte e receptores, pode ser expressa por:

$$\left[\frac{\partial^2}{\partial z^2}+\frac{\partial^2}{\partial x_r^2}-\frac{1}{v^2}\frac{\partial^2}{\partial t^2}\right]P(x_r,z,t)=S(x_s,z=0,t), \quad (1)$$

onde x_s corresponde a posição da fonte e x_r as posições dos receptores ao longo do levantamento, P é o campo de pressão em (x_r,z,t), devido à fonte S(x_s,z=0,t) e v=v(x,z) é a velocidade de propagação da onda compressional.

Aplicando-se uma transformada dupla de Fourier na equação (**1**), excluindo-se o termo fonte *S, e* impondo-se a condição de que a velocidade varia apenas com a profundidade (v=v(z)), chega-se a equação de Helmholtz no domínio (k_x,z,w), ou seja:

$$\frac{d^2P(z)}{dz^2}+k_z^2P(z)=0 \quad (2)$$

onde k_z é o número de onda vertical e P=$P(z)$ é o campo de pressão.

Para *v constante* dentro de cada intervalo de profundidade *Dz*, a solução da equação (2), que é de interesse para a migração, é expressa da seguinte maneira:

$$P_{(k_x,z,w)}=P_{(k_x,z=0,w)}e^{-ik_z\Delta z} \quad (3)$$

onde o número de onda vertical k_z é dado por:

$$k_z=\sqrt{\frac{w^2}{v^2(z)}-k_x^2}\ . \quad (4)$$

Na equação (**3**), o termo $e^{-ik_z\Delta z}$ corresponde ao operador de continuação descendente em profundidade, utilizado tanto na migração F-K, pós-empilhamento com velocidade constante desenvolvida por Stolt (1978), como na migração pós-empilhamento por deslocamento de fase, conhecida como "phase-shift" e descrita inicialmente por Gazdag (1978).

Dessa forma, o operador para continuação descendente das fontes é dado por:

$$e^{-ik_z^s\Delta z}\text{, onde } k_z^s=\sqrt{\frac{w^2}{v_s^2(z)}-k_s^2}\ , \quad (5)$$

e, de forma análoga, para a continuação dos receptores temos:

(*) PETROBRAS/E&P-SSE/UN-RIO/ATEX/PS, Brazil; (**) CPGG/UFBA, Brazil; (***) IG –UTEXAS, USA

$e^{-ik_z^r \Delta z}$, onde $k_z^r = \sqrt{\frac{w^2}{v_r^2(z)} - k_r^2}$. (**6**)

Combinando os operadores Eq. (**5**) e Eq. (**6**), chega-se a expressão completa para a extrapolação dos dados no domínio (k_s,k_r,w,z). Sendo assim o campo extrapolado, entre z=0 e z=Dz, é dado por:

$$P(k_s, k_r, w, \Delta z) = P(k_s, k_r, w, z=0)\, e^{-ik_z^{(s,r)}\Delta z} \quad (7)$$

com v=v_s=v_r, tem-se então que k_z, em função de (k_s,k_r,w) é dado por:

$$k_z^{(s,r)} = \sqrt{\frac{w^2}{v^2} - k_s^2} + \sqrt{\frac{w^2}{v^2} - k_r^2}\,. \quad (8)$$

A **Figura 1** descreve como esse operador faz a continuação das ondas planas provenientes das fontes (**s**), e dos receptores (**r**):

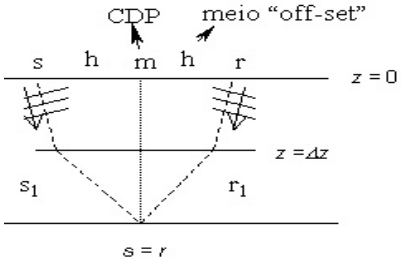

Figura 1: modelo gráfico para a continuação descendente que deve sofrer uma frente de onda plana, na fonte (***s***) e no receptor (***r***), para chegar, respectivamente, nas posições s_1 e r_1.

O operador de extrapolação $e^{-ik_z^{(s,r)}Dz}$ também pode ser obtido no domínio (k_s,p_0,z,w), depois se aplicar uma mudança de coordenadas da fonte (x_s) e receptor (x_r), para novas posições, respectivamente, de fonte equivalente (x'_s) e de afastamento (x_0). Através do princípio da invariância para os dados nos domínios transformados, tem-se a seguinte equivalência:

$$P(k_s, k_r, w) \equiv P(k_s', k_0, w) \quad (9)$$

Considerando que k_0=wp_o, então k_z no domínio (k_s,p_0,w) corresponde a:

$$k_z = \sqrt{\frac{w^2}{v^2} - (k_s - wp_0)^2} + \sqrt{\frac{w^2}{v^2} - w^2 p_0^2}\,. \quad (10)$$

A extrapolação em profundidade de cada seção de mesmo parâmetro de raio p_0, é então obtida por:

$$P(k_s, p_0, w, z=\Delta z) = P(k_s, p_0, w, z=0) e^{-ik_z \Delta z} \quad (11)$$

Finalmente, para se obter a imagem em profundidade, aplica-se uma transformada inversa de Fourier ao longo de k_s na Eq. (**11**), obtendo-se assim os dados no domínio (x_s,p_0,w,z), e em seguida impõe-se a condição de imagem (t=0 e x_0=0), o que respectivamente equivale a somar todos os componentes de freqüência que estão sendo migrados, e colocar todas as contribuições das fontes e dos receptores em uma mesma posição em profundidade (afastamento nulo), que é obtido, na prática, quando são somadas todas as seções de p-constante migradas separadamente.

EXTENSÃO PARA MEIOS COM VARIAÇÃO LATERAL DE VELOCIDADE

Essa extensão é feita através da aplicação de um termo de correção nos dados extrapolados no domínio w - x_s. Na prática, tal correção só está sendo aplicada sobre o campo de ondas relativo as posições das fontes. Nesse sentido, o processo de extrapolação de cada seção de mesmo parâmetro de raio é feito de forma similar ao da migração pós-empilhamento do tipo "split-step" (Stoffa et al., 1990). Os dados são extrapolados inicialmente no domínio (p_0,k_s,z,w), usando-se uma velocidade intervalar de referência, que normalmente é a velocidade média do intervalo em profundidade. Em seguida, com os dados já no domínio (p_0,x_s,z,w), o termo de correção de fase é aplicado com o objetivo de corrigir as variações laterais de velocidade. Para se obter esse termo de correção, calcula-se a diferença entre o número de onda vertical (k_z), computado através da vagarosidade (inverso da velocidade) verdadeira do meio, u(x,z), e do número de onda vertical obtido através da vagarosidade de referência, neste caso $\ddot{u}$(z). Sendo assim, a diferença entre o k_z verdadeiro e o calculado com a vagarosidade de referência, apenas para o termo fonte, definido aqui como *" k_z erro"*, é dado por:

$$k_z erro = \sqrt{(wu(x,z))^2 - (k_s - wp_o)^2} - \sqrt{(w\ddot{u}(z))^2 - (k_s - wp_o)^2}\,. \quad (12)$$

Desprezando-se os termos de 2ª ordem na expansão binomial dessas duas raízes quadradas e coletando apenas os termos de 1ª ordem, obtém-se:

$$k_z\ erro \approx w(u(x_s, z) - \ddot{u}(z)) \quad (13)$$

Sendo assim, a correção durante a extrapolação de cada passo de profundidade Δz, devido à variação lateral de velocidade, é feita usando o seguinte termo de correção de fase, relativo às posições das fontes:

$$e^{[-iw(u(x_S,z) - \ddot{u}(z))]\Delta z} \quad (14)$$

onde $u(x_s, z)$ e $\ddot{u}(z)$ correspondem, respectivamente, à vagarosidade verdadeira e a vagarosidade de referência.

Migração pré-empilhamento em profundidade no domínio das Ondas Planas

O termo de correção de variação lateral, referente aos afastamentos, não está sendo aplicado nesta migração, o que tornaria completa a correção da variação lateral de velocidade. Entretanto, como o termo de k_z, referente aos afastamentos, não depende de k_s, logo optamos por usar o próprio valor da vagarosidade , no seu cálculo, ou seja:

$$e^{\left[-iw\sqrt{u^2(x_S,z)-p_0^2}\right]\Delta z} \qquad (15)$$

APLICAÇÃO EM DADOS SINTÉTICOS

A presente técnica de migração foi testada sobre dois diferentes modelos geológicos de subsuperfície. Inicialmente para um modelo de camadas planas e horizontais com falhamento, depois sobre um modelo mais complicado de uma almofada de sal com diversos falhamentos (modelo SEG/EAGE).

No lado esquerdo da **Figura 4**, exibe-se o modelo geológico de camadas planas horizontais com falhamento no qual foi testada a nossa migração pré-empilhamento. A partir desta geometria foram modelados 150 registros de tiro comum, com 2s de comprimento cada, 64 canais a 0.02 km de intervalo entre estações e razão de amostragem temporal de 0,004s. No lado direito da **Figura 4** tem-se o campo de velocidade intervalar em profundidade utilizado, variando com a profundidade, segundo um gradiente vertical de $0.5s^{-1}$.

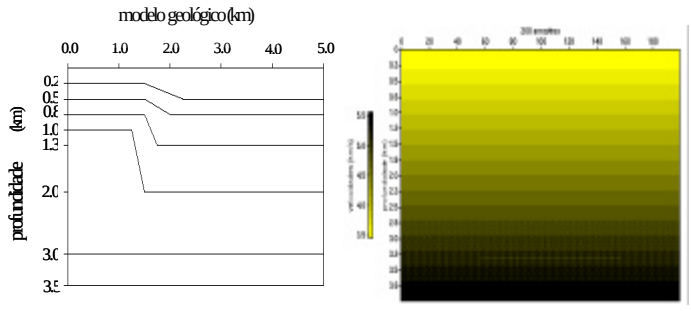

Figura 4: modelo de camadas planas e horizontais com falhamento (lado esquerdo) e o campo de velocidade intervalar utilizado (lado direito).

A **Figura 5**, ilustra a seção "near-trace", para esse modelo geológico, gerada a partir do campo de velocidade intervalar.

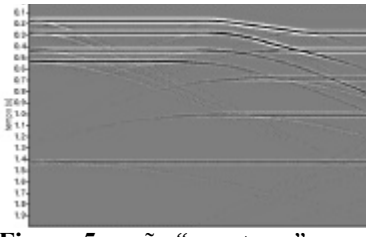

Figura 5: seção "near-trace".

Na transformação de cada registro de tiro comum para o domínio *tau-p* foram gerados 51 parâmetros de raio, de 0.0 até +0.5 s/km, com incrementos de 0.01 s/km. Na **Figura 6**, são apresentados alguns resultados desta migração em profundidade, respectivamente, para uma única seção de parâmetro de raio constante, neste caso, de p=0.0 s/km (lado esquerdo), e para 26 seções de parâmetro de raio constante, ou seja, com imagem construída pela soma de 26 seções de p-constante migradas separadamente, de p=0.0 a p=+0.25s/km (lado direito).

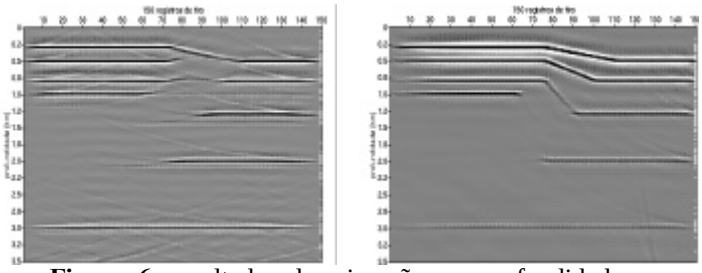

Figura 6: resultados da migração em profundidade, do modelo de camadas horizontais com falhamento.

Na **Figura 7** temos o campo de velocidade do modelo sintético SEG/EAGE, que apresenta uma almofada de sal com diversos falhamentos e variação lateral de velocidade. Os dados sísmicos referentes a este modelo correspondem a 675 registros de tiro, com 135 canais, razão de amostragem de 0,004 s e comprimento de registro de 1250 amostras. A partir desses dados foram gerados 675 registros de tiro no domínio *tau-p*, cada um com 61 parâmetros de raio, variando de +0.2 até –0.4 s/km, a –0,01 s/km de incremento.

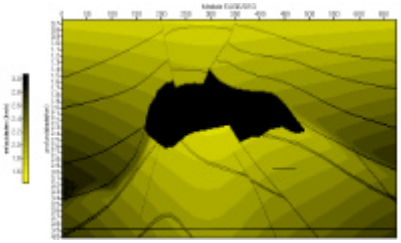

Figura 7: campo de velociadade do SEG/EAGE.

(*) PETROBRAS/E&P-SSE/UN-RIO/ATEX/PS, Brazil; (**) CPGG/UFBA, Brazil; (***) IG –UTEXAS, USA

Na **Figura 8**, são apresentados os resultados da migração em profundidade no domínio das ondas planas do modelo do SEG/EAGE. No lado esquerdo, a migração da seção de parâmetro de raio p = +0.2 s/km, e no lado direito, para p=0.0 s/km. A **Figura 9** exibe o resultado da migração da seção de p=-0.2 s/km.

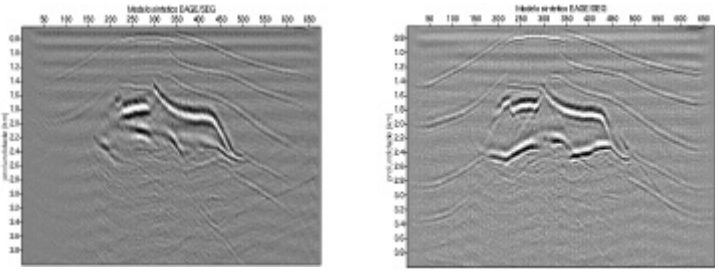

Figura 8: Migração em profundidade das seções de mesmo parâmetro de raio dos dados SEG/EAGE (à esquerda p=+0.2 s/km e p=0.0 s/km à direita).

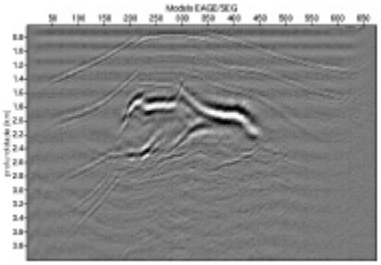

Figura 9: Resultado da migração em profundidade da seção de p=-0.2 s/km.

O resultado da migração obtido pela soma de 7 seções de parâmetro de raio constante de p=+0.2 s/km a p=-0.4 s/km, e com incrementos de –0.1 s/km, ou seja, imagem construída pela soma de 7 seções de p-constante migradas separadamente é mostrado na **Figura 10** (à esquerda). No lado direito, da mesma figura, é exibido o resultado obtido através da soma de 61 seções de mesmo parâmetro de raio, nesse caso de p=+0.2 s/km a p=-0.4 s/km, e com incrementos de –0.01 s/km.

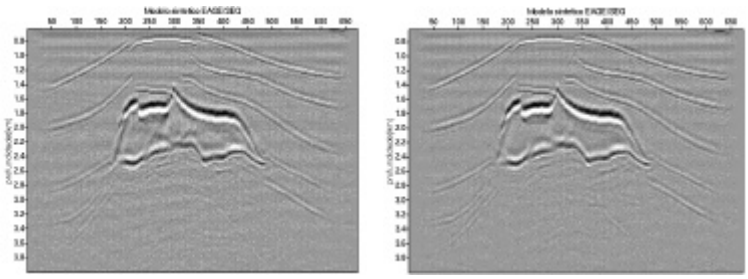

Figura 10: Migrações em profundidade obtidas a partir da soma de 7 seções de p-constante (lado esquerdo), e com a soma de 61 seções de mesmo parâmetro de raio (lado direito).

CONCLUSÕES

A presente migração de dados sísmicos, utilizando seções de parâmetros de raio constante, apresentou bons resultados, dentro das limitações do método, como confirmados pelos dois exemplos sintéticos exibidos. Pode-se constatar que a medida que mais seções migradas com mesmo parâmetro de raio, e relativas à valores mais elevados de parâmetro de raio, são somadas para a imagem final, melhora-se a visualização dos eventos de mais alto mergulho. Esta nova técnica de migração pré-empilhamento em profundidade nos possibilitou obter uma boa imagem de superfície a um custo computacional relativamente baixo. Com os dados do modelo SEG/EAGE, que apresenta uma almofada de sal com falhamentos, o resultado da migração de apenas 7 seções de p constante, já se aproximou bastante do resultado obtido com o uso de 61 seções de mesmo parâmetro de raio. Os resultados mostram que a base e o topo do sal foram bem posicionados. Este novo método de migração pré-empilhamento em profundidade pode ser aplicado em dados sísmicos 3-D e também ainda como um procedimento de análise de velocidade em função da sua eficiência computacional.

AGRADECIMENTOS

O primeiro autor agradece à Petrobrás e Reynam Pestana agradece ao CNPq pelo apoio através de bolsa de pesquisa, projeto no. 300312/88-1.

REFERÊNCIAS BIBLIOGRÁFICAS

Gazdag, J., (1978), Wave equation migration with the phase shift method, Geophysics, **43**:1342-1351.

Pestana, R. C. and Stoffa, P. L., (2001), Plane wave prestack time migration, J. Seismic Explor., 9: 223-233.

Stoffa, P.; Fokkema, J.; Freire, R. e Kessinger, W., (1990), Split-step fourier migraton, Geophysics, **55**:410-421.

Stolt, R., (1978), Migration by fourier transform, Geophysics, **43**:23-48.

Yilmaz, O., (1980), Pre-stack partial migration, Geophysics, **45**:1753-1779.

the Hubral and Krey algorithm, with the modifications discussed above.

Determination of the first layer. For a given central point X_0, draw from X_0 a straight line that makes an angle β_0 with the surface normal at X_0 and has length equals to $v_0 t_0/2$. The extreme of this segment of ray is the NIP. Do this for all central points that illuminate the first interface. To minimize the noise on this approximation, apply the smoothing process to the obtained curve and then adjust a cubic spline. We can now say that this first layer is completely determined.

Subsequent layers. Proceed as stated before, but now, the focusing conditions is *solved* in a least-squares sense. The curve composed by the recovered NIP's is smoothed and a cubic spline is adjusted to it to finally obtain the interface $(j+1)$.

Synthetic example

The method was applied to the model depicted in Figure 4, which consists of three interfaces separating four layers. The first and the fourth layers are homogeneous, with velocities 2.0km/s and 2.7km/s, respectively, and the second and third ones are inhomogeneous, with velocities varying from 2.2km/s to 2.4km/s and from 2.5km/s to 2.55km/s, respectively. The input data is the CRS

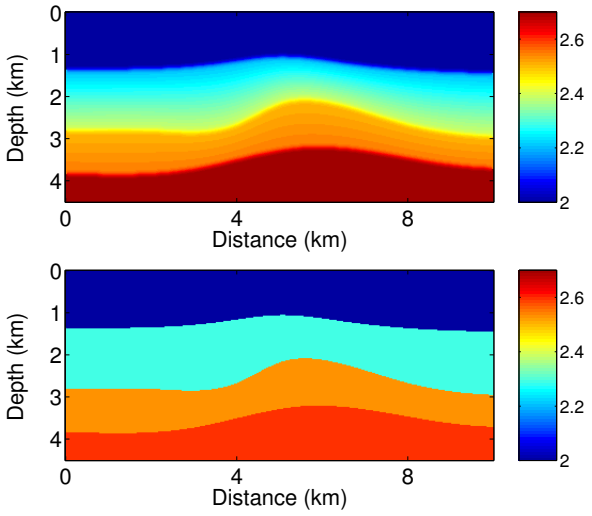

Figure 4: Top: synthetic model. Bottom: inverted model.

parameters obtained by the CRS Stack method performed on a noisy multi-coverage data. In Figure 4 we see the recovered model. Note that the velocity recovered for the second and the third layers are, in some sense, a mean of the actual velocities.

Conclusions

The contribution of this work is a new implementation of the Hubral and Krey algorithm, using the CRS parameters. We also discuss the numerical implementation of the algorithm, needed for a efficient application of the method. It is important to point out that the method works even if the *real* model does not fit in our assumptions, as in the case of inhomogeneous layers.

Concerning more complex velocities profiles, we could run the algorithm for separated parts of the domain. Thus, each inverted model would be composed by homogeneous layers that could be glued to form a complete inverted model (homogeneous by parts). This approach can be adopted independently of the inclusion of the possibility of velocity profiles depending on the depth.

We are intensively working to improve the algorithm so that the estimated velocity could linearly variates with the depth. This implies on some modification on the estimation of the layer velocities and on the ray tracing method, as well on the back-propagation of the wavefront.

Acknowledgements

This work was partially supported by FAPESP (Grant 97/12125-8) and by the sponsors of the WIT Consortium.

Migração Residual de Seções de Parâmetro de raio constante

Josair E. Gonçalves Júnior(*) , Reynam Pestana(*) e Paul L. Stoffa(**)

(*) CPGG/UFBA, (**)IG-UTEXAS

Abstract

In this paper we present a new method of prestack time residual migration derived in the plane wave domain. The data after slant stack transform along the offset direction is then organized in common ray parameter sections. For each commom ray parameter section the residual migration is applied. Here we present the prestack residual method for constant velocity medium and tested on the SEG/EAEG salt model. For comparison of the results we used the phase shift and Stolt plane wave time migration methods (Pestana and Stoffa (2001)). The results we obtained are reasonables and within the limitations of the method.

Introdução

Mais recentemente o processamento sísmico tem sido abastecido de novos métodos e técnicas que visam aprimorar as suas principais etapas e reduzir o custo computacional. Dentre essas etapas está a migração sísmica. Como referência tem-se a técnica da migração $F-K$ (Stolt (1978)), baseada no processo de migração através da transformada de Fourier. Essa técnica de migração possui um custo computacional relativamente baixo, entretanto não assimila variações de velocidade. Visando a melhoria dos resultados obtidos por essa migração $F-K$, Rocca and Salvador (1982) propuseram um meio de se corrigir os dados migrados com velocidade incorreta, possibilitando o colapso das difrações que não foram resolvidas na primeira migração (difrações residuais). Esse processo de correção consiste de uma migração residual dos dados, utilizando-se uma velocidade dada por $v_\xi = \sqrt{v^2 - v_o^2}$, onde v é a velocidade verdadeira do meio e v_o a velocidade usada na primeira migração. Em 1996, Stolt (1996) desenvolveu o operador de migração residual para dados antes do empilhamento. Mais recentemente, Pestana and Stoffa (2001) desenvolveram um operador de migração pré-empilhamento do tipo *Stolt* para dados no domínio tau-p.
Neste trabalho utilizamos as técnicas citadas acimas e desenvolvemos um novo método de migração residual aplicado em seções de parâmetro de raio constante.

Teoria e o Método

A migração do tipo Stolt (1978) implica numa operação de mudança da freqüência dependente das freqüências espaciais da fonte e do receptor. Esta mudança é expressa por:

$$\omega \Rightarrow \omega_m = \frac{1}{2}\left(\sqrt{\omega^2 - k_g^2 v_m^2} + \sqrt{\omega^2 - k_s^2 v_m^2}\right). \quad (1)$$

Supondo que uma velocidade incorreta v_0 foi utilizada na migração, resultando na freqüência modificada ω_0,

$$\omega_0 = \frac{1}{2}\left(\sqrt{\omega^2 - k_g^2 v_0^2} + \sqrt{\omega^2 - k_s^2 v_0^2}\right), \quad (2)$$

a obtenção da imagem final é possível executando-se uma migração residual nos dados através do mapeamento $\omega_0 \Rightarrow \omega_m$. Para isso precisamos reescrever ω_m em função de ω_0.
Elevando a equação 2 ao quadrado, isolando a raiz e novamente elevando ao quadrado, podemos obter ω em função de ω_0 dado pela relação (Stolt (1996)):

$$\omega^2 = \omega_0^2 + \frac{1}{2}(k_g^2 + k_s^2)v_0^2 + \frac{(k_g^2 - k_s^2)^2}{16\omega_0^2}v_0^4. \quad (3)$$

Podemos agora reescrever ω_m substituindo ω pela expressão de ω_0

$$\begin{aligned}\omega_m &= \frac{1}{2}\left[\sqrt{\left(\omega_0 + \frac{k_s^2 - k_g^2}{4\omega_0}v_0^2\right)^2 - k_g^2(v_m^2 - v_0^2)}\right. \\ &+ \left.\sqrt{\left(\omega_0 + \frac{k_g^2 - k_s^2}{4\omega_0}v_0^2\right)^2 - k_g^2(v_m^2 - v_0^2)}\right] \quad (4)\end{aligned}$$

obtendo assim o mapeamento residual de ω_m a partir de ω_0, para seções no domínio do número de onda de fonte-receptor. Partimos agora para a obtenção do operador residual no domínio do parâmetro de raio de afastamento p_0. Primeiramente vamos fazer a mudança do domínio do número de onda de fonte-receptor para número de onda da fonte-afastamento (Pestana and Stoffa (2001)) dado por:

$$k_s = k_s' - k_0 \quad (5)$$
$$k_g = k_0 \quad (6)$$

Fazendo uma segunda mudança de domínio, do domínio dos números de onda do afastamento e da fonte, $k_s^{'} - k_0$, para o domínio do número de onda da fonte e parâmetro de raio do afastamento, $k_s^{'} - p_0$, através da seguinte relação:

$$p_0 = \frac{k_0}{\omega} \Longleftrightarrow k_0 = \omega p_0 \tag{7}$$

Através dessas mudanças de variáveis, obtemos o operador de migração no domínio do número de onda da fonte e do parâmetro de raio do afastamento, que é dado por:

$$\omega_m = \frac{1}{2}\left[\omega_0\sqrt{(1+A')^2 - p_0^2(v_m^2 - v_0^2)} + \sqrt{(\omega_0 + B')^2 - (k_s - \omega_0 p_0)^2(v_m^2 - v_0^2)}\right] \tag{8}$$

onde;

$$A' = \frac{(k_s - \omega_0 p_0)^2 - \omega_0^2 p_0^2}{4\omega_0^2} v_0^2 \tag{9}$$

e

$$B' = \frac{\omega_0^2 p_0^2 - (k_s - \omega_0 p_0)^2}{4\omega_0} v_0^2 \tag{10}$$

Notemos agora que sem a presença dos termos $A^{'}$ e $B^{'}$ o operador residual tem a mesma forma do operador inicial (Eq. 2), apenas com as alterações de domínio e pela substituição $v_m^2 - v_0^2 = v_\xi^2$ que é a velocidade residual.

No gráfico da figura 2 está representado a razão entre o $\omega_{ab}^{'}$, que é ω calculado com os parâmetros $A^{'}$ e $B^{'}$, e $\omega^{'}$, calculado desprezando-se esses parâmetros. O gráfico foi feito com uma variação do parâmetro de raio p_0 de $-0{,}40 \leq p_0 \leq 0{,}20\ s/km$ e do parâmetro de raio de tiro p_s também de $-0{,}40 \leq p_s \leq 0{,}20\ s/km$. Foram traçados gráficos para velocidades iniciais v_0 de $1{,}40\ km/s \leq v_0 \leq 4{,}5 km/s$, sendo que o maior valor de erro encontrado foi de 0.07.
A partir desses resultados os parâmetros $A^{'}$ e $B^{'}$ puderam ser considerados como desprezíveis. Esse fato levou a conclusão de que para a migração Stolt o operador residual;

$$\omega_m = \frac{1}{2}\left[\omega_0\sqrt{1 - p_0^2 v_\xi^2} + \sqrt{\omega_0^2 - (k_s - \omega_0 p_0)^2 v_\xi^2}\right] \tag{11}$$

tem a mesma forma do operador inicial. Sendo então os dados remigrados com a velocidade residual v_ξ.

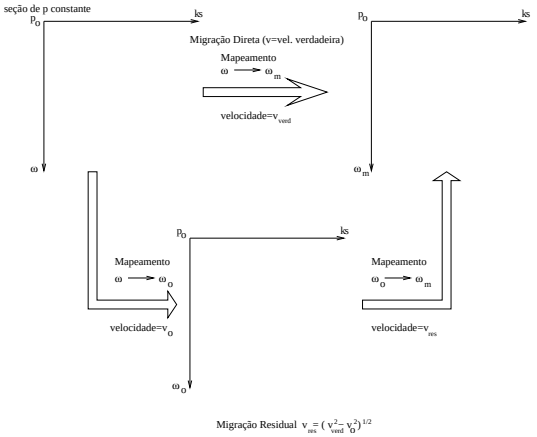

Figura 1: Esquema gráfico representando as mudanças na freqüência devido à migração direta e a migração residual.

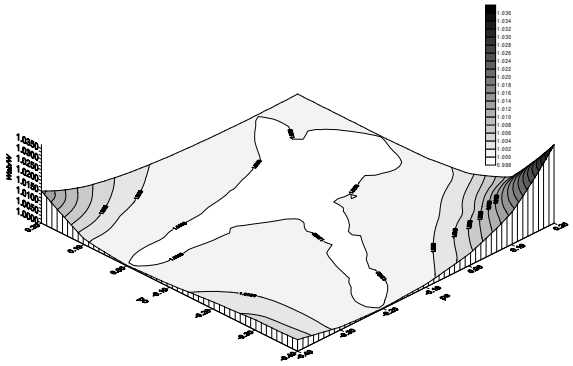

Figura 2: Razão entre $\omega_{ab}^{'}$ e $\omega^{'}$ (calculado desprezando-se $A^{'}$ e $B^{'}$), para uma variação de p_0 e p_s de -0,4 $\pm$ x $\pm$ 0,2 s/km e $v_0 = 1{,}8\ km/s$ e $v_{verd} = 2{,}2\ km/s$.

Aplicação em modelo sintético

O modelo utilizado para o teste foi o SEG/EAGE, representando uma almofada de sal e diversos falhamentos. Os dados sísmicos correspondem a 675 registros de tiro, cada um com 61 parâmetros de raio, variando de -0,4 até +0,2 s/km, com comprimento de registro de 1250 amostras (5s) cada.
A migração phase shift em tempo de seções de parâmetro de raio (Pestana and Stoffa (2001))foi aplicada nos mesmos dados, utilizando-se o modelo de velocidade intervalar em tempo (Fig. 3) constituido de 675 amostras em x e 1250 amostras no tempo, para efeito de comparação dos resultados.

A aplicação da migração residual no modelo foi realizada em 4 etapas. Na primeira etapa deter-

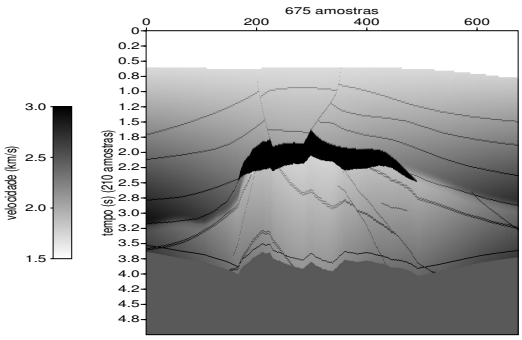

Figura 3: Modelo de velocidade em tempo do SEG/EAGE simulando uma almofada de sal e diversos falhamentos

minamos o campo de velocidade a ser utilizado em todo o processo. O campo de velocidade utilizado foi gerado contendo 3 faixas de velocidade distintas. A primeira faixa, com velocidade $v_1 = 1,8$ km/s, compreendida no intervalo de 0 a $1,10s$ (0-275 amostras), a segunda faixa, com velocidade $v_2 = 2,0km/s$, no intervalo de $1,10$ e $1,85s$ (175 amostras). A última faixa inicia em $1,85s$ estendendo-se até o final da seção, com velocidade $v_3 = 2,2km/s$.

A migração inicial foi executada com a velocidade v_1 da primeira faixa. Em seguida foi realizado um primeiro corte nos dados retirando-se toda a primeira faixa migrada. A seção resultante foi submetida a segunda migração, com velocidade residual $v_{\xi_1} = 0,87km/s$. Um segundo corte foi realizado nos dados com o objetivo de retirar a faixa intermediária. A última porção dos dados foi então migrada com a velocidade residual $v_{\xi_2} = 0,92km/s$. Através desse procedimento podemos obter todas as faixas devidamente migradas. Em seguida iniciou-se o processo de junção das seções, partindo de baixo, a terceira faixa foi unida a segunda e posteriormente unida a primeira.

A figura 4 mostra algumas seções CIG ("commom image gathers"), obtidas com a migração residual. Comparando os resultados da migração residual (Fig. 4a) com os da migração Stolt convencional (Fig. 4b) podemos perceber uma grande melhora no resultado da migração, com o melhor alinhamento dos parâmetros de raio na seção migrada residualmente, e com o colapso da difração existente no refletor localizado aproximadamente em 1,8s, que a migração Stolt convencional não conseguiu colapsar.

Comparando os resultados obtidos com os da migração phase shift (Fig. 4b), considerada como ideal para efeito de comparação, podemos observar uma boa relação no alinhamento dos parâmetros de raio das duas seções. Nas seções empilhadas, podemos observar respostas bem parecidas entre as duas técnicas empregadas, com a migração phase-shift sobressaindo na delimitação do flanco esquerdo da almofada de sal e pelo colapso das difrações nas falhas localizadas entre 6 e 7 km e 1,0 a 2,0 s. Em contrapartida o tempo foi um grande trunfo da migração residual, já que todo o seu processo foi desenvolvido em três horas, enquanto a migração phase-shift foi realizada em aproximadamente quinze horas num computador Pentium III 750MHz com 1Gb de memória RAM.

Conclusão

A migração residual de seções de parâmetro de raio constante apresentou resultados bastante satisfatórios, com uma boa relação de custo-benefício. O método destaca-se pela sua rapidez de processamento (vantagem da migração Stolt) e pela possibilidade de se incorporar faixas de velocidade distintas com o tempo, um empecilhio da migração Stolt. Os resultados demonstraram uma melhora considerável em relação a migração Stolt convencional e mostraram-se comparáveis aos obtidos com a migração phase shift em tempo.

Agradecimentos

Os autores agradecem ao CPGG/UFBA pelo suporte operacional. O primeiro autor agradece a ANP pela oportunidade de trabalhar nesta pesquisa e pelo suporte financeiro através de um bolsa de graduação. Reynam Pestana agradece também ao CNPq pelo apoio através de bolsa de pesquisa, projeto no. 300312/88-1.

Referências

Pestana, C. P., and Stoffa, P. L., 2001, Plane wave prestack time migration: J.Seismic Explor., **9**, no. 3, 211,222.

Rocca, F., and Salvador, L., 1982, Residual migration Residual migration, Annual Meeting Abstracts, S1.4.

Stolt, R. H., 1978, Migration by fourier transform: Geophysics, **43**, no. 01, 23–48.

Stolt, R. H., 1996, A prestack residual time migration operator: Geophysics, **61**, no. 02, 605–607.

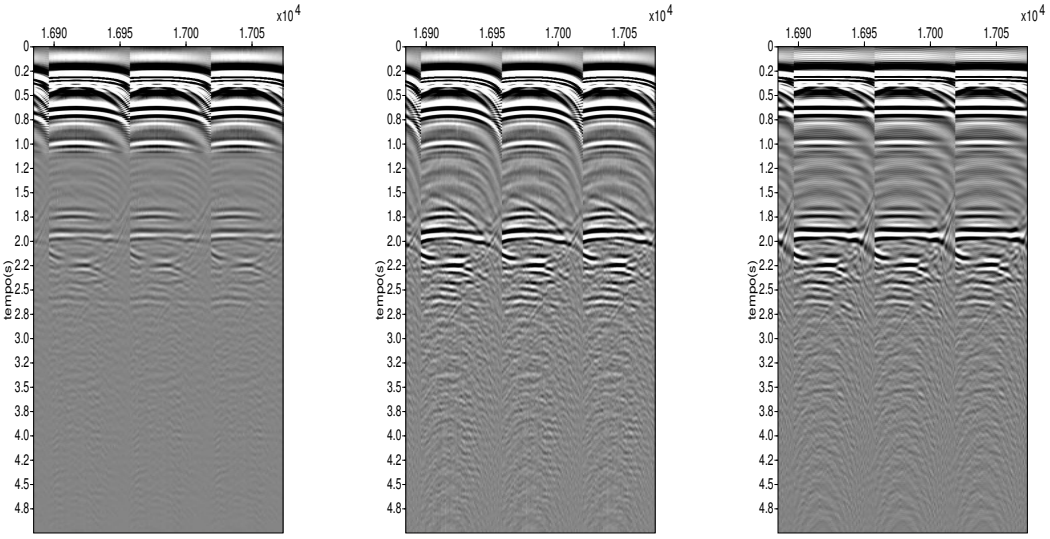

(a) (b) (c)

Figura 4: Modelo da SEG/EAGE.(a) Migração residual Stolt com 3 janelas de velocidade; (b) Migração Stolt convencional com $v_{st_2} = 2,0\ km/s$;(c) Migração phase shift (Pestana and Stoffa (2001))

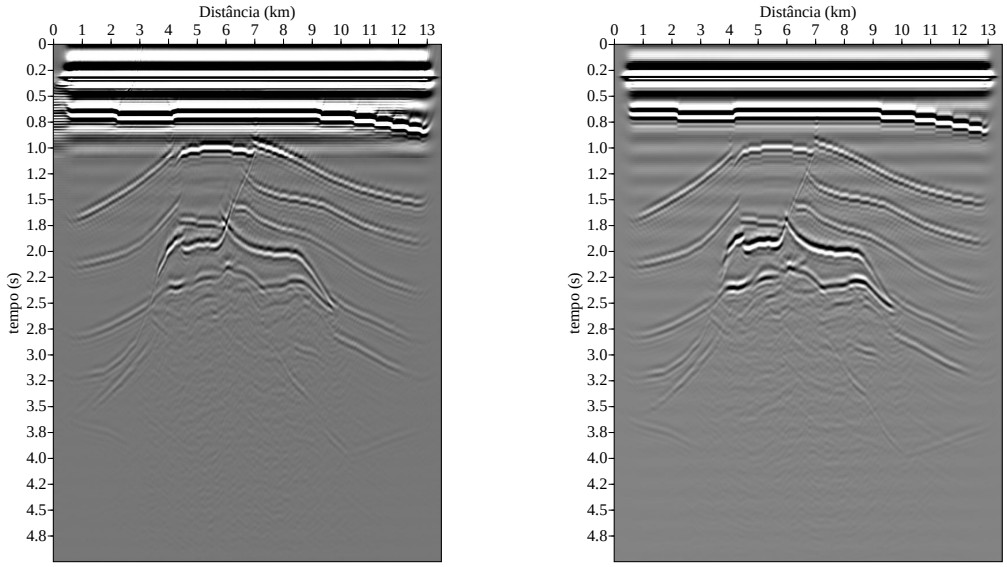

(a) (b)

Figura 5: (a) Seção residual final obtida pela soma das 61 seções de parâmetro de raio constante migradas individualmente; (b) Seção final migrada pelo método phase shift (Pestana and Stoffa (2001)) obtida pela soma das 61 seções de parâmetro de raio constante

Migração Reversa no Tempo 2-D: Estabilidade em relação à Suavização do Modelo de Velocidades e às Reflexões Laterais

André Bulcão; COPPE/UFRJ; Brasil
Djalma M.S. Filho; CENPES/PETROBRAS S/A; Brasil
Webe J. Mansur; COPPE/UFRJ; Brasil

Introdução

Neste trabalho realiza-se uma análise qualitativa das imagens em profundidades, obtidas a partir da simulação bidimensional do esquema de Migração Reversa no Tempo via Método das Diferenças Finitas, verificando-se a estabilidade da metodologia em relação à suavização do campo de velocidades; também são apresentados alguns testes relativos à presença de reflexões laterais provenientes do emprego de um sismograma obtido através de uma modelagem acústica 3-D.

A metodologia adotada mostrou-se extremamente eficaz na identificação de camadas contendo um elevado contraste de velocidades, como no caso simulado numericamente onde se tem a presença de um domo de sal no modelo geológico, com diferentes níveis de suavização do campo de vagarosidade e com fortes reflexões laterais.

Modelo Geológico

Utilizou-se um modelo geológico baseado no modelo proposto pela SEG/EAGE [1], apresentando características típicas do Golfo do México, com a presença de um domo de sal em seu interior. As alterações realizadas foram, basicamente, um acréscimo de 500 metros na lamina d'água existente no modelo original, cortes em suas laterais, e a realização de um *resample* alterando-se o espaçamento do *grid* de 25 m para 12.5 m.

Um ponto importante a ser destacado neste modelo geológico são as interfaces estratigráficas entre suas camadas. Excluindo-se tais interfaces o modelo de velocidades apresenta uma variação muito suave nos valores de sua impedância acústica, sendo que as únicas camadas que se encontram bem definidas pelo valor da impedância são: a lâmina d'água e o domo de sal.

Nas modelagens acústicas 3-D o modelo geológico empregado é composto por 1061 x 1061 x 459 pontos do *grid*, respectivamente para as direções X, Y e Z, perfazendo um paralelepípedo de 13.250 x 13.250 x 5.725 Km. A velocidade de propagação da onda neste modelo possui uma variação de 1500 m/s, referente a lâmina d'água, a até aproximadamente 4500 m/s no domo de sal.

A seguir, na figura 1, apresentam-se alguns planos de corte ao longo do modelo geológico. Destaca-se na figura 1b plano de corte ao longo da direção Y (seção Y) empregado nas migrações e nas modelagens acústicas 2-D realizadas neste trabalho.

Metodologia

Os resultados das simulações numéricas apresentadas a seguir, Modelagens Acústicas e Migrações Reversas no Tempo, foram obtidos com o emprego do Método das Diferenças Finitas utilizando-se de operadores centrais de 2ª e 4ª ordens, respectivamente para as derivadas temporais e espaciais presentes na equação diferencial que rege a propagação de ondas acústicas [2].

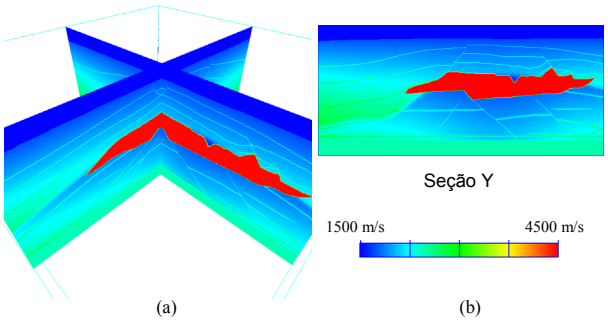

Figura 1 – (a) planos de corte ao longo do modelo geológico 3-D, perpendiculares às direções coordenadas; (b) seção Y, plano de corte ao longo da direção Y.

Para as modelagens acústicas 3-D desenvolveu-se um software que lança mão dos recursos do processamento em paralelo, através do uso das bibliotecas do PVM (*Parallel Virtual Machine*), tornando possível tais simulações em um *cluster* de microcomputadores. A estratégia de paralelismo empregada é a Decomposição de Domínio (*Domain Decomposition*) [3].

A modelagem acústica do modelo geológico 3-D demandou um total de 5.75 Gb de memória. Considerando-se apenas a seção Y, simulação 2-D, necessitou-se de 5.58 Mb de memória para as modelagens acústicas, e nas migrações de 9.30 Mb.

Suavização do Campo de Velocidades

Um fator de fundamental importância nos algoritmos de migração é a suavização do campo de vagarosidade (S) (i.e., o inverso do campo de velocidade). Para tal fim, nas simulações 2-D, empregou-se a média móvel aplicada ao longo das direções coordenadas, equação 1, sendo n o numero de amostras empregadas.

$$\overline{S}(i) = \sum_{-n}^{+n} \frac{S(i)}{2n+1} \qquad (1)$$

Resultados Numéricos

Apresentam-se na tabela 1 os principais parâmetros utilizados nas simulações numéricas, tanto para o modelo geológico 3-D quanto para o 2-D.

Inicialmente realizaram-se as modelagens acústicas 2-D e 3-D, obtendo-se para a seção Y os respectivos sismogramas. Observa-se que, de acordo com a figura 2, no sismograma 3-D há a presença de reflexões

laterais que não se encontram no 2-D, acarretando em uma maior complexidade. Tais reflexões competem em ordem de grandeza com as oriundas das reflexões ao longo da seção Y, fazendo com que as reflexões sobre a seção Y não apareçam em destaque no sismograma 3-D. Na figura 7 apresentam-se 2 planos de corte no modelo de velocidades 3-D e alguns *snapshots* onde se observam as reflexões laterais.

Tabela 1 – Parâmetros utilizados nas simulações 2-D e 3-D.

Espaçamento da malha (*grid*) - (h)	12.5 m
Intervalo de tempo	0.0005 s
Tempo total de análise	6.0 s
Intervalo para saída de *snapshot*s	0.1 s
Freqüência de corte	28 Hz

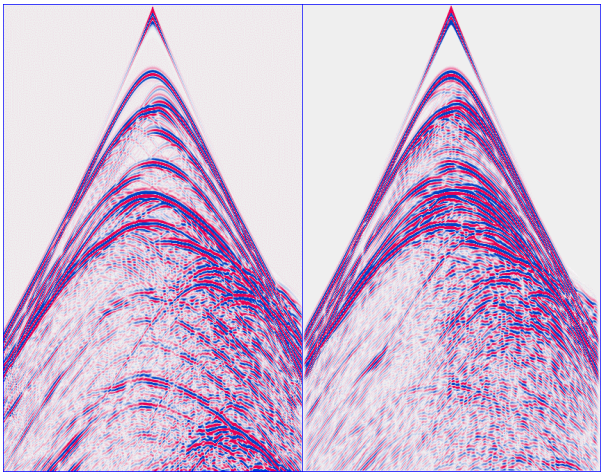

2-D 3-D

Figura 2 – Sismogramas oriundos das modelagens acústicas 2-D e 3-D.

Os sismogramas apresentados foram utilizados pelo algoritmo de Migração Reversa no Tempo bidimensional. No algoritmo de migração como condição de imagem utilizou-se o valor máximo da amplitude ao longo do tempo total de análise durante a modelagem [4].

Inicialmente apresentam-se as imagens em profundidade empregando-se apenas uma única fonte sísmica, obtida a partir do sismograma 2-D e com o campo de vagarosidade não suavizado. Está corresponde a simulação numérica onde se espera alcançar uma imagem em profundidade com a melhor qualidade. A figura 3 ilustra a situação, onde se tem a imagem sem nenhum tratamento prévio (figura 3a), apenas com um ganho para ressaltar as baixas amplitudes. Na figura 3b tem-se esta mesma imagem após a aplicação de um filtro polinomial [5], cortando os baixos números de onda presentes na imagem inicial.

Destaca-se que algumas das imagens em profundidade apresentadas a partir deste ponto foram tratadas com a aplicação do mesmo procedimento empregado na figura 3b, isto é, fazendo-se uso de um filtro polinomial.

A seguir na figura 4 faz-se uma análise qualitativa da estabilidade da metodologia empregada em função da suavização do campo de velocidades, variando-se o numero de amostras utilizadas para tal.

A utilização da suavização do campo de vagarosidade na Migração Reversa no Tempo faz com que se altere a aparência da condição de imagem, pois se alteram os contrastes do modelo de velocidades e conseqüentemente o tempo de transito e as amplitudes registradas durante a propagação das ondas sísmicas.

Na figura 5 têm-se algumas imagens do campo de velocidades, obtidas a partir da superposição de 29 imagens para diferentes posições da aplicação da fonte sísmica, variando-se o número de amostras empregadas na suavização do campo de vagarosidade. As posições das fontes no *grid* são: 110, 160, 210, 260, 310, 360, 410, 460, 470, 480, 490, 500, 510, 520, 530, 540, 550, 560, 570, 580, 590, 600, 650, 700, 750, 800, 850, 900 e 950.

A figura 6 apresenta as imagens em profundidades comparando-se os resultados obtidos com o algoritmo de migração bidimensional, com a aplicação de apenas uma única fonte sísmica, utilizando-se os sismogramas 2-D e 3-D. O campo de vagarosidade encontra-se suavizado empregando-se 9 amostras.

Conclusões

A aplicação de um filtro polinomial mostrou-se um excelente recurso para melhor acentuar as interfaces das camadas do modelo de velocidades presentes nas imagens em profundidade obtidas a partir do algoritmo de migração reversa no tempo.

O esquema de migração empregado revelou-se estável em relação à suavização do campo de vagarosidade. De acordo com os resultados apresentados observou-se que à medida que se aumenta o número de amostras utilizadas para a suavização torna-se mais difícil à obtenção de imagens das estruturas que se encontram abaixo do domo de sal, pois a suavização do campo de vagarosidade acarreta em um erro na avaliação do tempo de transito e nos valores de amplitude, o que prejudica a formação correta da imagem em profundidade.

De maneira geral o algoritmo de migração mostrou-se extremamente robusto, a ponto de gerar uma imagem em profundidade representando o topo e base do domo de sal, mesmo quando da presença de reflexões laterais no sismograma empregado para a migração (i.e., considerando-se o uso do sismograma 3-D em uma análise 2-D), obtendo-se, desta forma, resultados com uma qualidade semelhante à obtida com o uso do sismograma 2-D.

Referências Bibliográficas

[1] – Aminzadeh, F.; Brac, J.; Kunz, T.; (1996), 3-D Salt and Overthrust Models, *SEG/EAGE 3-D Modeling Series*, n. 1.

[2] – Bording, R.P.; Lines, L.R.; (1997); *Seismic Modeling and Imaging with Complete Wave Equation*; Course Notes Series, N. 8; Society of Exploration Geophysicists.
[3] – Bragança, R.S.N.; Bulcão, A.; Soares, D.M.F.; Mansur, W.J.; (2001), Modelagem Sísmica 3-D em Clusters - Análise de Performance, *7th International Congress of the Brazilian Geophysical Society*.
[4] – Botelho, M.A.B.; Stoffa,P.L.; (1988), *Velocity Analysis Using Reverse Time Migration*, AGU, AGU.
[5] – Cohen, J.K.; Stockwell, Jr.J.W.; (1998); *The New User's Manual; Center of Wave Phenomena*, Colorado School of Mines.

Agradecimentos

À PETROBRÁS por proporcionar os meios necessários e pela permissão para a publicação deste artigo. Ao CNPq projeto 462304/00-0 (NV) por financiar parte deste trabalho junto a UFRJ.

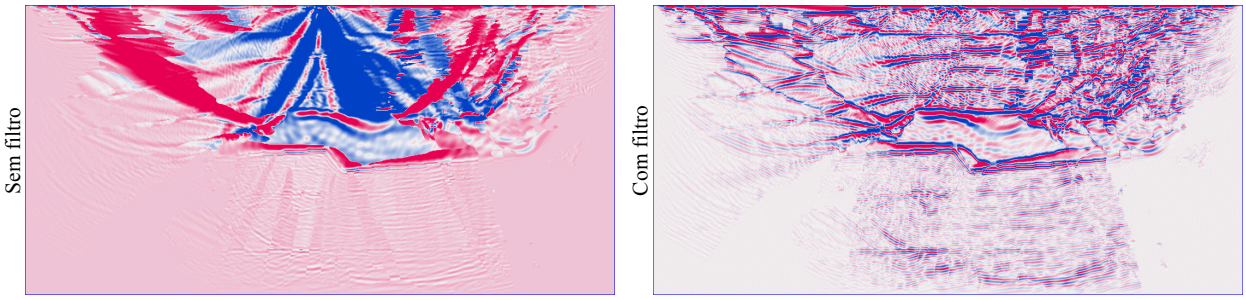

Figura 3 – Imagens em profundidade, provenientes da Migração Reversa no Tempo 2-D, empregando o campo de vagarosidade não suavizado e o sismograma 2-D. 1(a) – Imagem sem filtro; 1(b) – Imagem com filtro cortando os baixos números de onda.

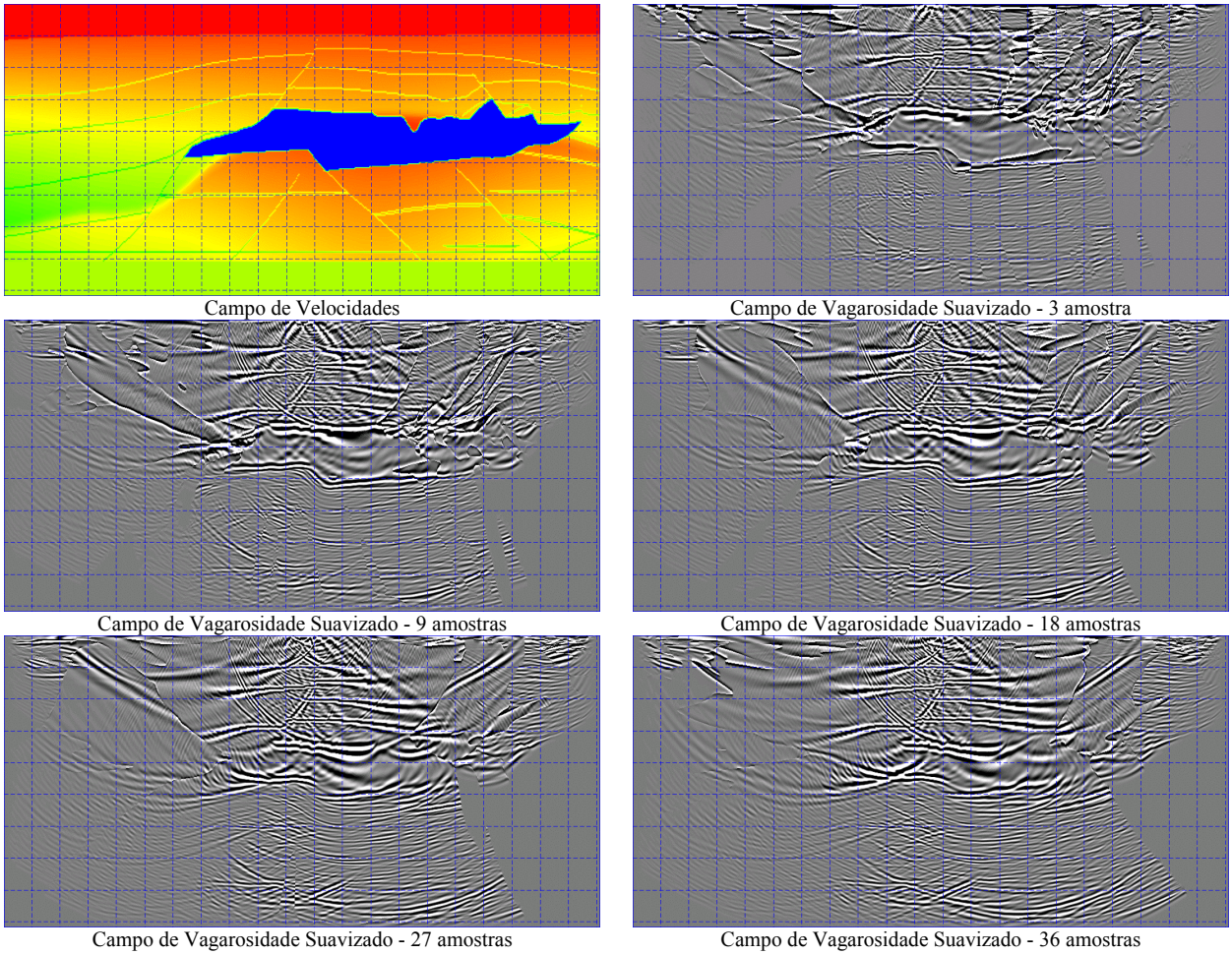

Figura 4 – Modelo de velocidades e Imagens em profundidade com o campo de vagarosidade contendo diferentes níveis de suavização, provenientes da Migração Reversa no Tempo 2-D com apenas uma única fonte sísmica, empregando o sismograma 2-D.

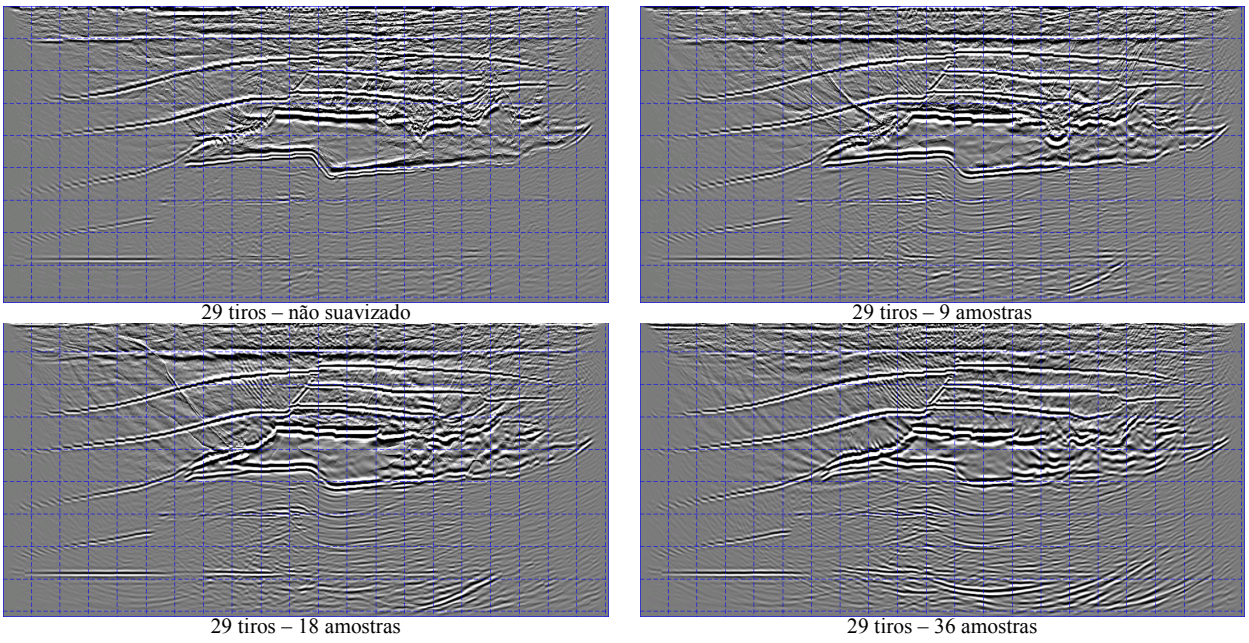

Figura 5 – Imagens em profundidade, com o campo de velocidades contendo diferentes níveis de suavização, provenientes da Migração Reversa no Tempo 2-D com a superposição de 29 fontes sísmicas (empregando-se os sismogramas 2-D).

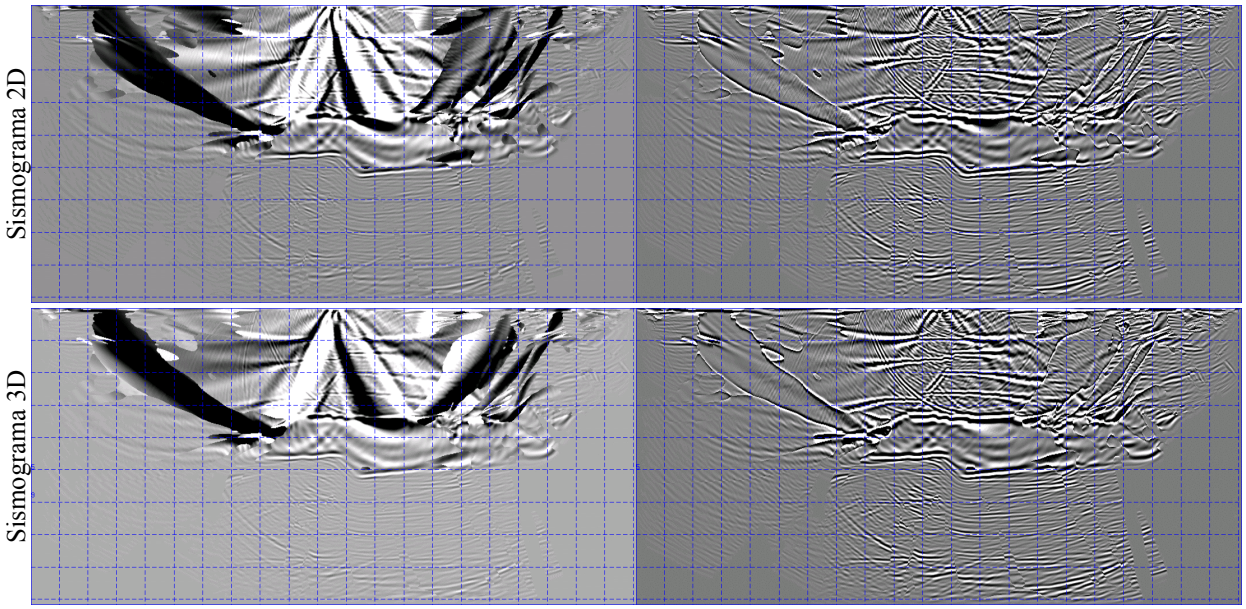

Figura 6 – Imagens em profundidade, provenientes do algoritmo de migração 2-D, utilizando-se os sismogramas obtidos da modelagem acústica 2-D e 3-D, aplicação de apenas uma única fonte sísmica (campo de vagarosidade suavização com 9 amostras).

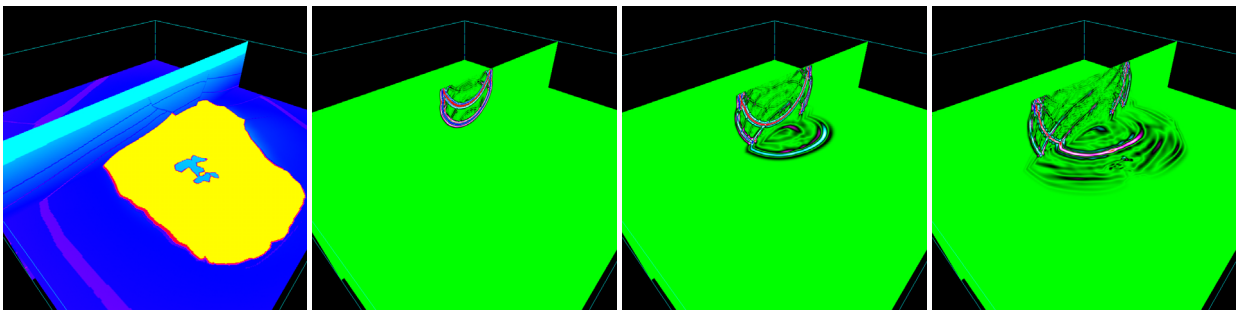

Figura 7 – Planos de corte no modelo de velocidades 3-D e alguns *snapshots* para diferentes instantes de tempo.

New advances in the Common-Reflection-Surface Stack

Jürgen Mann†, Steffen Bergler†, German Höcht†, and Peter Hubral†

Abstract

The Common-Reflection-Surface Stack was originally introduced as a data-driven method to simulate zero-offset sections from 2-D seismic reflection pre-stack data. The noteworthy results received for various synthetic and real data examples encouraged us to transfer the approach to more general problems, namely the simulation of finite-offset sections for 2-D pre-stack data as well as the simulation of zero-offset volumes for 3-D data. In this contribution, we focus on these generalizations of the Common-Reflection-Surface Stack and briefly indicate implementation strategies for the zero-offset simulation in 3-D and the finite-offset simulation in 2-D.

Introduction

The Common-Reflection-Surface (CRS) Stack was introduced by Müller (1998) and Müller et al. (1998) as a data-driven zero-offset (ZO) simulation method for 2-D that does not require an explicit knowledge of the macro velocity model. The underlying model assumptions of the CRS stack method are more general than the models of, e. g., Kirchhoff migration or normal moveout/dip moveout/stack which are based on diffractors or ZO isochron segments in the subsurface, respectively. The CRS stack assumes the subsurface to be set up by reflector segments with arbitrary location, orientation, and curvature. Obviously, this subsurface model is more appropriate to describe reflectors in the subsurface than any other method based on a less general approach.

A model-based application of the CRS stack is hardly applicable as it requires a detailed description of the model including all interfaces—a smooth macro velocity model is not sufficient for this task. However, in the scope of paraxial zero-order ray theory, the three properties of the reflector segment are associated with a set of wavefield attributes that represent propagation directions and curvatures of certain hypothetical wavefronts. With these wavefield attributes, an analytic approximation of the kinematic reflection response of the reflector segment can be derived. This approximate response, in the following also called CRS stacking operator, and its associated wavefield attributes can be directly determined from the pre-stack data by means of coherence analysis. In other words, the optimum CRS stacking operator for a particular ZO sample to be simulated can be determined in a data-driven way without the need to know the actual location, orientation, and curvature of the corresponding reflector segment. Thus, the CRS stack approach implies a generalization of the well-known velocity analysis. However, instead of only one wavefield attribute, the stacking velocity,[1] the CRS stack provides an entire set of wavefield attributes that parameterize the subsurface model and serve for various applications.

Applications of the CRS stack for the simulation of 2-D ZO sections can be found in Mann et al. (1999) and Jäger et al. (2001). Further improvements of the "classic" CRS stack for 2-D, namely the handling of conflicting dip situations, were introduced by Mann (2001).

3-D zero-offset simulation

For the ZO case, the reflector segment's properties and the associated wavefield attributes are related to each other by two hypothetical experiments. For ZO, we assume only unconverted primary events with normal incidence on the reflecting interface. In this case, the up-going and down-going ray branches coincide. The up-going ray branch is called the normal ray in the following. For the first experiment, a point source is placed at the normal incidence point (NIP) of the normal ray on the reflector segment. The wavefront emanating from this experiment, the so-called NIP wave, propagates along the normal ray and emerges at the acquisition surface with well-defined curvature and propagation direction. In the second experiment, a simultaneous excitation of the entire reflector segment (exploding reflector experiment) is performed to obtain the so-called normal wave. Again, a wavefront propagates along the normal ray and emerges with a certain curvature and the same propagation direction as in the first experiment.

For the 2-D case, both curvatures as well as the propagation direction can be expressed as

†Geophysical Institute, University of Karlsruhe, Germany

[1] In 3-D, the stacking velocity in general depends on the azimuth.

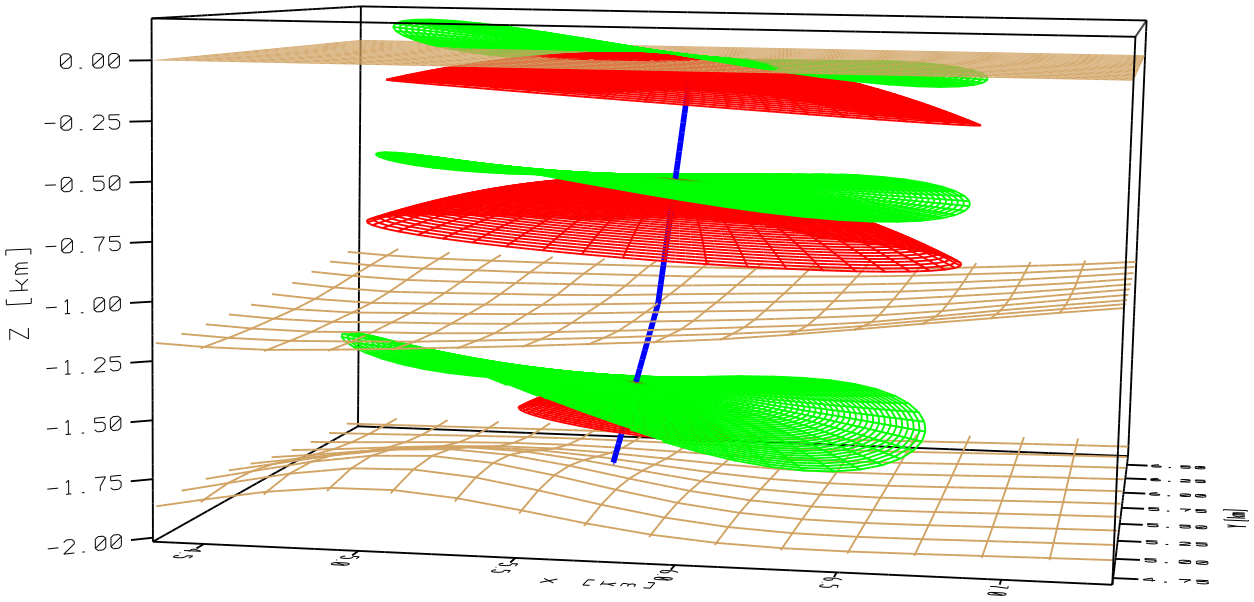

Figure 1: Hypothetical experiments yielding the wavefield attributes for the 3-D CRS stack for ZO. The normal ray (bold blue line) connects the normal incidence point on the second interface (brown grid) with the acquisition surface (brown plane). The red and green surfaces represent the emerging NIP and normal wavefronts, respectively, for three different instances of time.

scalars. Thus, we receive three wavefield attributes for this simplest case. The 2-D ZO case was thoroughly discussed by Mann et al. (1999) and Jäger et al. (2001). These concepts can be immediately generalized to the 3-D case by performing the same hypothetical experiments as in 2-D. Some snapshots of the emerging wavefronts are displayed in Figure 1 for a model consisting of three homogeneous layers. Obviously, the curvatures can no longer be described by scalars but take the form of 2×2 matrices. The propagation direction can now be described by a unit vector with three components or, more convenient, by its projection onto the acquisition surface. Considering the symmetry of the curvature matrices, we come up with a set of eight wavefield attributes. Nevertheless, the hyperbolic CRS stacking operator formally remains the same as for the 2-D case:

$$t^2 = \left(t_0 + \frac{2}{v}\, \mathbf{w_z} \circ \mathbf{m} \right)^2 + \frac{2\, t_0}{v}\, \mathbf{m}^{\mathrm{T}}\, \hat{\mathbf{A}}\, \mathbf{m} + \frac{2\, t_0}{v}\, \mathbf{h}^{\mathrm{T}}\, \hat{\mathbf{B}}\, \mathbf{h}\ . \tag{1}$$

The matrices $\hat{\mathbf{A}}$ and $\hat{\mathbf{B}}$ depend on the curvatures of the normal and the NIP wave, respectively, and the projected propagation direction $\mathbf{w_z}$. The vectors $\mathbf{m}$ and $\mathbf{h}$ denote the relative midpoint displacement and the half offset, respectively. As in the 2-D case, t_0 is the traveltime to be simulated, and v denotes the near-surface velocity.

To fit the optimum stacking operator to an actual reflection event, a global optimization in an eight-dimensional parameter domain is required. However, the computational effort for such an optimization is unacceptable. Similar to the implementation strategy for 2-D (see, e. g., Jäger et al., 2001), the eight-parameter problem can be split into separate optimizations with less parameters. Among other strategies, one way to solve this problem is to decompose it into a set of 2-D problems: in case of sufficient azimuthal coverage in the prestack data, the CRS stack for 2-D can be applied independently for lines with three different azimuths. The 3×3 wavefield attributes from this approach can be combined to the eight wavefield attributes in Equation (1).

In case of poor azimuthal coverage, the curvature of the NIP wavefront cannot be fully determined because of the lack of information in the acquired data: if, e. g., only one small azimuth range is covered, the five-dimensional $(t, \mathbf{m}, \mathbf{h})$ data domain is virtually four-dimensional as all half-offset vectors $\mathbf{h}$ are almost parallel. An additional assumption, e. g., spherical NIP wavefronts, is required for a complete description of the CRS stacking operator.

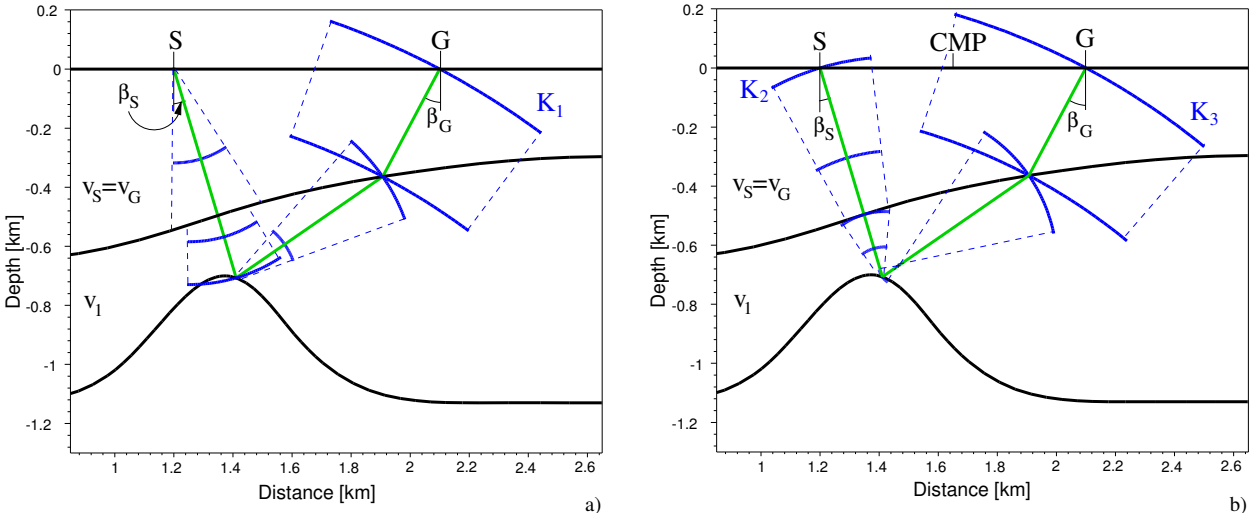

Figure 2: Hypothetical experiments yielding the wavefield attributes for the 2-D CRS stack for FO. The FO ray (bold green line) connects the reflection point on the second interface with the acquisition surface. The blue lines represent the a) CS and b) CMP wavefronts, respectively, for different instances of time. The propagation directions along the FO ray are given by β_S and β_G at the shot and the receiver, respectively. K_1, K_2, and K_3 denote the wavefront curvatures at the indicated locations.

2-D finite-offset simulation

For ZO simulation, we considered rays with coincident up-going and down-going ray branches. However, in case of finite offset (FO) and/or converted waves, the two ray branches no longer coincide. However, the described two hypothetical experiments with NIP and normal wavefronts provide only information about the reflector segment and the propagation along the normal ray. Thus, different hypothetical experiments are required to associate the reflector segment's properties with wavefield attributes in the time domain—these experiments have to provide information about *both* ray branches of the FO ray.

Appropriate hypothetical experiments for the FO case were introduced by Zhang et al. (2000). The first experiment is the so-called common-shot (CS) experiment[2] for which a point source is placed in the shot point of the considered FO ray. The CS wavefront propagates along the down-going ray branch, is reflected at the reflector segment, and propagates back to acquisition surface along the up-going ray branch. This experiment defines three wavefield attributes, namely the curvature of the wavefront K_1 emerging at the receiver and the propagation direction along the FO ray at the source and the receiver, respectively. The propagation directions can be described by the angles between the FO ray branches and the acquisition surface normal. The CS experiment is depicted in Figure 2a for a model consisting of three homogeneous layers.

The second experiment, the so-called common-midpoint (CMP) experiment[2], is more difficult to explain: the initial curvature of the wavefront starting at the source is now no longer zero (as in the CS experiment) but takes a finite value K_2. This wavefront also propagates along the FO ray via the reflecting interface to the receiver and emerges with the curvature K_3 (see Figure 2b). The propagation direction along the FO ray is the same as for the CS experiment. Thus, we come up with a a set of five wavefield attributes for the FO case. For offset zero, the number of attributes again reduces to three: the two angles, β_S and β_G, coincide and the three curvatures, K_1, K_2, and K_3, can be expressed in terms of the two curvatures related to the normal and NIP wave experiment introduced for the ZO case.

The hyperbolic approximation of the kinematic reflection response of the reflector segment for FO in terms of the five wavefield attributes is given in Equation (2). (t_0, x_0, h_0) defines the FO sample to be simulated, whereas x_m and h denote the midpoint and half-offset coordinates of the contributing traces. The near-surface velocities at shot

[2] "Common" refers to the paraxial rays in the vicinity of the central FO ray.

$$
\begin{aligned}
t^2 = & \left[t_0 + \left(\frac{\sin\beta_G}{v_G} + \frac{\sin\beta_S}{v_S} \right) (x_m - x_0) + \left(\frac{\sin\beta_G}{v_G} - \frac{\sin\beta_S}{v_S} \right) (h - h_0) \right]^2 \\
& + 2\,t_0 \left[(x_m - x_0) \left(K_3 \frac{\cos^2\beta_G}{v_G} + K_2 \frac{\cos^2\beta_S}{v_S} \right) (h - h_0) \right. \\
& + \frac{1}{2} (x_m - x_0) \left((4\,K_1 - 3\,K_3) \frac{\cos^2\beta_G}{v_G} - K_2 \frac{\cos^2\beta_S}{v_S} \right) (x_m - x_0) \\
& \left. + \frac{1}{2} (h - h_0) \left(K_3 \frac{\cos^2\beta_G}{v_G} - K_2 \frac{\cos^2\beta_S}{v_S} \right) (h - h_0) \right] .
\end{aligned}
\tag{2}
$$

and receiver are given by v_S and v_G, respectively. Similar to the ZO case, the search for these attributes can be performed in separate steps and specific gathers. In each gather, the CRS stacking operator is a two-parameter hyperbola. We determine two parameters in the CMP gather, two in the common-offset (CO) gather, and the last one in the CS gather (the second CS parameter is not independent).

The presented approach for the simulation of 2-D FO sections can be generalized to the 3-D case by performing the same hypothetical experiments. As for the ZO case, the propagation directions are then given by two component vectors, whereas the curvatures are symmetric 2×2 matrices. This yields a total of 13 wavefield attributes. The development of efficient strategies to determine these attributes remains as a future research topic.

As already indicated above, the CRS stack for FO simulation can also handle converted waves. In this case, the near-surface velocities at shot and receiver, v_S and v_G, refer to the respective wave types.

Conclusions

The CRS stack method, originally introduced for the simulation of 2-D ZO sections, has been generalized for the simulation of 3-D ZO sections as well as 2-D FO sections. For an efficient implementation, the 3-D ZO CRS stack can, e. g., be decomposed to separate 2-D ZO problems. An implementation strategy for the 2-D FO CRS stack was discussed. Its generalization to 3-D remains as subject for future research.

The data-driven simulation of FO sections opens up new possibilities for various applications. As an example, the FO CRS stack can be used to simulate a set of FO sections with high signal-to-noise ratio which are well suited as input for tomographic methods.

Acknowledgments

We would like to thank the sponsors of the Wave Inversion Technology Consortium for their support.

References

Jäger, R., Mann, J., Höcht, G., and Hubral, P., 2001, Common-reflection-surface stack: Image and attributes: Geophysics, **66**, no. 1, 97–109.

Mann, J., Jäger, R., Müller, T., Höcht, G., and Hubral, P., 1999, Common-reflection-surface stack - a real data example: J. Appl. Geoph., **42**, no. 3,4, 301–318.

Mann, J., 2001, Common-Reflection-Surface Stack and conflicting dips: 63th Mtg., Eur. Assoc. Expl. Geophys., Extended Abstracts.

Müller, T., Jäger, R., and Höcht, G., 1998, Common reflection surface stacking method - imaging with an unknown velocity model: 68th Annual Internat. Mtg., Soc. Expl. Geophys., Expanded Abstracts, 1764–1767.

Müller, T., 1998, Common Reflection Surface Stack versus NMO/STACK and NMO/DMO/STACK: 60th Annual Internat. Mtg., Eur. Assoc. Expl. Geophys., Extended Abstracts, Session 1-20.

Zhang, Y., Bergler, S., Tygel, M., and Hubral, P., 2000, Model-independent traveltime attributes for 2-D, finite-offset multi-coverage reflections: Accepted by Pure Appl. Geophys.

Offset-dependent resolution of seismic migration

Jörg Schleicher and Lúcio T. Santos, State University of Campinas

Summary

In this work, we study the resolving power of seismic migration as a function of source-receiver offset. We quantify horizontal resolution by means of the region around the migrated reflection point that is influenced by the migrated elementary wave. To obtain an estimate for the mentioned zone of *horizontal influence* after migration, we investigate the migration output at a chosen depth point in the vicinity of the specular reflection point, i.e., when the output point is moved along the reflector. The width of the spatial resolution resulting from migration of the reflection event is compared with the resolution predicted from theoretical ray-theory formulas for various data sets with different offsets. We find that the region of influence increases linearly with offset. In other words, the resolution power of seismic depth migration decreases when migrating data from larger offsets.

Introduction

Seismic resolution after depth migration has been theoretically discussed by various authors (Berkhout, 1984; Beylkin, 1985a; Cohen et al., 1986; Bleistein, 1987). A recent comprehensive study on the subject was carried out in Vermeer (1999), where additional references on the subject can be found.

It is widely accepted among geophysicists that "depth migration reduces the Fresnel zone." Although this is a very sloppy expression, because the Fresnel zone is a fixed-size frequency-dependent quantity associated with the reflected ray, we will see in this section that there is a lot of truth in it.

We discuss horizontal resolution in a completely analogous manner to the discussion of the pulse stretch in Tygel et al. (1994) that is closely related to vertical resolution. Note that we implicitly define now resolution in a slightly different way from what is usually done in the literature. Conventionally, resolution is quantified by the minimal distance of two objects such that their images can still be recognized as two distinct ones. In this way, resolution is clearly a frequency-domain concept. For a more practical, time-domain concept, we need a different definition. Guided by the above section on pulse distortion, we quantify horizontal resolution by means of the region around the migrated reflection point M_R that is influenced by the migrated elementary wave at M_R.

To obtain an estimate for the mentioned zone of "horizontal influence" after migration, we investigate the migration output at the chosen depth point $\overline{M}_R$ in the vicinity of the specular reflection point M_R (see Figure 1), i.e., when the output point is moved along the reflector Σ_R.

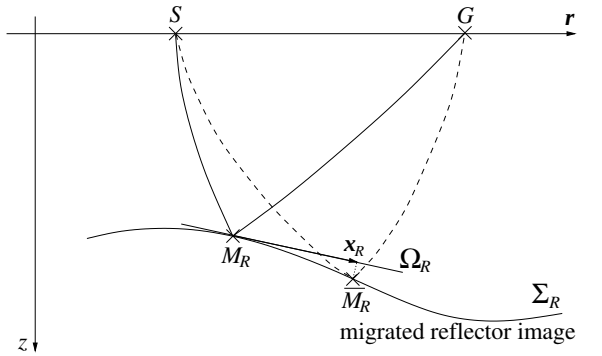

Fig. 1: Horizontal resolution: influence of the migrated event at the specular reflection point M_R on the migration result at the neighboring point $\overline{M}_R$ on the reflector.

In particular, we study the horizontal resolution of seismic migration as a function of offset. As shown by Tygel et al. (1994), the vertical resolution is the worse the greater the offset becomes. For a horizontal reflector below a constant-velocity overburden, it decreases proportionally to the cosine of the reflection angle. A similiar behavior is expected for horizontal resolution.

Theoretical background

As the starting point, we consider the time-dependent diffraction-stack integral in the form of Tygel et al. (1994). For an arbitrary depth point M, it reads

$$V(M,t) \;=\; \frac{-1}{2\pi}\iint d^2\boldsymbol{\xi}\; B(\boldsymbol{\xi},M)\;\partial_t F[]t+\mathcal{T}_{\rm dif}(\boldsymbol{\xi},M)], \tag{1}$$

where F is the seismic source pulse, B includes the weight function and the seismic data amplitude, and $\mathcal{T}_{\rm dif}(\boldsymbol{\xi},M)$ is the difference between the stacking surface, i.e., the diffration traveltime $\mathcal{T}_D(\boldsymbol{\xi},M)$, and the reflection traveltime $\mathcal{T}_R(\boldsymbol{\xi})$. The time derivative is needed to correctly recover the pulse shape. At an actual reflector point, M_R, the asymptotic evaluation of the above integral upon the use of the Method of Stationary Phase (Bleistein, 1984) yields in second-order approximation

$$V(M_R) \;\simeq\; F[0]\;\Upsilon(\boldsymbol{\xi}^*;M_R)\,, \tag{2}$$

where the new amplitude factor $\Upsilon(\boldsymbol{\xi}^*;M_R)$ includes the amplitude factor B of integral (1) together with some additional factors that appear as a consequence of the stationary-phase analysis. Moreover, $\boldsymbol{\xi}^*$ denotes the stationary or critical point.

To understand how the migrated result at M_R influences reflector points $\overline{M}_R$ in its vicinity, we calculate the derivative of the above stacking integral in equation (1) with respect to the horizontal coordinates $\mathbf{x}_R$ of $\overline{M}_R$. After application of the Method of Stationary phase to the resulting integral expression, we find for the migration result at $\overline{M}_R$

$$V(\overline{M}_R) = F[\frac{1}{2}\mathbf{x}_R \cdot \underset{\sim}{\mathbf{H}}_F \mathbf{x}_R]\Upsilon(\boldsymbol{\xi}, M_R)\,, \qquad (3)$$

where $\underset{\sim}{\mathbf{H}}_F$ is the Fresnel zone matrix as defined in Hubral et al. (1992). Observe that the amplitude factor $\Upsilon(\boldsymbol{\xi}, M_R)$ appearing in equation (3) is the one calculated at the central point M_R, not at $\overline{M}_R$.

The physical interpretation of this result is straightforward. Recall that $F[t]$ is a wavelet of finite length, i.e., it has values different from zero only inside the interval $0 \le t \le \mathcal{T}_\varepsilon$, where $\mathcal{T}_\varepsilon$ is the pulse length. Thus, the influence of the migrated wavefield at M_R ends at that particular point $\overline{M}_R$, where

$$\frac{1}{2}\mathbf{x}_R \cdot \underset{\sim}{\mathbf{H}}_F \mathbf{x}_R = \mathcal{T}_\varepsilon\,. \qquad (4)$$

This is exactly the definition of the time-domain Fresnel zone (Hubral et al., 1992). Thus, the area affecting the reflected field in the vicinity of M_R is the area of the time-domain Fresnel zone at M_R.

Let us appreciate the meaning of this result. We know that forward wave propagation distributes the information scattered from each "diffraction point" M in the seismic data over one projected Fresnel zone, which is therefore the minimum aperture for seismic Kirchhoff prestack depth migration (Schleicher et al., 1997). The present result tells us that Kirchhoff depth migration smears the information pertaining to each depth point M in the migrated section over its time-domain Fresnel zone. This is exactly what should be needed to undo the effects of wave propagation, that is, to recover the migrated image with a perfect resolution.

Since the migration operator is proven to be valid in paraxial approximation, i.e., up to second order, we might expect that the migrated data will show a residual uncertainty in lateral resolution that is roughly equivalent to the quality of the paraxial approximation of the Fresnel zone. In the next section, we investigate this expectation with a simple numerical experiment.

Synthetic example

To demonstrate the lateral resolution of seismic Kirchhoff depth migration, we have devised the following simple numerical experiment. Consider a horizontal interface below a homogeneous halfspace with an acoustic wave velocity of 6 km/s (see Figure 2). Below the interface, we consider a vertical fault at $x = 0$ km, separating two homogeneous blocks with velocities of 5 km/s and 5.5 km/s on the left and right side of the fault, respectively. In this

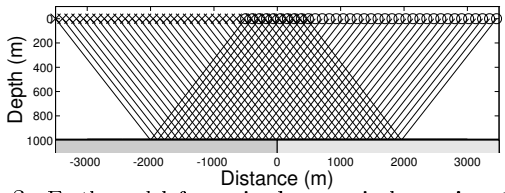

Fig. 2: Earth model for a simple numerical experiment. Also shown is the ray family for a common-offset experiment with a source-receiver offset of 3000 m.

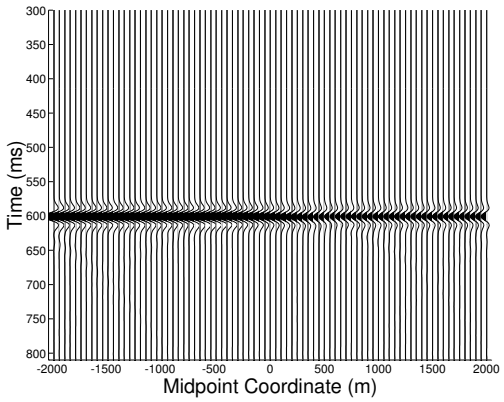

Fig. 3: A numerically simulated common-offset dataset for the model in Figure 2.

model, we have simulated an ensemble of common-offset seismic surveys with source-receiver offsets ranging from 0 m to 4000 m. The reflection angle for the largest offset is about 68°. A typical common-offset dataset (for a source-receiver offset of 3000 m) is depicted in Figure 3. The numerical modeling was realized by an implementation of the 2.5-dimensional Kirchhoff integral. The source wavelet is a symmetrical Ricker wavelet with a duration of 64 ms.

The model was chosen to demonstrate the capacity of Kirchhoff migration to collapse the Fresnel zone. The simple fault model is ideal for this demonstration as it allows for a quantitative estimate of the residual Fresnel zone after migration. The Kirchhoff data show how the information of the fault is distributed in the seismic amplitudes over a projected Fresnel zone. To make this even more evident, we have picked the peak amplitude along the seismic event in Figure 3. This amplitude is shown in Figure 4 as a function of midpoint coordinate. Also indicated in Figure 4 are the boundaries of the time-domain projected Fresnel zone. For a common-offset experiment over a model with a horizontal reflector below an overburden with a constant velocity v, the projected Fresnel zone is an ellipse with semi-axes

$$b = \sqrt{v\mathcal{T}_\varepsilon z}\,, \qquad a = \frac{b}{\cos^{3/2}\alpha_R}\,, \qquad (5)$$

where $\mathcal{T}_\varepsilon$ is the length of the source wavelet, z is the reflector depth and α_R is the reflection angle. Indicated in

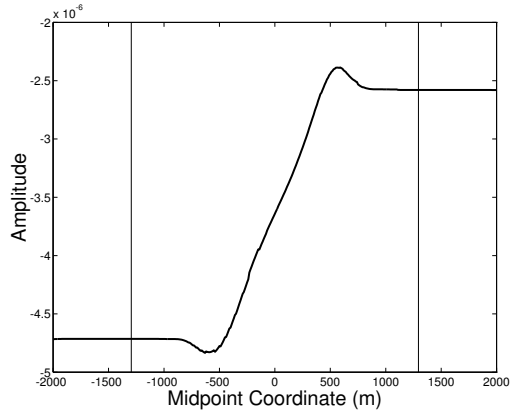

Fig. 4: Seismic peak amplitude along the reflection event in Figure 3. Also indicated are the boundaries of the time-domain projected Fresnel zone in the direction of the seismic line.

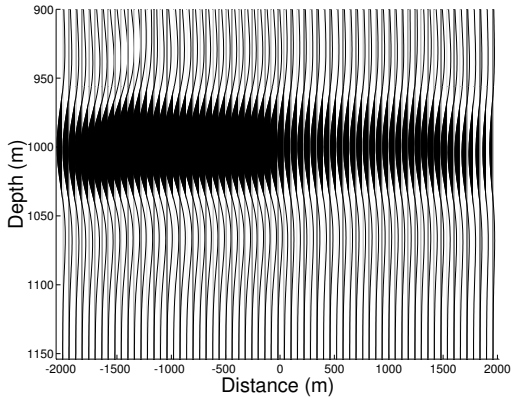

Fig. 5: Depth section after a true-amplitude Kirchhoff migration of the data in Figure 3.

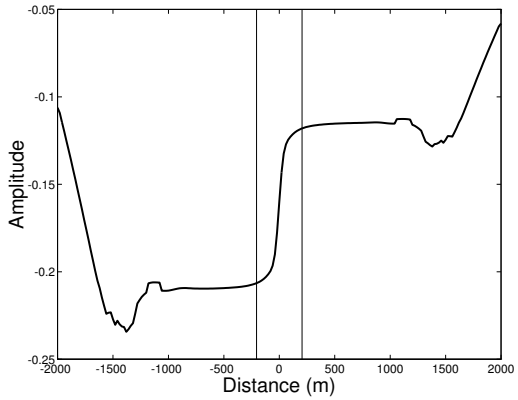

Fig. 6: Picked peak amplitudes of the migrated reflection event in Figure 5.

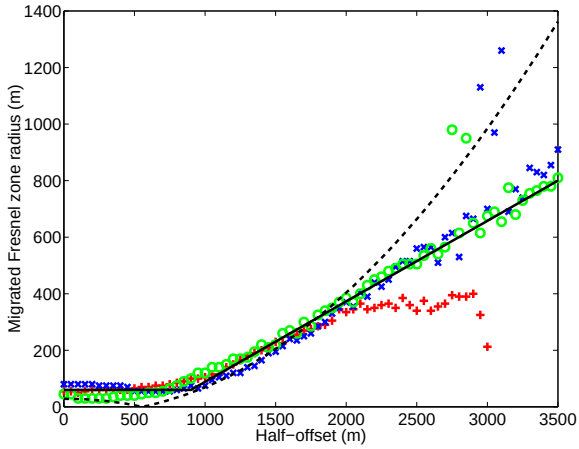

Fig. 7: Residual Fresnel zone after Kirchhoff depth migration. Estimated values (crosses, plus signs, and circles) vs. predicted size (solid and dashed lines).

Figure 4 is the size of the greater semi-axis a that quantifies the extension of the Fresnel zone in the direction of the seismic line. In Figure 4, we observe that the abrupt horizontal velocity contrast leads to a smooth amplitude increase along the seismic reflection event, almost covering a complete projected Fresnel zone. Note that for a good estimate of the transition zone, $\mathcal{T}_\varepsilon$ is *not* the full length of the seismic wavelet but an *effective* length being the mean half-period of the wavelet.

Figure 5 shows the data of Figure 3 after application of a seismic prestack Kirchhoff depth migration. The same prestack depth migration has been performed on all other corresponding synthetic common-offset sections with source-receiver offsets between 0 m and 4000 m. The results of these migrations are similar to that of Figure 5 and are, thus, not depicted here. We already recognize in Figure 5 that the amplitude change from one side of the fault to the other has become much steeper than in the original data (cf. Figure 3). This comes as no surprise since it is well-known that migration increases the lateral resolution. To better quantify this effect, Figure 6 shows the picked peak amplitudes along the seismic event in Figure 5. In this figure, it is much easier to observe than in Figure 5 that the change in amplitudes between the two values of the reflection coefficient at both sides of the fault is much more abrupt than in Figure 4. The Fresnel zone has indeed been strongly reduced by Kirchhoff migration. Our estimate for the size of the residual Fresnel zone after migration is indicated by two vertical bars.

To put this investigation on a broader basis and make its results more conclusive, we have repeated this numerical comparison for the other source-receiver offsets between 0 m and 7000 m. Figure 7 shows the size of the residual Fresnel zone after migration as a function of offset (crosses, plus signs, and circles). The size of the residual Fresnel zone after migration was estimated by determining where the amplitude values in the transition zone reach the value of the reflection coefficient as recovered by the true-amplitude migration. Because of the numerical error, this cannot be used as an exact criterion. We there-

fore chose the value of the recovered reflection coefficient to be reached where the error was less than five percent. Figure 7 compares the size of the residual Fresnel zone as estimated in this way to its expected size (dashed line) as calculated by the difference of the paraxial and true time-domain Fresnel zones. We observe a good agreement of estimated and expected values over up to a half-offset of 2000 m. The larger offsets, however, show that this expectation overestimates the residual Fresnel zone after migration. A heuristical curve (bold line) that increases linearly with offset better follows the observed values over the whole range of half-offsets.

Note that the size of the migration aperture also affects resolution. The crosses in Figure 7 were obtained for a smaller migration aperture. For half-offsets beyond 2000 m, they do not represent a realistic measure of the achieved resolution. Here, the boundary effects reach into the transition zone. As a consequence, the migration amplitudes never reach the true value, that is, the correct reflection coefficient.

By means of the present analysis, we have now gained a much more quantitative understanding of what the common expression "depth migration reduces the Fresnel zone" means in quantitative terms. It is to be remarked, however, that the above resolution is reached only with perfect, that is, noise-free, correctly sampled, unbiased data that were acquired with short intervals between two adjacent shots and receivers. Any additional distortion due to the wave propagation in an inhomogeneous reflector overburden, such as transmission losses, focusing and defocusing, caustics, etc., as well as acquisition effects such as irregular source and receiver spacing, source and receiver coupling, uncalibrated traces, etc., will not only affect the recovery of the best possible amplitudes but will also degrade the seismic resolution.

Final remarks

In this paper, we have discussed the horizontal resolution of true-amplitude Kirchhoff depth migration in dependence on the source-receiver offset. We have seen that the region around the reflection point affected by the reflected wavefield after migration increases with offset. This means that the resolving power of seismic migration decreases with increasing offset. A possible explanation of this behavior is that Kirchhoff migration is an algorithm that is based on a second-order approximation. Therefore, it can be expected to be correct only up to second order. However, this expectation explains the observed resolution only for a certain range of offsets.

Qualitatively, we observe the expected behavior of a decreasing horizontal resolving power with increasing offset. However, the quantitative behavior of horizontal resolution as a function of offset is different from that of vertical resolution. As shown by Tygel et al. (1994), for constant velocity and a horizontal reflector, the vertical resolution decreases proportionally to the cosine of the reflection angle. Horizontal resolving power, however, seems not to be a simple function of that angle. The best fitting curve increases linearly with offset.

Note that a decreasing resolution with increasing offset may have consequences for a post-migration stack and for AVO analysis. The image after a post-migration stack can only be expected to exhibit the worst resolution of the individual images, i.e., that of the largest offset to be used in the stack. An AVO analysis may be affected when studying the AVO trend too close to an amplitude contrast along a reflector. Because of different resolution, amplitude might be correct for smaller offsets but wrong for larger offsets.

Acknowledgements

The research of this paper was supported in part by the National Research Council (CNPq – Brazil), the São Paulo State Research Foundation (FAPESP – Brazil), and the sponsors of the WIT Consortium.

References

Berkhout, A., 1984, Seismic resolution, a quantitative analysis of resolving power of acoustical echo techniques: Geophysical Press.

Beylkin, G., 1985a, Imaging of discontinuities in the inverse scattering problem by inversion of a generalized Radon transform: Journal of Mathematical Physics, **26**, no. 1, 99–108.

Bleistein, N., 1984, Mathematical methods for wave phenomena: Academic Press, New York.

Bleistein, N., 1987, On the imaging of reflectors in the earth: Geophysics, **52**, no. 7, 931–942.

Cohen, J., Hagin, F., and Bleistein, N., 1986, Three-dimensional Born inversion with an arbitrary reference: Geophysics, **51**, no. 8, 1552–1558.

Hubral, P., Schleicher, J., and Tygel, M., 1992, Three-dimensional paraxial ray properties – Part I. Basic relations: Journal of Seismic Exploration, **1**, no. 3, 265–279.

Schleicher, J., Hubral, P., Tygel, M., and Jaya, M., 1997, Minimum apertures and Fresnel zones in migration and demigration: Geophysics, **62**, no. 2, 183–194.

Tygel, M., Schleicher, J., and Hubral, P., 1994, Pulse distortion in depth migration: Geophysics, **59**, no. 10, 1561–1569.

Vermeer, G., 1999, Factors affection spatial resolution: Geophysics, **64**, no. 3, 942–953.

Practical implementation of the Wave Analog of Common Depth Point Method

Andrey N. Kremlev, Russian Academy of Sciences, Novosibirsk, Russia,
Viatcheslav I. Priimenko, Sérgio A.M. Oliveira and Roseane M. Misságia,
Lenep/Uenf, Macaé, Brazil

Abstract

Development and application of the inverse scattering problems of acoustic and seismic waves for seismic data processing and investigation of sedimentary cover is an actual and perspective tendency. In this report we describe practical realization of the Wave Analog of Common Depth Point Method (WCDP) for 2D seismic data processing and represent its testing on synthetic data corresponded to typical geological objects: dipping reflectors, diffraction points and salt dome tectonic model.

Introduction

The WCDP method is a method for multi channel seismic data processing. Among migration methods on unstacked data the WCDP method stands out by the fact that it is based on the strict solution (in linear approximation) of inverse acoustic scattering problem using overdetermined multifold data, A.N.Kremlev (1979, 1985). This problem consists for 2D case in reconstruction of function $a(\vec{\rho})$ describing medium inhomogeneities by wave field $u(x, x_0, t)$ registered for different source (x_0) and receiver (x) positions on free surface. This wave field satisfies to the following Cauchy problem, Bleisten (1979):

$$\frac{\partial^2 u}{\partial t^2} = c^2(1 + a(\vec{\rho}))\nabla^2 u + \delta(t)\delta(\vec{\rho} - \vec{\rho_0}), \qquad (1)$$
$$u|_{t<0} \equiv 0,$$

where c is the velocity of acoustic waves in background medium and $(\vec{\rho}, \vec{\rho_0}, t) \in R^2 \times R^2 \times R, \vec{\rho} = (x,z)$, $\vec{\rho}_0 = (x_0,z_0)$. The result of the inverse scattering problem solution for Cauchy problem (1) is linear focusing operator:

$$\alpha(\vec{\rho}) = \int \frac{d\omega}{2\pi}\frac{d\chi}{2\pi}\frac{d\chi_0}{2\pi}\Phi_v(\vec{\rho}, \chi, \chi_0\omega)\hat{u}(\chi, \chi_0\omega), \qquad (2)$$

which allows to calculate vizualization function $\alpha(\vec{\rho})$ averaged over domain with size determined by the signal wave length. In formula (2) function $\hat{u}(\chi, \chi_0, \omega)$ is the spectrum of observed field,

$$\Phi_v(\vec{\rho}, \chi, \chi_0\omega) = \Theta(\frac{\omega^2}{v^2} - \chi^2)\Theta(\frac{\omega^2}{v^2} - \chi_0^2) \qquad (3)$$
$$\frac{v}{\omega}\cdot\sqrt{\frac{\omega^2}{v^2} + \chi_0\chi + \sqrt{\frac{\omega^2}{v^2} - \chi^2}\cdot\sqrt{\frac{\omega^2}{v^2} - \chi_0^2}}$$
$$\cdot exp\{i(\chi + \chi_0)x - iz(\sqrt{\frac{\omega^2}{v^2} - \chi^2} + \sqrt{\frac{\omega^2}{v^2} - \chi_0^2})\}$$

is the kernel of focusing operator (3). Here $\Theta(\cdot)$ is Heaviside's function and v is apriory input wave velocity. Exponential factor in (3) describes phase shift migration of source and receiver coordinates analogous to Gazdag (1978) and Stolt (1978) migration, but proceedings multipliers are the result of strict inverse problems solution. It is necessary to note that stacking formula (2) uses input data overdetermination completely, like the CDP method, and realizes useful signal accumulation. It increases signal/noise ratio in obtained stack and can be used for velocity analysis too.

Practical implementation of the WCDP method

For practical realization of the WCDP algorithm we use transform in (2) from the coordinates "source-receiver" to the coordinates "common midle point- offset" by the formulae:

$$m = (x + x_0)/2, \quad l = x - x_0. \qquad (4)$$

In (x, x_0) coordinates aperture used for approximates calculation of the vizualiztion function $\alpha(\vec{\rho})$ is square ABCD situated on general seismic plane, (see Fig. 1), with diagonal AC oriented along CMP m-axes. In this case of increasing of investigion depth and inclination angles of reflected boundaries it is necessary to increase summation base, too: $AC \rightarrow AC_2$. As it seesig from 1, the number of seismic traces involved simuleneously in data processing increases quadratically. Furthermore, domais (as triangles ABK_2 and DLD_2) appear which don't have real seismic data and which we need to fill by zero's traces for FFT implementation. This step has artificial character and does

not increase infomativity of profile. In (m,l) coordinate aperture A'B'C'D' is rectangle one and volume of calculation increases linearly under increasing of summation base. Taking into account (4) and making the change

$$q = v(\sqrt{\frac{\omega^2}{v^2} - \chi^2} + \sqrt{\frac{\omega^2}{v^2} - \chi_0^2})$$

we obtain final stacking formula

$$\alpha_v(m,t) = \int_{-\infty}^{\infty} \frac{dq}{2\pi} e^{-iqt} \int_{-\infty}^{\infty} \frac{d\mu}{2\pi} e^{i\mu m} \int_{-\infty}^{\infty} \frac{d\nu}{2\pi} \hat{\Phi}_v(m,t,\mu,\nu,q) U(\mu,\nu,q), \quad (5)$$

where integrals with respect to variables q and μ are Fourier integrals which can be calculated by FFT algorithm. Here $\hat{\Phi}_v(\cdot)$ and $U(\cdot)$ are the kernel of focusing operator and the wave field spectrum in new coordinates, correspondengly. Outline, also, that computations in stacking formula (5) for finite aperture increase linearly with stacking base increasing with constant offset range. It is very important for reconstruction of inclined deep reflectors.

Reconstruction of typical geological objects

Fig.2 shows the result of pointwise reflectors reconstruction disposed on different depth and different parts of summation base. We can see good quality of such subjects reconstruction and, it's worth to note, the precise of diffractors reconstruction is closed to its theoretical wave length limit. Figs.3 and 4 show the results of dipping reflectors reconstruction in the case when (a) background velocity used in the inversion, coincides with the real wave velocity c of the medium and for the case when (b) these velocities differ one from another on 25%. Note that for the case (b) inclined reflectors are reconstructed stably inspite of big velocity difference, though they move a little from their real positions.

Salt dome structure reconstruction

A model of salt-diaper structure is shown on Fig.5.That model is highly representative for Campos Basin (Atlantic Ocean, Campos Offshore Deep Water). The synthetic data were calculated by numerical solution of the acoustic wave equation using finite-diffrence approach, acording to algoritm proposed by Oliveira (1999), which considered both variations in velocity and density of medium. The data consists of 521 shot gathers spaced by 30m for 96 receivers spaced with same distance. Fig.6 and Fig.7 show the results of the model reconstruction with background velocity 1500m/s and 1600m/s. All reflectors, including dipping reflectors and undersalt interface are good rebuild though the last one move away from their real positions due to strong lateral velocity variations. We can see some noise in the data due the presence of multiples, spetially the water botton multiple. This indicate the necessity of demultipling the data previous to WCDP processing. Finally, it is important to mention that the CPU time required by WCDP is comparable to the Stolt prestack algorithm.

Acnowledgements

We would like to thank CENPES-PETROBRAS for permission to use the synthetic model with salt dome structure. We are grateful to Prof. Djalma S. Filho for useful discussions during the course of this work supported by FINEP-CTPETRO, grant n.0810/00.

References

A.N.Kremlev, 1979, Technical Report of Computing Center of Siberian Branch of Russian Academy of Sciences: Novosibirsk, Russia.

A.N.Kremlev, 1985, Wave Analogue of the Common Depth Point Method: Geologia i Geofizika, **26**, no. 10, 77–86.

BleistenN., C. J., 1979, Velocity Inversion Procedure for Acustic Waves: Geophysics, **44**, 1077–1087.

Gazdag, I., 1978, Wave Equation Migration with the Phase Method: Geophysics, **46**, 1342–1351.

Oliveira, S. A. M., 1999, Um Algoritmo Prático de Modelagem 3D baseado na Solução da Equação Acústica completa da Onda: Abstract Expanded, 6th International Congress of SBGF.

Stolt, R. H., 1978, Migration by Fourier Transform: Geophysics, **43**, 23–48.

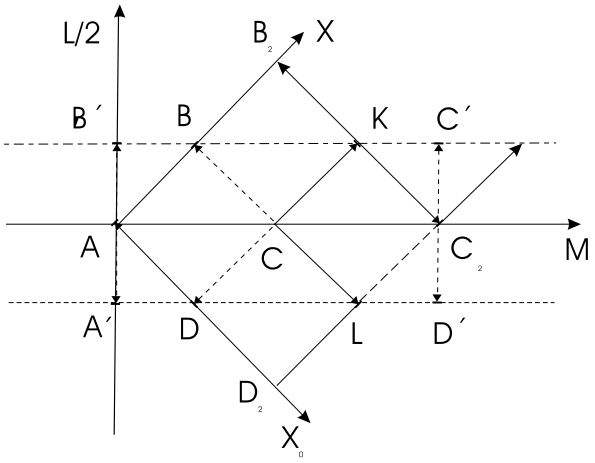

Figure 1: WCDP aperture on general seismic plane

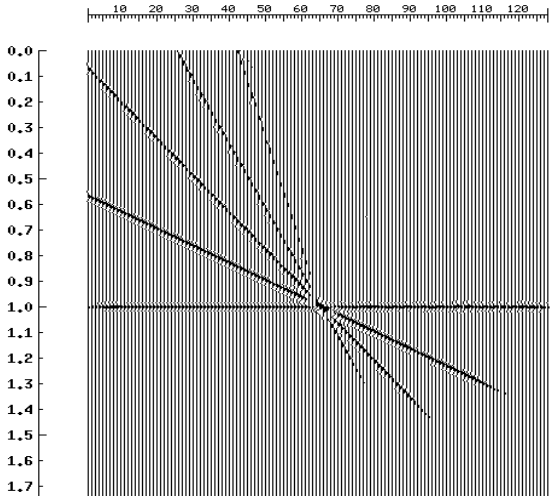

Figure 3: Reconstruction of deep oriented planes. Angles 0,15,30,45 and 60 degries. $V_{media} = V_{input} = 2000m/s$

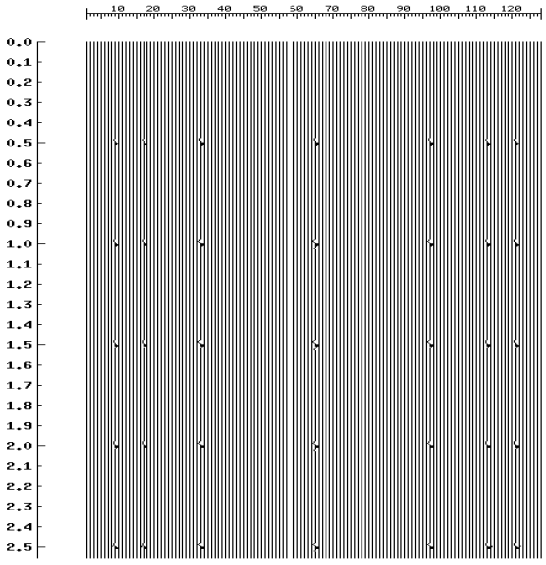

Figure 2: Reconstruction of point difractors.

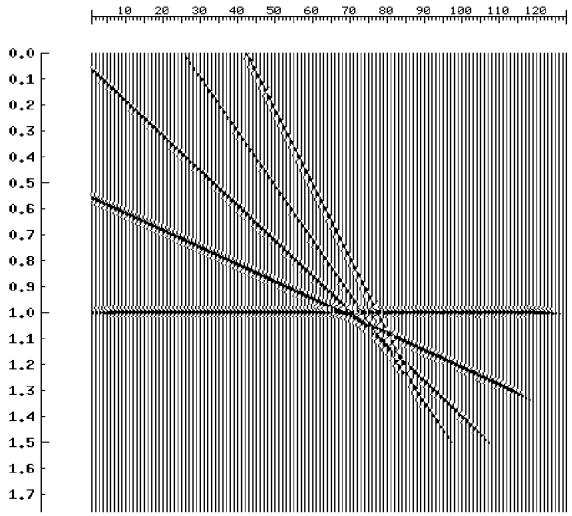

Figure 4: Reconstruction of dipped planes. Angles 0,15,30,45 and 60 degries. $V_{media} = 2000m/s$, $V_{input} = 1500m/s$

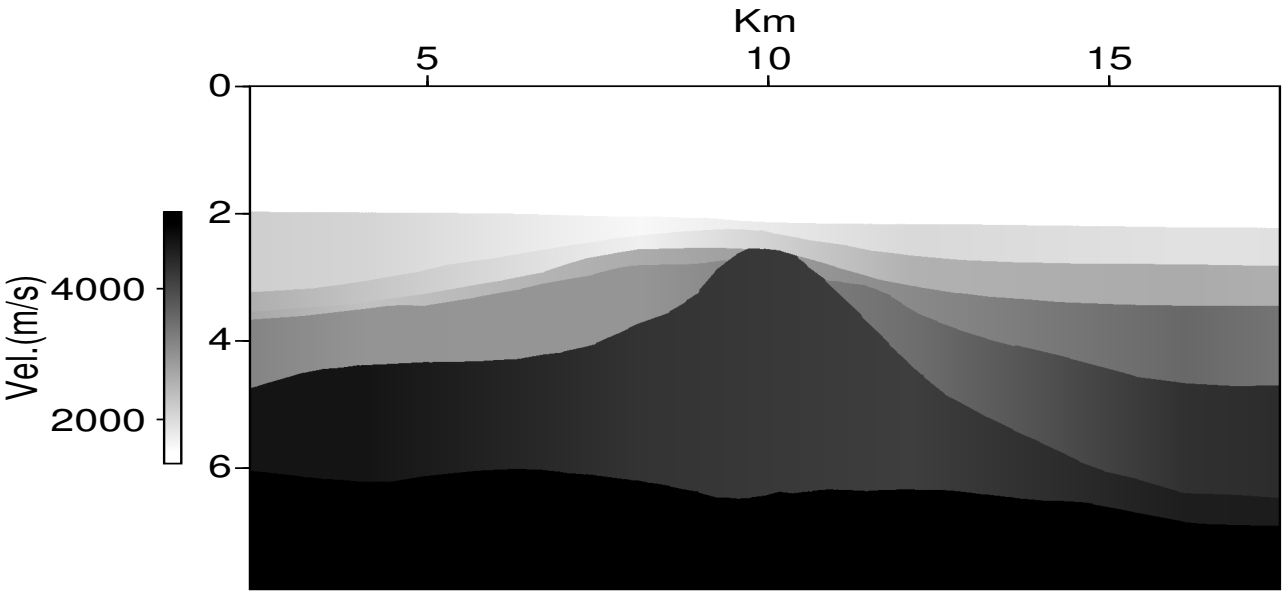

Figure 5: A model of salt-diaper structure.

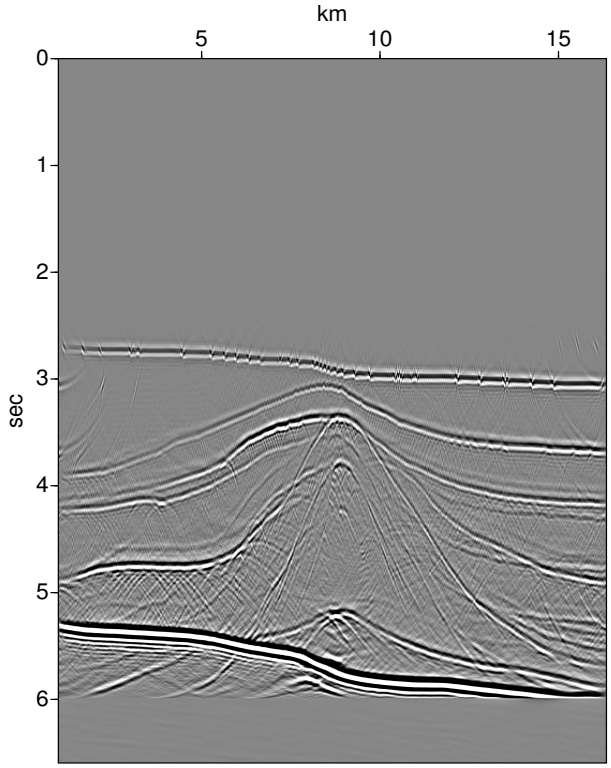

Figure 6: WCDP result, $V_{input} = 1500m/s$.

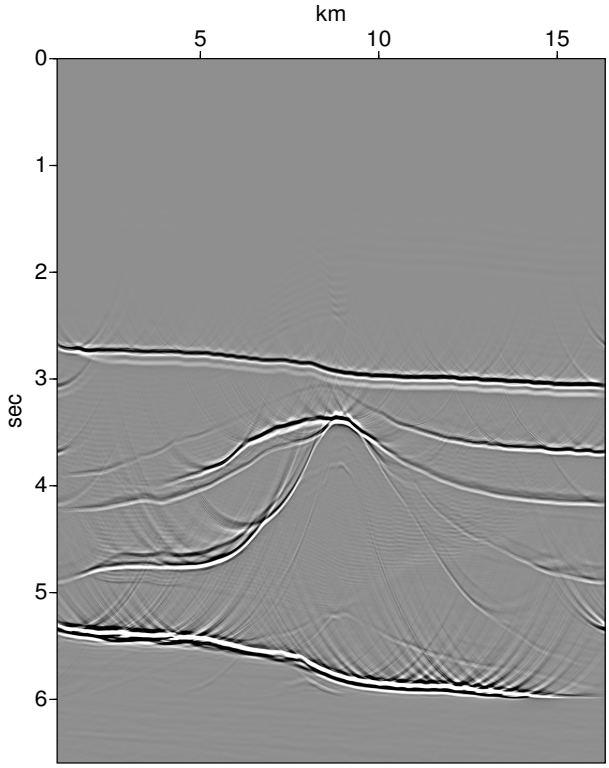

Figure 7: WCDP result, $V_{input} = 1600m/s$.

Prestack depth imaging and its application to Brazilian data

Robert Bloor, Alberto Galleguillos and Peter Watterson, WesternGeco, robert.bloor@westerngeco.com.
Roberto Fainstein, Schlumberger, Rio de Janeiro.

Abstract

The use of prestack depth imaging has been expanding rapidly over the past few years. During this time we have seen a dramatic evolution of the technology and methods involved. This development continues today and depth imaging methods and practices will evolve further over the coming years. The majority of the prestack depth migrations done during this period have been in the Gulf of Mexico and the North Sea. Our intent in this paper is to review the history of prestack depth migration and then consider the lessons learnt along the way. We will examine how to make the most of this experience as we consider each new prestack depth migration project. To do this we will focus more on some of the components of prestack depth migration such as the velocity model building and the migration algorithms. We will then consider the above in the context of the various exploration areas in and offshore Brazil.

Introduction

An understanding of prestack depth migration has been available since the 1970's. It was considerably more recent before the use of prestack depth migration became common. Since depth migration began to be an accepted method the quantity of prestack depth has grown dramatically. The majority of prestack depth migration experience is centred on certain areas and within these areas despite the level of experience, depth imaging is still an immature technology.

In areas where there is less experience and exposure to these technologies, it is beneficial to draw on appropriate experience from other areas. This is one of the themes of our paper. We must stress "appropriate" and this leads us to an analysis of how one would define which methods and from where will best contibute to new projects.

To understand these factors we can consider the reasons for doing prestack depth imaging and the requirements for prestack depth imaging. Armed with this knowledge we can start to identify similarities in velocity model building requirements and in migration algorithm requirements from one area to another. Generally these similarities will be related to the geology, but the geologies from one area to another are never identical. For example, a steeply dipping salt flank near the surface may impose different demands on the velocity model building and migration algorithms than a deeper salt flank, especially as the overburden changes in each case.

Finally we will consider some of the specifics of the current and potential areas for prestack depth imaging in Brazil. Particularly where depth imaging can potentially improve the imaging of the subsurface, and from where we can draw experience to help this work.

Why do prestack depth migration?

Depth migration has the ability to better image data in the presence of lateral velocity variations. Prestack depth migration can improve the image quality when alternative stacking methods (DMO, prestack time based methods etc.) can not perfectly stack the data. Virtually every seismic survey contains lateral velocity variations to some extent. The obvious question is not "why do we do prestack depth migration", but "why don't we always do prestack depth migration".

Why don't we always do prestack depth migration?

A theoretically preferable imaging method can only be justified if the lift in quality and accuracy will change the decisions based on the final product enough to justify the additional effort. Our main concern here is to answer this question from the technical point of view. However, we cannot ignore some practicalities that will often be the reasons for not pursuing prestack depth migration. These factors are essentially cost and time. Prestack depth migration requires a velocity model, which takes time to produce and prestack depth migration is itself a relatively time consuming process (compared to time processing). The extra time and the additional computational effort correspond to additional cost.

In addition to the practical aspects of the additional time taken to build a velocity model, there is the question of accuracy of the velocity model. Optimum prestack depth migration results require a perfect velocity model. If we cannot produce a perfect velocity model then the advantages depth migration has over conventional processing is reduced. In reality this means there is a point where even with some level of lateral velocity variation time migrations can produce an image which is

comparable to the prestack depth images. Typically, the differences will increase as the amount of lateral velocity variation increases. Simply because larger lateral velocity variations exist, we should not assume they will be represented in the velocity model accurately enough to produce the expected improvement. There have been examples where prestack depth migration has been inferior to time products. This should never happen, but it can if large velocity variations are put in the model incorrectly. If a variation cannot be identified accurately a smoother version of that variation should be in the model and this will tend to lead the results towards those of the time migration. If the variation is accurately defined results should be superior to the time migration.

We can now see a set of guidelines are starting to appear to govern the choice of imaging approaches. Lateral velocity variations have to reach a certain level to justify depth imaging. Once we have lateral variations we have to recover them adequately in the velocity model. To develop these guidelines we should consider some of the different varieties of lateral velocity variations that we encounter.

Prestack depth imaging and lateral velocity variations

Lateral velocity variations come in many categories. It is instructive to divide these categories into relatively few, ranging from abrupt and significant lateral changes to slowly varying lateral variations. For example we can consider lateral variations which are due to an abrupt change in velocity such as a salt boundary or fault. Lateral variations which are due to boundaries between dipping layers such as a dipping water bottom. Lateral velocity variations that are due to gradual changes in properties, for example gradual changes in lithology. There are geological situations that can have any of these characteristics such as gas clouds. If the nature of all lateral velocity variations in an area can be defined the chances of successful imaging increase dramatically. When these variations are difficult to define, it will be difficult to get a good image of the energy propagating through these areas of velocity uncertainty. Velocity boundaries that are difficult to interpret or gradual velocity changes which must be recovered from velocity analysis methods will be difficult. Velocity variations that can be accurately defined via interpretation are much more reliable.

In the Gulf of Mexico the dominant cause of lateral velocity variation is the salt. If the salt boundary is readily interpreted then depth imaging should start to be superior to time imaging. This is why there are a large number of examples from the Gulf of Mexico showing depth imaging improving the image. However, to achieve better images of the deeper structure, especially where the salt becomes more complicated involves a number of additional considerations (O' Hara et al., 2000). Particularly, the migration algorithm must be adequate for the demands of this environment. The apertures required to image this data are extremely large. We should not forget that not all algorithms are able to be extended to these apertures and produce good results.

In environments where there are a larger number of factors affecting the velocity variations then the process becomes more difficult. For example, if we have gradual lateral velocity variations above an abrupt variation, both of these issues must be dealt with. This is a common scenario in the North Sea. Two aspects of model building become critical: the tools we use and the way we use them. Different tools are more efficient and more accurate in different situations. Often we see practitioners using the same tools regardless of the data they are working on. This restriction may be enforced by the range of reliable tools at their disposal, but this restriction will also compromise their abililty to handle the range of geological situations that exist. If we approach every project with the full set of available methods rather than some predetermined subset the probablility of building an adequate velocity model significantly improves.

When we are assessing these problems the most reliable indicators of problems are the data. Lateral velocity variations will start to produce inconsistencies in the time imaged seismic data which can often be recognised and used to determine a model building approach. In addition we would want to understand the geological context of an area to assess as many factors that can play a role in the model building as possible. One factor that is often encountered is anisotropy.

Anisotropy

Anisotropy is present in the majority of the rocks we image through. Particularly offshore Brazil there is a lot of evidence for significant anisotropic behaviour. Figures 1 shows a CMP gather from the Santos basin. This gather has had NMO applied on the basis of the hyperbolic moveout equation. The near offsets are nicely flattened and we can see that no single vleocity will flatten the whole gather. As soon as we flatten

higher offsets the near offsets would be undercorrected. There are a number of factors which can cause this phenomenon. The location in this case was chosen to try and avoid dip, crossline dip, lateral velocity varions etc. Vertical variations will be present and figure 2 shows a gather with a 4 term moveout applied. This is designed to take account of the issues of the vertical variation in velocity. The vertical variation induces bending of the raypath. The gather is better corrected than figure 1 but there is still moveout at the high offset which cannot be removed by this method. Assuming this isa reflection, and the other possible complications are not present, that leaves anisotropy. The fact that we can see similar behaviour from top to bottom of the gather we are showing reduces the chances of it being due to any other affects. Figure 3 shows the gather with anisotropic moveout applied, the gather can now be flattened across the entire offset range.
This sequence of dealing with vertical variations and anisotropy is common throughout at least the Santos and Campos basins.

The above approach is appropriate to optimally stack the data during time processing. However, it does not fully correct for overburden propagation effects as we must do for depth imaging. As we move into more complex territory the anisotropy is still present and even if the targets are below the regions of anisotropic behaviour, energy must propagate throught the overburden to reach the targets. In this scenario the prestack depth imaging approach should account for anisotropy. Here we can draw on experience, from elsewhere in the world , in anisotropic model building and anisotropic prestack depth migration (Bloor et al, 2000).

Depth imaging in Brazil

Brazil has a large number of prospective offshore basins. Each of these basins pose different seismic imaging problems. Some of these problems are clearly depth imaging related as in the basins off eastern Brazil whilst others are less obvious such as in the basins offshore north Brazil.

Massive salt is present in the eastern Brazilian basins. In the Santos and Campos basins there are a range of salt related problems to be solved by depth imaging. Superficially these basins appear to have a lot of similarities to the Gulf of Mexico. The overburden above the autocthonous Brazilian salt contains various calcareous layers and sometimes lava intrusions. The best prospects of Campos basins are on turbidites of the Upper Cretaceous and Tertiary, these are generally situated on salt related structures. These basins are also the ones in which we have the best evidence for anisotropy. Accurate definition of the turbidites would benefit from the use of anisotropic imaging.

Eocene lava flows became pervasive in the northern Espirito Santo Basin, here the main problems are related both with the lava, imaging of salt structures and with identifying sub-basalt features. The most relevant area from the rest of the world is probably the Faeroes where similar basalts exist. Whilst depth imaging is still required, multiples and noise attenuation are significant problems and a large portion of the effort will be dedicated to dealing with these.

Offshore Bahia, in the Camamu-Almada basin, the imaging problems both on the shelf and in the slope are connected with the correct understanding of the rift geometry and prospects within it. Depth imaging can more accurately define the faulting beneath the lateral velocity variaitons of the overburden.

Moving to Sergipe-Alagoas there are evaporites and carbonates with fault blocks beneath them. These have some similarities to parts of the North Sea. Prospects need to be depth imaged in the faulted syn-rift as well as in the overburden.

The rift section offshore north Brazil is characterized by block-faulting that are related to the geometry of the equatorial fracture zones. The most interesting area for depth imaging is the Amazon Cone where as result of thick Miocene and Pliocene sedimentation, shale diapirs have formed. The lateral velocity variations induced by the diapirism and overpressure zones around the diapirs pose a depth imaging problem. Hydrocarbon prospects are situated around the diapirs.

Summary

Depth imaging is still a developing field. Whilst there is a lot of experience around the world, new projects often require modifications to existing approaches. To produce good depth migration results we need to draw upon appropriate experience, use the most appropriate tools and acknowledge the fact that we are working with a new dataset and it will be different to previous projects. Given these prerequisites depth imaging is capable of giving improved results and has the best chance of fulfilling the objectives of the project.

Prestack depth imaging

Depth imaging in Brazil is necessary for the appropriate understanding of the syn-rift geometry and for the correct structural and stratigraphic mapping of carbonates, autocthonous salt and shale diapirs. In addition, it adds to the high-resolution imaging of turbidite reservoirs.

Bibliography

Bloor, R., Whitfield, P., Fisk, K., 2000, Anisotropic depth imaging and model building, Petex 2000, London
O'Hara, P., Kapoor, J., Liu, C., Trares, S., 2000, Imaging the unimaginable. SEG 2000, Calgary.

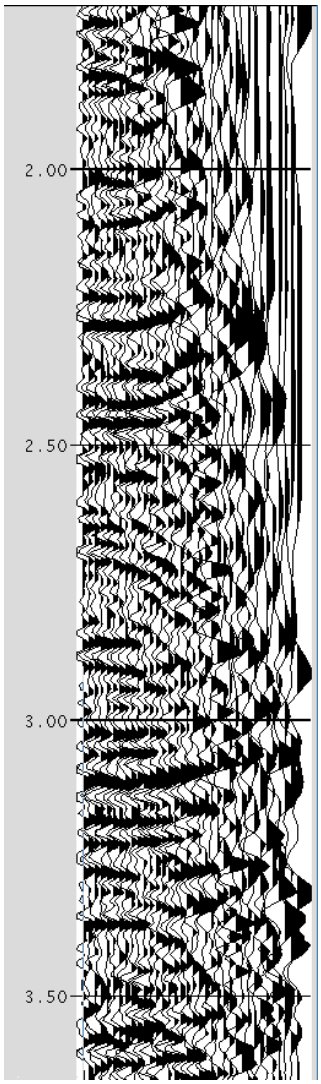

Figure 1: Hyperbolic moveout correction.

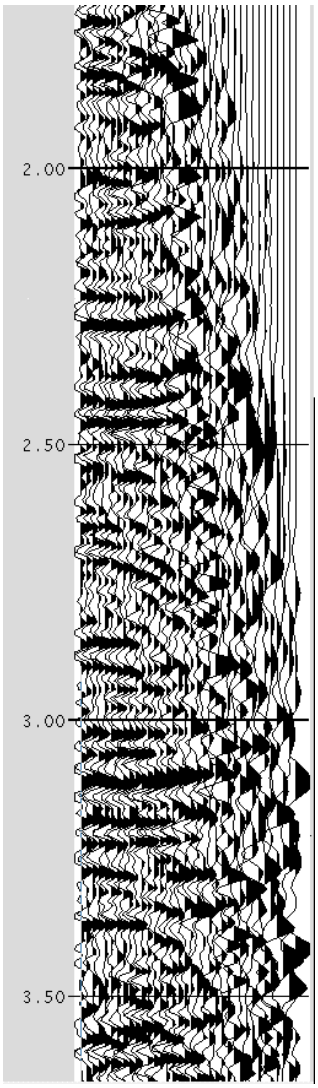

Figure 2: 4 term moveout correction.

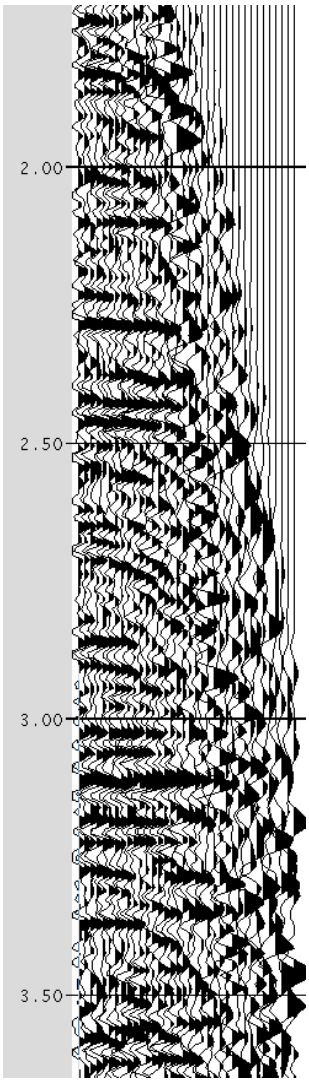

Figure 3: Anisotropic moveout correction.

Recuperação de Atributos Sísmicos Utilizando a Migração para Afastamento Nulo

Angela C. R.Vasquez (*), Adelson S. Oliveira (**) Martin Tygel (***) & Lúcio T. Santos (***)

INTRODUÇÃO

De especial interesse é a determinação de propriedades de rocha e fluido pelos métodos geofísicos envolvendo a propagação de ondas sísmicas em poços (perfis) ou em subsuperfície (métodos sísmicos). Na sísmica o objetivo central é obter uma imagem realista dos refletores de interesse e também inverter os dados registrados para atributos sísmicos que melhor caracterizem os meios geológicos nos quais inserem-se os refletores. Dentre os algoritmos de imageamento sísmico destacam-se os métodos de empilhamento Kirchhoff, nos quais somam-se os dados sísmicos ao longo de curvas específicas multiplicadas por funções peso que garantem o controle das amplitudes.

O processamento convencional, sem um tratamento adequado de preservação de amplitude, mascara ou até inviabiliza o mapeamento de propriedades petrofísicas, prejudicando a correlação entre o dado sísmico e a informação de perfil. Uma forma de estimar corretamente as amplitudes e, por conseqüência, os coeficientes de reflexão nas interfaces sísmicas, é efetuar uma migração pré-empilhamento em verdadeira amplitude, onde a distorção das amplitudes devido ao espalhamento geométrico ao longo do raio de reflexão é compensado pela operação de migração. Entretanto, esse processo tem um custo elevado, sendo também dependente do modelo de velocidades utilizado.

Uma rotina menos dispendiosa e mais estável em relação a erros no modelo de velocidade, consiste na transformação da seção sísmica obtida com a geometria de aquisição no afastamento comum em seções simuladas de afastamento nulo em amplitude verdadeira. Neste caso, as amplitudes das reflexões primárias em afastamento comum são transformadas de tal forma que o fator de espalhamento geométrico original (dependente do afastamento) é automaticamente substituído pelo correspondente fator de espalhamento geométrico do afastamento nulo. O coeficiente de reflexão é, no entanto, preservado, possibilitando a sua aplicação em estudos de AVO. A operação de transformação de uma seção sísmica de afastamento constante para a sua correspondente em afastamento nulo recebe o nome de migração para afastamento nulo em verdadeira amplitude (TA MZO). No caso de um meio com velocidade constante, a curva de empilhamento do MZO e a função peso se reduzem a fórmulas analíticas, minimizando o esforço computacional.

A MÉTODO UNIFICADO DE IMAGEAMENTO SÍSMICO EM MEIOS 2,5D

Neste método considera-se a situação 2,5D (Bleistein, 1986): onde a propagação da onda sísmica é 3D e o modelo geológico é 2D. Seja, também, a subsuperfície formada pela sobreposição de camadas estratificadas, isotrópicas, e não homogêneas separadas por interfaces refletoras suaves, de tal forma que a propagação da onda é descrita pela teoria do raio de ordem zero para reflexões primárias (Cerveny, 1985 e 1987).

Sob estas condições, as ondas emitidas por uma fonte pontual localizada no eixo *x* são registradas por receptores também localizados no eixo *x* propagando-se idealmente no plano *(x,z)*. Portanto, ´podem ser descritas pela teoria dos raios (Bleistein, 1986).

O objetivo do MZO tipo Kirchhoff é transformar as reflexões primárias que são encontradas na seção de afastamento comum ao longo das curvas de tempo de trânsito na sua correspondente de afastamento nulo em amplitude verdadeira. A expressão analítica que em um único passo representa essa operação é uma integral de empilhamento ponderado tipo Kirchhoff (Tygel et al., 1998)

$$\hat{U}_0(\xi_0,t_0)=\frac{1}{\sqrt{2\pi}}\int_A d\xi\, K_{MZO}(\xi,N_0)\,D^{1/2}U(\xi,t)\Big|_{t=\tau_{MZO}(\xi,N_0)}, \quad (1)$$

onde $t = \tau_{MZO}(\xi,N_0)$ é a curva de empilhamento para o MZO, ξ é a coordenada do ponto médio variando ao longo da abertura A, $D^{1/2}$ representa o operador de meia derivada em tempo negativo e $K_{MZO}(\xi,,N_0)$ é a função peso. Pela expressão (1) vê-se que cada ponto N_0 na seção de afastamento nulo a ser simulada será posicionado um valor de amplitude obtido pelo empilhamento ponderado ao longo da curva de MZO. Como mostrado em Schleicher et al (1993), a integral (1) pode ser avaliada assintoticamente pelo método da fase estacionária (Bleistein, 1984) para as altas frequências, no ponto estacionário.

A curva de empilhamento do MZO é o lugar onde se localizam todas as contribuições na seção de afastamento comum para a determinação da amplitude em cada ponto $N_0 = (\xi_0,t_0)$ na seção de afastamento nulo a ser simulada. Ela representa, consequentemente, a relação entre o tempo em afastamento nulo e o não nulo, podendo ser deduzida, do

(*)PETROBRAS/E&P-SSE/UN-RIO/ATEX/PS (**) PETROBRAS/E&P-Corp/TG (***) UNICAMP/IMECC

ponto de vista cinemático, a partir de raciocínio semelhante ao da resposta impulsiva do DMO.

Tygel et al. (1998) mostraram que a curva de empilhamento e a função peso para a migração em afastamento nulo para velocidade constante *($t = \tau_{MZO}$)* são fórmulas analíticas, sendo a primeira função do tempo no afastamento nulo *(t_0)* e da velocidade *(v)*

$$t = \frac{2h}{v}\sqrt{1+\left(\frac{vt_0}{2h}\right)^2 a^2(\eta)}\,, \quad (2)$$

enquanto a segunda é dada por

$$K_{MZO}(\xi, N_0) = \frac{a(\eta)\sqrt{t}}{h}\left(2a^2(\eta)-1\right), \quad (3)$$

onde, em ambas as expressões acima, foi utilizada a notação de Black et al.

$$a(\eta) = \frac{1}{\sqrt{1-\frac{\eta^2}{h^2}}}, \qquad |\eta| = |\xi - \xi_0| < h. \quad (4)$$

Ao aplicar-se o MZO aos dados sísmicos, representa-se o refletor imageado por uma faixa migrada de largura distinta daquela original. Este efeito é definido como distorção do pulso, ao qual relaciona-se um fator de estiramento que será denotado como m_{MZO}. Como demonstrado em Tygel et al. (1998) o fator de estiramento no MZO é

$$m_{MZO}(\xi_R, N_{0R}) = \cos\Theta\,, \quad (5)$$

onde Θ define o ângulo de incidência da reflexão original no afastamento comum, ou seja o sinal de reflexão simulado em afastamento nulo é estirado em relação ao sinal sísmico original em afastamento comum ou em relação a uma seção de afastamento nulo real de um valor correspondente ao coseno do ângulo de incidência, consequentemente o conteúdo de frequência será escalonado por este valor.

Observando-se a equação para o fator de estiramento no MZO (5) percebe-se que a aplicação da migração para afastamento nulo aos dados sísmicos em afastamento comum fornece uma medida independente do ângulo de incidência Θ, desde que seja possível estimar a assinatura da fonte antes e depois do MZO. Como a estimativa da assinatura da fonte é problemática, um método de obter os ângulos de reflexão para cada afastamento comum que compõem o experimento sísmico, mais especificamente, em estudos de AVO é executar um segundo MZO com uma função peso modificada de forma conveniente (Bleistein, 1987, Tygel et al., 1993 e Bleistein et al., 1999). Considerando a segunda função peso como sendo

$$\tilde{K}_{MZO}(\xi, N_0) = \cos\Theta K_{MZO}(\xi, N_0)\,, \quad (6)$$

onde $K_{MZO}(\xi, N_0)$ é a função peso original para o algoritmo do MZO. Tomando-se, em seguida, a razão entre as duas respostas de saída, obtidas das integrais ponderadas do MZO, com os diferentes pesos $\tilde{K}_{MZO}(\xi, N_0)$ e $K_{MZO}(\xi, N_0)$ têm-se a estimativa do ângulo de incidência

$$\frac{\tilde{U}_0(\xi_0, N_0)}{\hat{U}_0(\xi_0, N_0)} = \frac{\tilde{K}_{MZO}(\xi, N_0)}{K_{MZO}(\xi, N_0)} = \cos\Theta. \quad (7)$$

MODELO SINTÉTICO E A RESPOSTA SÍSMICA

Na figura (1) observa-se o modelo sintético utilizado, onde a interface plano-inclinada é o fundo do mar com profundidade de 100 a 500 m. A segunda interface é curva e representa um marco sismoestratigráfica do Oligoceno Inferior cuja profundidade varia de 2500 a 3700 m. A última interface que aparece no modelo em profundidade de 3000 a 4100 m é o topo do reservatório, estando a acumulação de óleo restrita a feição dômica segmentada por duas falhas. As velocidades intervalares, para este modelo, são v1 = 1500 m/s para o meio1. v2 = 3000 m/s, v3 = 3400 m/s, v4 = 3800 m/s para o meio 4 que representa um arenito saturado com óleo e v5 = 4300 m/s para a areia com água. As densidades, para todos os meios, são constantes e iguais a unidade.

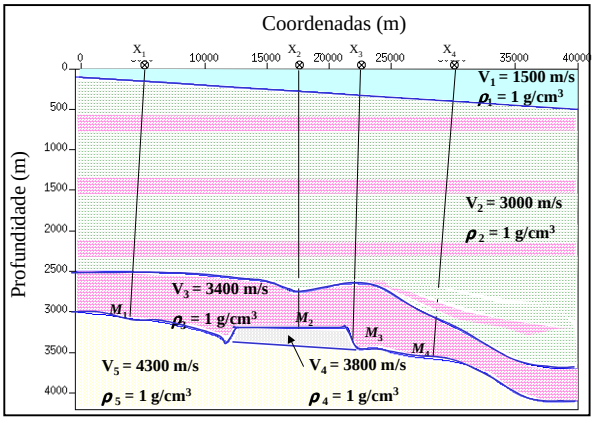

Figura 1: Modelo da Terra em profundidade

A imagem sísmica foi gerada no CWP/Cshot tendo sido o intervalo de tiro e de receptores de 50 m, a banda de freqüência, para construção da assinatura da fonte, de 4 – 72 Hz, com o comprimento do operador de 150 ms, a razão de amostragem de 4 ms e o tempo de registro igual a 4 seg. Trinta seções sísmicas sintéticas em afastamento comum foram modeladas com afastamentos variando de 100 até 3000 m equiespaçados de 100 m. Uma seção em afastamento nulo também foi imageada de modo a fornecer uma comparação com o resultado proveniente da aplicação do MZO à verdadeira amplitude.

Recuperação de Atributos Sísmicos Utilizando a Migração para Afastamento Nulo

As seções sísmicas em afastamento comum foram processadas utilizando dois fluxos de processamento contidos na figura (2) com o mesmo modelo de velocidade (figura 3). Quatro pontos médios foram selecionados para realização das análises de A-VO/AVA (figura 1) após a .aplicação da migração para afastamento nulo no dado modelado e do DMO FK.

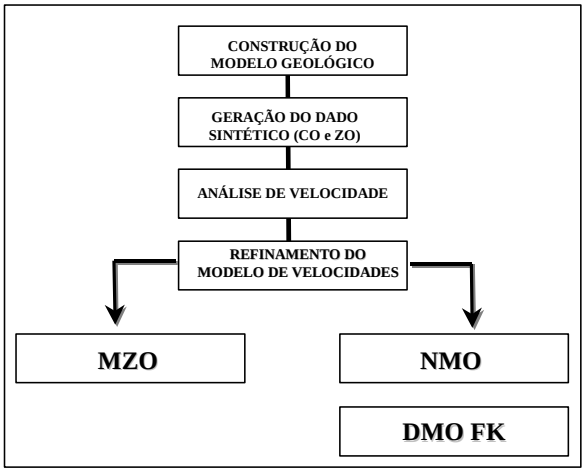

Figura 2: Seqüências de Processamento

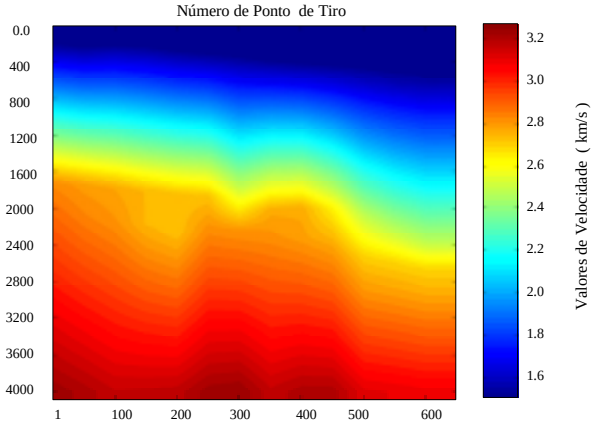

Figura 3: Modelo de Velocidades RMS

Colecionando as amplitudes de pico, nos CMPs selecionados, e exibindo-as contra o afastamento obteve-se as respostas de AVO do arenito com água (CMPs X_1 e X_4) e do arenito com óleo (CMPs X_2 e X_3), para as duas seqüências de processamento realizadas (figura 4). A comparação deste AVO padrão com o AVO teórico, obtido segundo a equação acústica do coeficienete de reflexão, assumindo as mesmas velocidades e densidades do modelo geológico, pode ser realizada mediante um esforço computacional adicional. No entanto, a aplicação de um segundo MZO, com peso ligeiramente diferente do primeiro, fornece a estimativa do ângulo de incidência, permitindo uma comparação direta entre o AVA obtido da aplicação da migração para afastamento nulo em verdadeira amplitude e o AVA teórico.

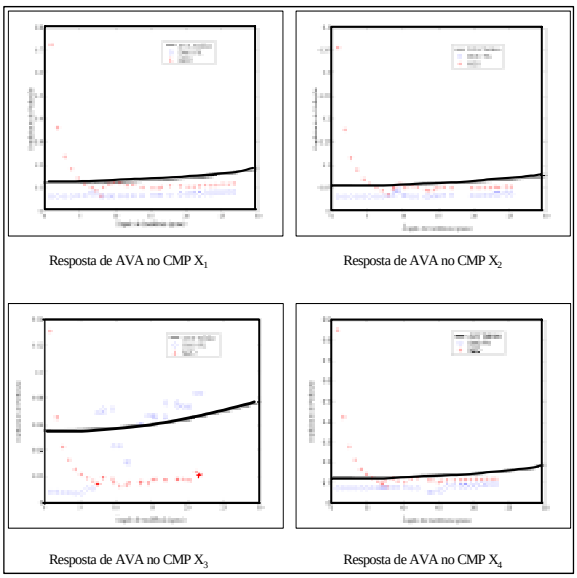

Figura 4: Respostas de AVO para os CMPs selecionados.

DISCUSSÃO DOS RESULTADOS

Este exemplo sintético desrespeita a hipótese de velocidade constante, com um modelo de velocidade relativamente acentuado. As respostas de AVO, contidas na figura (4), indicam valores similares obtidos tanto com DMO FK quanto com TA MZO. Nesta figura nota-se com maior evidência os valores de amplitudes discrepantes nos afastamentos curtos para o TA MZO.

Neste estudo, como o meio de propagação é acústico a diferença dos coeficientes de reflexão teóricos para o arenito saturado com água ou com óleo está exclusivamente nas velocidades dos meios envolvidos que sejam o reservatório (arenito) e a rocha encaixante (marga). Nota-se que a resposta de AVA teórica para o arenito com água aproximadamente duas vezes a resposta obtida para a areia com óleo. As comparações realizadas com a curva teórica de AVA, figura (4), mostram que nos CMPs X_1, X_2 e X_4, os resultados fornecidos pelo TA MZO passam a exibir valores satisfatórios a partir do afastamento de 1000 m, indicando uma tendência de aumento da amplitude com o ângulo de incidência para as duas alternativas de processamento (TA MZO e DMO FK) tanto para água (CMPs X_1 e X_4) quanto para óleo (CMP X_2), o que está de acordo com os modelos de saturação, já que estes dois fluidos apresentam propriedades petro-

(*)PETROBRAS/E&P-SSE/UN-RIO/ATEX/PS (**) PETROBRAS/E&P-Corp/TG (***) UNICAMP/IMECC

físicas semelhantes. Apesar dos valores de amplitude resultantes do TA MZO estarem deslocados da curva teórica, no CMP X_3, eles ainda exibem um aumento da amplitude com o ângulo de incidência o que não ocorre com os valores provenientes do DMO FK. Portanto, a estimativa do AVO *gradient*, para o TA MZO, fornece um melhor resultado.

Os gráficos de erro comparando os resultados das duas seqüências de processamento utilizadas estão apresentados na Figura (5), permite visualizar a distribuição dos erros. Neste exemplo, onde a distância entre traços é de 50 m, o problema na abertura do operador torna-se mais crítico e os valores de amplitude passam a exibir erros muito elevados nos afastamentos curtos.

A comparação das respostas de AVO/AVA e dos gráficos de erro realizadas entre o TA MZO e o DMO FK permite afirmar que as amplitudes obtidas pela migração para afastamento nulo à verdadeira amplitude melhoram a análise de AVO/AVA. Isto se deve ao fato do TA MZO fornecer melhores aproximações das perdas por espalhamento geométrico que o DMO FK. Esse fato contribui para que acha uma melhoria na estimativa dos atributos de AVO.

Problemas na função velocidade, apesar de não fornecer grandes erros na parte cinemática, podem levar a valores de amplitude não confiáveis, o que impossibilitaria a sua utilização em análises de AVO/AVA. A interpretação de velocidade se mostrou ser o ponto crítico para a correta obtenção dos valores de amplitude, onde velocidades mais altas que a verdadeira levam a um decréscimo nas amplitudes enquanto que velocidades mais baixas levam a um aumento nas amplitudes. Uma outra dificuldade do TA MZO está relacionada a amostragem espacial que pode deteriorar a qualidade da imagem nos afastamentos curtos e diminuir a fidelidade das curvas de AVO/AVA. Portanto, as análises de AVA/AVO, nos refletores mergulhantes, devem ser restritas a uma banda de freqüência não falseada, podendo no intuito de minimizar o problema realizar uma interpolação de traços no dado sísmico. Recomenda-se o uso de um filtro anti-alias para preservação das amplitudes.

Este trabalho empregou um modelo acústico e com gradiente pequeno de velocidade, pois num primeiro momento desejava-se testar a potencialidade do TA MZO em estudos de AVO/AVA, obtendo respostas rápidas e sem perda de generalidade. O natural prosseguimento deste trabalho deve aplicar a metodologia desenvolvida em exemplos mais realistas e em dados reais.

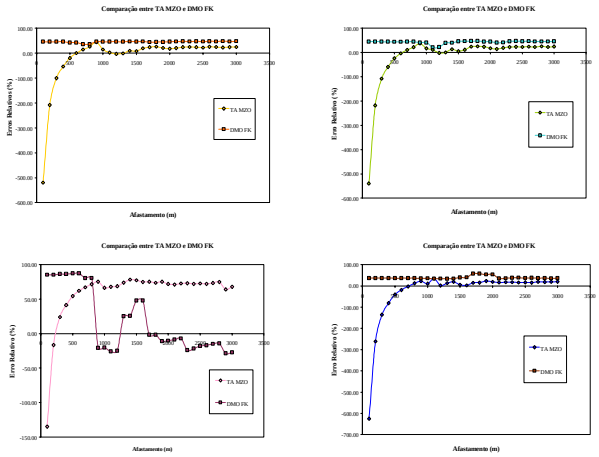

Figura 5: Gráficos de erro para as respostas de AVO encontradas segundo os dois fluxos de processamento

REFERÊNCIAS BIBLIOGRÁFICAS

Black, J. L.; Schleicher, K. L.; Zhang, L. True-amplitude imaging and dip moveout. *Geophysics*, v. 58, p. 47–66, 1993.

Bleistein, N.; Cohen, J.; Jaramillo, H. True-amplitude transformation to zero offset of data from curved reflectors. *Geophysics*, v. 64, p. 112 – 129, 1999.

Hubral, P.; Schleicher, J.; Tygel, M. A unified approach to 3D seismic reflection imaging. Part I: Basic concepts. *Geophysics*, v. 61, p. 742–758, 1996 a.

Oliveira, A. S.; Tygel, M.; Filpo, E. On the application of true-amplitude DMO. *Journal of Seismic Exploration*, v. 6, p. 279-289, 1997.

Oliveira, A. S.; Ramos, A. C. B.; Tygel, M. True amplitude MZO and AVO: application to real data. 5th INTERNAT. CONGRESS OF THE BRAZILLIAN GEOPHYSICAL SOCIETY, 1997, Rio de Janeiro, Expanded Abastract, v. 1, p. 223–226.

Oliveira, A.S.; Mezzomo, L.C DMO-Teoria e Prática.

Tygel, M.; Schleicher, J.; Hubral, P. Pulse distortion in deph migration. *Geophysics*, v. 59, p. 1561–1569, 1994b.

Tygel, M.; Schleicher, J.; Hubral, P. Dualities involving reflectors and reflection-time surfaces. *Journal of Seismic Exploration*, v. 4, p. 123–150, 1995.

Tygel, M.; Schleicher, J.; Hubral, P. A unified approach to 3D seismic reflection imaging Part II: Theory. *Geophysics*, v. 61, p. 759–775, 1996.

Tygel, M.; Schleicher, J.; Hubral, P. 2,5D Kirchhoff MZO in laterally inhomogeneous media. *Geophysics*, v. 63, p. 557–573, 1998.

Time to Depth Conversion by Multivariate Mapping

Paulo Eduardo Miranda Cunha[1] , & *Eduardo Filpo Ferreira da Silva*[2]

Abstract

The method performs a conversion of time migrated sections to depth. The algorithm distributes the samples of the time migrated section along the *image ray* (Hubral and Krey, 1977) for which the trajectory is in general different from the vertical ray, in the presence of lateral variations of the velocity field. Its main function is to correct the effects of mis-positioning of the time image, due to lateral velocity variations when the option is to use the fast time migration (TM) instead of prestack depth migration (PSDM). In many cases the comparison of PSDM with TM, followed by the time to depth conversion (TDC), give similar results. This favours the use of the latter which is less expensive in many applications. This method uses ray tracing with an adaptive time step size control (Cunha, 1999) which is necessary for obtaining high precision in the ray coordinates/times and, as consequence, in the precision of the depth of the reflectors. This method reduces the sources of errors leaving only the uncertainties of the velocity field analysis.

Introduction

It is well known that the pre/pos-stack time migration methods (Hubral and Krey, 1977), such as Kirchoff, solve the wave equation by a process equivalent to a weighted amplitude sum along a curve, with times defined by the stack velocity. The velocity analysis is made in time and for each pair of points, ξ at the surface and t (time) in the seismogram $v \equiv v(\xi, t)$. It is normal practice to assume a hyperbolic difraction curve, which is reasonable for near offsets. One point (ξ_0, t_0) of the time stack section is fixed as appex of the hyperboloid where the result of the summation is located. This procedure avoids ray tracing for determining the transit times. These times and amplitudes are an aproximation of the Greens function centered in point (x_0, z_0) of the depth section. The greater the lateral velocity variations, the larger the differences in horizontal coordinates of both points, $\xi_0 \neq x_0$, Fig-2. The reason for this is the Fermat principle, which determines that the ray which links the point x_0, y_0, z_0 to the aquisition surface, must emerge orthogonally to the surface, i.e., *image ray*, (Hubral and Krey, 1977) and its path is different, in general, from the vertical ray. Although ray-tracing is an efficient tool, its use in the construction of the Green function may be very expensive and justifies the use of time migration for a large number of cases. The TDC by *image ray* often becomes a necessity in common situations such as the continental slope, where the water column works as an optical prism bending the *image ray* far from the vertical, which can cause errors in the interpretation.

Method Fundations

Here we present a new implementation of 2D/3D TDC based on the multivariate mapping Fig-1. This function $\mathcal{M} : (\xi, \eta, t) \rightarrow (x, y, z)$ is a map linking the point (ξ, η, t) in time section to another (x, y, z) in depth. The surfaces of constant t are horizontal planes in the time section and isochrons in the depth section. The surfaces of constant ξ and η are vertical planes in the time section and surfaces formed by image rays in the depth section. In ray-tracing a method was used (Cunha, 1999) which adapts the time interval between points to the variations of the gradient of the slowness field. This achieves high precision ray-tracing, eliminating the errors except for the uncertainties in the velocity analysis. After this the time section is re-sampled at a constant time interval. One point (ξ_0, η_0, t_0) in the time migrated section corresponds to a unique point (x_0, y_0, z_0) in the image ray. The image ray starts in a surface point of coordinates (ξ_0, η_0) which correspond to the inline and crossline CDPs, respectively. The time to depth convertion of this point is made by moving the time section amplitude, $A(\xi_0, \eta_0, t_0)$, to a corresponding depth

[1]PETROBRAS S/A, Brasil
[2]PETROBRAS S/A, Brasil.

point $A(x_0, y_0, z_0)$. But the latter doesn't necessarily agree with the depth grid. Hence the ray-tracing is made for each surface cell and always there will be one image ray near each depth grid point. The amplitude of a point of the depth grid can be calculated by a second order Taylor expansion with a source point in the image ray:

$$A(\vec{x}) = A(\vec{x}_0) + \frac{\partial A(\vec{x})}{\partial x^i}\Big|_{\vec{x}_0}(x^i - x_0^i) + \frac{1}{2}\frac{\partial^2 A(\vec{x})}{\partial x^i \partial x^j}\Big|_{\vec{x}_0}(x^i - x_0^i)\left(x^j - x_0^j\right) + O\left[|\vec{x} - \vec{x}_0|^3\right] . \quad (1)$$

The derivatives: $\frac{\partial A(\vec{x})}{\partial x^i}$ e $\frac{\partial^2 A(\vec{x})}{\partial x^i \partial x^j}$ are not known, but the Jacobian matrix $\left[\frac{\partial t^j}{\partial x^i}\right]$ of the mapping $\mathcal{M}$ and its determinant $\mathcal{J}_{\mathcal{M}}$ allows its conversion to time derivatives by some tensorial relations.

Then for each image ray point $A(x_0, y_0, z_0)$: a) the derivatives of the time section amplitudes are calculated by finite difference, with a 4^{th} order precision operador, b) the Jacobian matrix, its determinant and its inverse are determined, based in the image ray coordinates, c) all of the nine time derivatives are converted to depth and the coefficients of the Taylor series are determined. With these coefficients, the amplitude $A(x_0, y_0, z_0)$ are scattered for all grid points inside a square window (2D), a cubic window (3D) Fig-3, with a weight factor proporcional to the inverse of the distance from the image ray point to the grid depth point.

Examples

The result of the pre-stack depth migration Fig-4, with depth velocities, is close to the post-stack time migration, followed by image ray TDC, Fig-5, assuming the use of the same velocity field. This result demonstrates the good behavior of both processes. However, Fig-6 shows that the results are not satisfactory for a TDC using time velocities converted to depth by vetical ray.

Conclusions

- The time migration followed by image ray TDC using depth velocities resulted in a good equivalence to PSDM in the present case of moderate geological complexity.
- The same process using stack velocities did not achieve satisfactory results.
- TDC by vertical ray using stack velocities is not a good solution, even in a situation of moderate geological complexity.
- These results are a warning to the risks of a geological interpretation based on a time migrated section. This interpretation is equivalent to one based on vertical ray TDC using a *constant* velocity field.
- The TDC process recquires a good depth velocity analysis.
- Reliable tools (i.e. migration, tomography) are needed to properly convert time velocity field to depth.

Referências

Cunha, P. E. M., 1999, High precision/fast adaptive step size ray-tracing by curvature criteria: Presented at the 6th Ann. Internat. Mtg., Brazilian Geophysical Society, Soc. Expl. Geophys.

Hubral, P., and Krey, T., 1977, Time migration - some theoretical aspects: Geoph. Prosp., **25**, *738–745.*

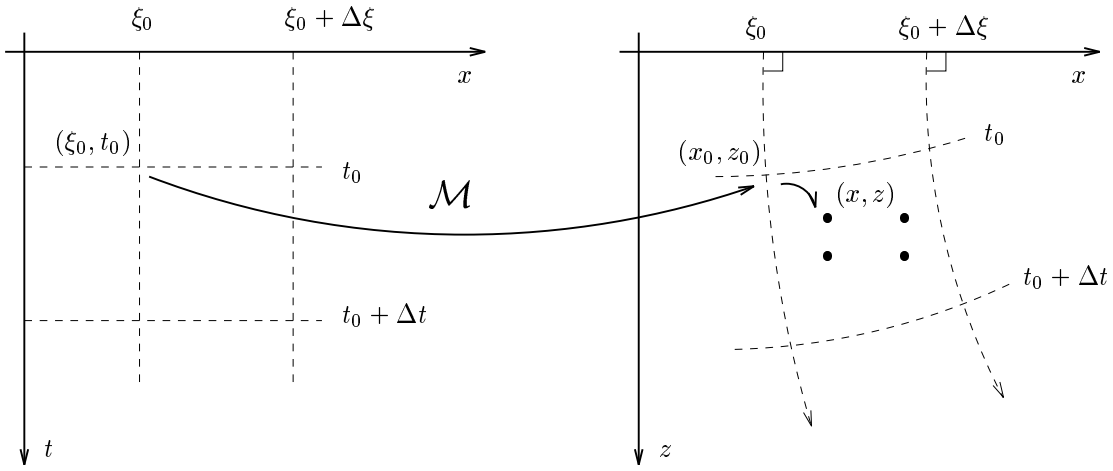

$$\mathcal{M} : (\xi, t) \rightarrow (x, z)$$

$$dxdz = \left| \frac{\partial(x,z)}{\partial(\xi,t)} \right|_{x_0,z_0} d\xi dt = \mathcal{J}^{\mathcal{M}}\big|_{x_0,z_0} d\xi dt$$

Figura 1: 2D Time to Depth mapping

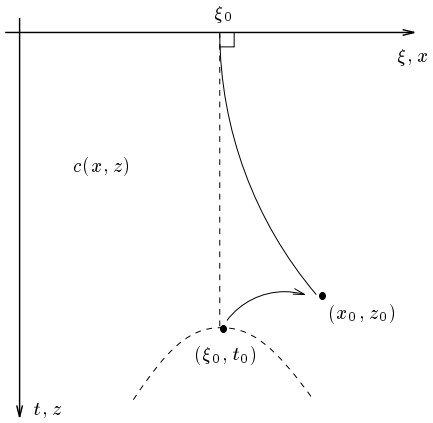

Figura 2: Time migration + Time/Depth conversion for generic medium.

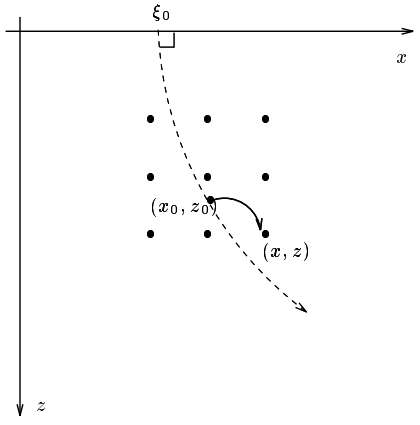

Figura 3: Taylor expansion: $A(x_0, z_0) \rightarrow A(x, z)$

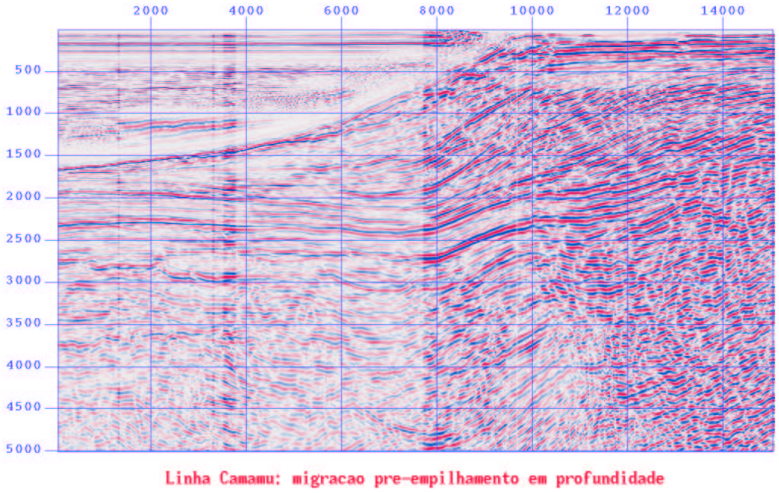

Figura 4: Pre-Stack Depth Migration.

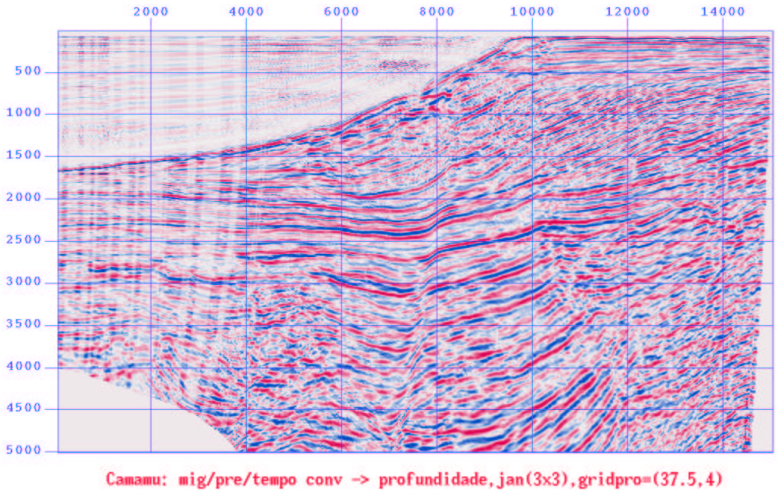

Figura 5: Time Migration plus Image Ray TDC

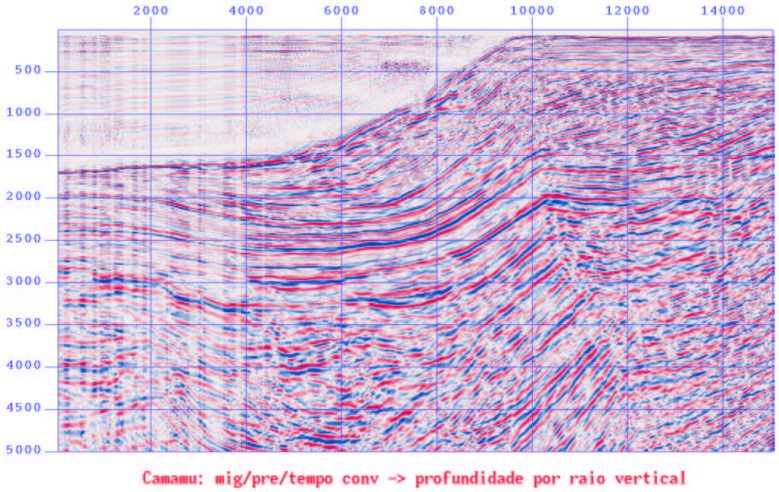

Figura 6: Time Migration plus Vertical Ray TDC

1098

Velocity field smoothness *via* spatial dependence information for seismic imaging

***Paulo Sérgio LUCIO**, ICEx-UFMG – Brazil, lucio@est.ufmg.br*

Abstract

The purpose of this work is to present an overview of velocity seismic sampling with emphasis on spatial stochastic processes, focusing on the variographic information of seismic velocity field. Seismic imaging - by ray tracing to estimate the Green's function values taking into account the migration/inversion accuracy requirements of geological structures with strong velocity non-homogeneity - requires an accurate determination of the distribution of the propagation velocities and the trade-off between resolution and computing costs. Construct the smooth seismic velocity model based on the spatial data analysis filtering and cardinal cubic B-spline parameterization seems to be quite attractive for this goal.

Smoothing the velocity grid by cubic B-splines procedure assures the existence of second derivatives on each knot of the velocity field, a necessary (but not sufficient) condition for ray tracing algorithms to estimate the required travel-times and geometrical spreading. It is not necessary to introduce interfaces into the model, which greatly facilitates the ray tracing and is also attractive for ray-based depth migration. In the applications on the Ray Tracing algorithms, the velocity macro model is smooth, represented by cardinal cubic B-splines (the continuity of the second derivatives is necessary for the continuity of the Fréchet derivatives).

For the sake of simplicity, only 2D problems are considered (*Marmousi Model*). The smoothness proposed here, has to yields excellent results, which give a better qualitative and quantitative resolution, compared with those carried out by conventional Gaussian windowing interpolation. If the velocity map is to be used to look for spatial patterns in the data, it is important to map smoothed values that take into account the spatial non-homogeneity of variances, as well as any spatial dependence between locations.

Keywords: geostatistics; variogram; kriging; structural modeling.

Introduction

The problem of smoothing velocity models is quite interesting. A possible method consists on optimizing the splines coefficients for that the velocity field been as close as possible of the initial model discretised by a regular grid. But this method can not conserve the travel-time between two points of the model and the true amplitude. Any way, we know that is not possible with a smoothed model to respect the same kinematics and dynamics parameters of the layered model of all points located on the model. A practical smooth method, based on the spatial information, is proposed to approximate the velocity field as close as the real one. This method improves the interpolation accuracy and requires little computational effort, or none at all if the velocity model makes it possible to take advantage of overall ray-shooting number reduction.

The numerical application of the final migration formula with multiple arrivals requires the computation of multivalued maps of travel-times, amplitudes, the angles of rays and the KMAH index [5]. Such maps can be computed accurately by the wavefront construction code DRTUWFC-2D™ [3] or DRTUWFC-3D™ [4]. It is quite common for prestack imaging algorithms to generate Green's function using smooth-velocity macro models defined by means the convolution of a Gaussian windowing filter following by the determination of B-splines knots.

Geostatistics is a set of numerical tools to be added to the large tool chest of the geologist; it allows transporting quantitatively a geological model all the way to process design and engineering. So, to creating the velocity model, it is necessary to know how many degrees of freedom (independent variables or spatial structural dependency of knots) we need for its description correctly. For the 2D or 3D ray tracing algorithms ([3] and [5]) we use a parameterization of the velocity model based on B-splines, after an adequate description of the field that must present smooth spatial variation, here mentioned as variographic analysis.

Variographic analysis

The mean ($\mu(x) = E[V(x)]$) of the variable $V(x)$ relates the number of events in arbitrary volumes ($x \in 2D$), and clearly depend on the size of the particular basic volume involved. First order ($\mu(x)$) proprieties can be described in terms of intensity. Second order proprieties or spatial dependence, when one assume that the variance of $V(x)$ exists for all $x \in 2D$, involves the relationship between numbers of events in pairs of the basic area (or volume). This can be formally described by the second order intensity, called spatial covariance, defined by

$$Cov(V(x), V(x + \vec{h})) = C(\vec{h}) .$$

A weaker assumption than that of stationary (or quasi-stationary) processes [2] is intrinsic stationary

which is defined through a constant mean and a constant variance in the differences between values at locations separated by a given distance and direction, that is

$E(V(x)-V(x+\vec{h}))=0$ and $Var(V(x)-V(x+\vec{h}))=2\gamma(\vec{h})$

($2\gamma(\vec{h})$ is the variogram function). This second moment is said to be stationary. Stationarity is a model decision, not some intrinsic property of the actual distribution of the values over the domain region. For a stationary process, the second order intensity depends on only the vector difference, $\vec{h}$ (direction and distance), between two sample points and not on their absolute locations. The process is called isotropic, if the dependence is purely a function of the length h, of the vector and not its orientation; that is, purely a function of the distance and not direction [2]. (Fig.1)

Spatial information

Prediction is a primary interest in the analysis of spatially continuous phenomena. The interest is on the description of possible patterns in the locations of the events. It is attributed values over $R\in 2D$ (the region under study), based on observed values at a pre-defined and fixed set of locations. The locations of the attribute value are simply the sparse grid velocity. The situation considered is one where the series of observations on a spatially continuous attribute, have been recorded at corresponding spatial locations.

The objective of these analyses is to infer the nature of spatial variation in the attribute over the whole of R, from the sampled point values. We can seek description in terms of a smooth-surface, which captures large-scale global trends (modeling first order variation in the mean value of the process). Alternatively, one might wish to study aspects of local variability (modeling second order variation or spatial dependence between two locations in R). Particularly, if the primary objective is one of accurate interpolation or prediction of the value of the attribute at points other than the sampled one, it is involve a mixture of methods. Some designed to examine large-scale heterogeneity in the mean value of the attribute over R. Others, where one shall examine areas within which one assume the process to be stationary and/or isotropic and look for spatial dependence by means of variogram or covariogram information, attempting to capture the spatial information (covariance) structure of the process.

Typically, one can observe high covariance or correlation at short distances and lower covariance or correlation at greater distances, for many spatially continuous phenomena, where seismic velocity field is concerned.

The critical step of covariance or variogram inference and modeling allows determination of all required covariance values.

First of all, the interest is in using the covariogram, or variogram, simply as exploration devices to examine spatial dependence in the observed data. Then, we can see how these functions play a major role in the modeling of such data. In order to estimate $C(\vec{h})$ or $\gamma(\vec{h})$ for an observed seismic velocity spatial process it is in practice necessary to make some sort of micro scale quasi-stationary assumption, otherwise one can not estimate the second order proprieties.

So, one begin an exploratory analysis of second order proprieties or covariance structure by first estimating an isotropic variogram, by mean of a coordinate transformation in case of geometric anisotropy behavior detection. Subsequent analysis can then proceed to calculate directional variograms in almost four broad directions in order to explore for possible directional effects or anisotropy.

For a stationary process the sample variogram should rise to an upper bound, the *sill* corresponding to $C(0)$. The distance at which this occurs is referred to as the *range* (a). The discontinuity at the origin of the sample variogram is often referred to as the *nugget effect* or white noise (C_0). Clearly, a variogram consisting of pure nugget effect corresponds to a process with no spatial dependence. If the variogram rises as unbounded concave-upwards curve away from the origin, this may indicate a first order drift or trend in the process. In our case the contrast velocity field is defined as a stochastic process $\{V(x), x\in R\}$ where $V(x)$ is assumed to be the random variable from the regionalized phenomenon (velocity contrast).

To have a better structural model, a local estimator that can yield the spatial distribution of parameters throughout the structure should base localization of characteristic parameters on sparse samples by the kriging approach.

Smoothing 2D Velocity Field

Kriging interpolation

Spatial interpolation corresponds to the case where the data relate to the same attribute but at different locations.

Consider an unknown value v_0 (the *target* for prediction) as an outcome of the random velocity. The n velocity data values $v_\alpha, \alpha = 1,...,n$ are themselves interpreted as n outcomes of n random velocity "*reponse*" variables $V_\alpha, \alpha = 1,...,n$ associated with locations, the sampling design. The model is typically defined indirectly by full conditionals, $[V_i / V_j, \forall j \neq i]$. The set $V_0, V_1, ..., V_n$, real-valued stochastic process called *signal* processes, is characterized by assuming a probability model, an expression for the means: $E\{V(x_\alpha)\} = \mu_\alpha, \alpha = 0,1,...,n$, assumed known, and an expression for the covariances:

$$Cov\{V(x_\alpha), V(x_\beta)\} == C_{\alpha\beta}, \forall \alpha, \beta = 0,1,...n.$$

The unknown value v_0, the conditional distribution of the *target* given the data, can be estimated by a linear combination of the n velocity data plus a shift parameter, by the relation: $\hat{V}_0 = \lambda_0 + \sum_{\alpha=1}^{n} \lambda_\alpha V_\alpha$ (best choice needs a criteria: the best predictor minimizes the *MSE*, given by the conditional expectance). The expected value of the prediction error is $E\{V_0 - \hat{V}_0\} = m_0 - \lambda_0 - \sum_{\alpha=1}^{n} \lambda_\alpha m_\alpha$. So, by the unbiasedness (this is a BLUP) constraint we obtain $\hat{V}_0 = m_0 + \sum_{\alpha=1}^{n} \lambda_\alpha [V_\alpha - m_\alpha]$. To determine the n weights λ_α, we act upon to minimize the error of prediction variance. By this way, we establish the normal system equations, also known kriging system: $\sum_{\beta=1}^{n} \lambda_\beta C_{\alpha\beta} = C_{\alpha 0}, \forall \alpha = 1,...,n$ (assuming a stationary Gaussian process for the *signal*). The corresponding minimized error variance, the normal kriging variance, is then: $\sigma_k^2 = C_{00} - \sum_{\alpha=1}^{n} \lambda_\alpha C_{\alpha 0}$. In matrix notation, the system can be written by $\lambda = K^{-1}.\kappa$, where $K = [C_{\alpha\beta}]$ and $\kappa = [C_{\alpha 0}]; \alpha, \beta = 1,...,n$. Because the conditional variance does not depend on the observed data, the prediction mean square error is equal to the prediction variance.

This system, yields one and only one solution as soon as the data covariance matrix K is positive definite. Defining the residual data matrix as R_α^T the kriging estimator can be written as:

$$\hat{V}_0 = m_0 + \lambda^T.R_\alpha = m_0 + \kappa^T.K^{-1}.R_\alpha .$$

The minimized estimation variance is:

$$\sigma_{SK}^2 = C_{00} - \kappa^T.K^{-1}.\kappa .$$

The choice of covariance functions must be allows minimizing the resulting error variance [2]. The predictor compromises between its unconditional mean and the observed data. Besides, the kriging estimator is an exact interpolator.

Case-study

The *Marmousi Model* (Fig.2 (a)) is a well-known 2D synthetic acoustic model ($1{,}500/-/5{,}000$ m/s). It often is considered as a reference for testing imaging in complex area [5]. It was build by the IFP-France for simulating a 2D marine seismic acquisition from Angola [1]. Data were computed by finite differences of the acoustic equation, and the model was given by dense velocity and density grids sampled in each coordinate to 4.0 meters. A hydrocarbon trap is located just under the complex structure with abscises between $5{,}500$ and $7{,}500$ meters and ordinate (depth) about $2{,}500$ meters.

We assume that the *Gaussian Marmousi Model* holds when the data vector is transformed component-wise. The differentiability of the Gaussian stochastic process guarantees that the degree of smoothness is a property of the spatial interpolation. The mean-square differentiability is directly linked to the differentiability of its covariance function.

To have a better structural model, a local estimator that can yield the spatial distribution of parameters throughout the structure should base localization of characteristic parameters on sparse samples, a re-sampled model ($16x4.0m = 64.0m$). An optimum estimator for this purpose can meet by filtering the velocity field by the variogram law (Fig.1), providing that estimation variance is defined properly for the random velocity field.

The 2D ray-tracing code requires smooth-velocity models. For this application, a kriging filter of the exact velocity field can obtain the background velocity model, taking into account the spatial correlation length (the influence ratio), that gives the local cutoff frequency of this filter. The smoothed

model then is projected on the cardinal cubic B-splines basis.

The database was filtered using a *exponential* variogram framework information:

$$\gamma(h) = C_0 + C(1 - e^{-3h/a}), h > 0.$$

The spatial variability of velocity was analyzed by the variogram function where $C_0 = 0.$, $h = 16.0m$, $C(0) = 440{,}000.0$ and $a = 128.0m$ (or $a = 256.0m$), see Fig.1. The geometrical anisotropy factor is 0.1. The layers are well represented on the final image (Fig.2).

Conclusions

A case-study performed on a set of data distributed spatially indicates that kriging provides reasonably accurate prediction of local distribution of the velocity field and good estimates of the corresponding average of the final image, prepared for ray tracing algorithm. For a more smoothed model, it is sufficient to increase the *range* of the variogram model (Fig.2 (b) and (c)). Even in caustic zones the control of the prediction error can be done, once the variability depends only on the theoretical spatial correlation structure defined by the variogram.

Additional researches should include an extensive case study using the results of migration to compare how smooth the velocity field we need to do not affect the final image. Sensitivity analyses of the predictions on the indices of accuracy and hardness of the information. And, of coarse, the application to the 3D domain [4]. Exhaustive analyses based on 2D Ray Tracing [3] algorithm will be showed.[1]

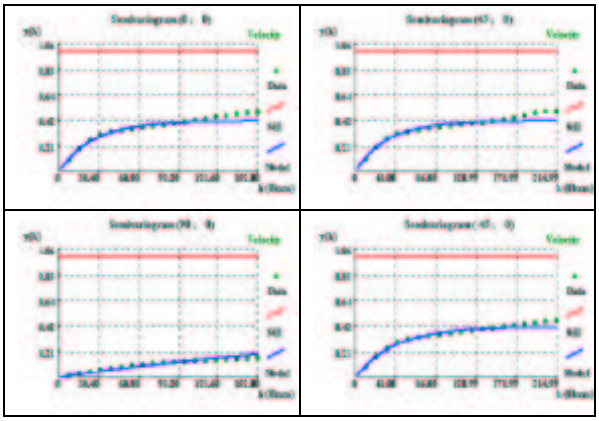

Fig.1: The four principal direction variograms for the *Gaussian Marmousi Model*, where a geometric anisotropy is detected. Remark the anomalous laterally comportment.

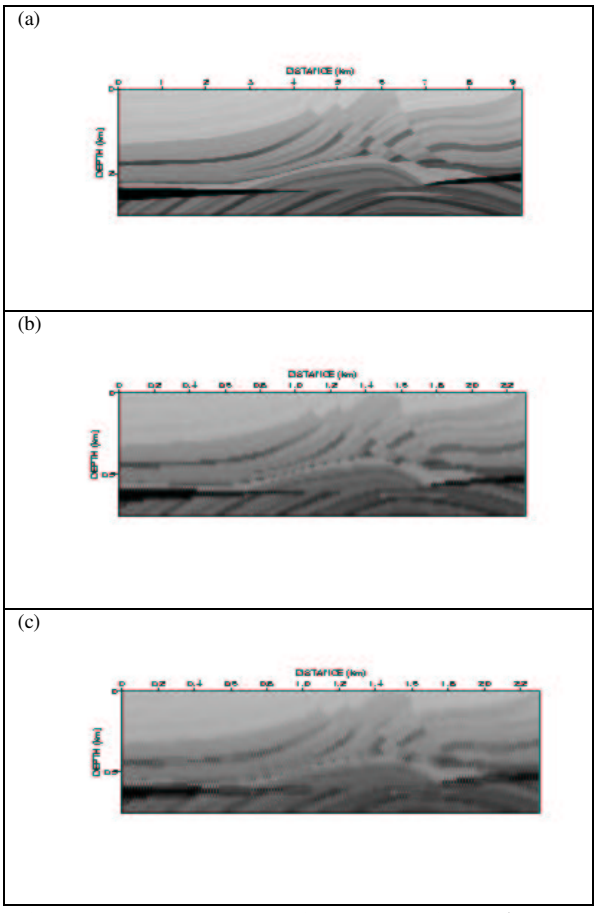

Fig.2: (a) Exact *Marmousi Model* (*2301x751*) points at $4.m$, (b) and (c) Smoothed Re-Sampled *Marmousi* (*577x189*) points at $16.m$, *a=128.0m* and *a=256.0m*.

References

[1] Bourgeois, A., Bourget, M., Lailly, P., Poulet, M., Ricarte, P., and Versteeg, R. (1991). "Marmousi Model and Data", in Versteeg, R., and Grau, G., Eds., "The Marmousi Experience": Eur. Assn. Expl. Geophys., 5-16.

[2] Journel, A. G., and Huijbregts, C. J. (1978). Mining Geostatistics. London: Academic Press.

[3] Lambaré, G., Lucio, P. S., and Hanyga, A. (1996). "Two Dimensional Multivalued Traveltime and Amplitude Maps by Uniform Sampling of a Ray Field." Geophys. J. Int., 125: 584-598.

[4] Lucio, P. S., Lambaré, G., and Hanyga, A. (1996). "3D Multivalued Travel Time and Amplitude Maps." Pure and Applied Geophysics, 148: 499-479.

[5] Operto, S., Xu, S., and Lambaré, G. (1998). "Can We Image Quantitatively Complex Models with Rays? " 68th Ann. Internat. Mtg. Soc. Expl. Geophys., Extended Abstracts, 1120-1123.

[1] **Acknowledgements**

This Project was supported by the CNPq - CTPEPRO - Brazil 400002/97-3 (NV). The GeoMS™ - Geostatistical Modelling Software was gently provided by the CMRP - IST - Portugal